In presenting the dissertation as a partial fulfillment of the requirements for an advanced degree from the Georgia Institute of Technology, I agree that the Library of the Institute shall make it available for inspection and circulation in accordance with its regulations governing materials of this type. I agree that permission to copy from, or to publish from, this dissertation may be granted by the professor under whose direction it was written, or, in his absence, by the Dean of the Graduate Division when such copying or publication is solely for scholarly purposes and does not involve potential financial gain. It is understood that any copying from, or publication of, this dissertation which involves potential financial gain will not be allowed without written permission.

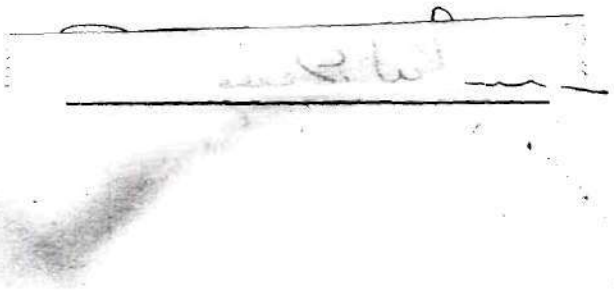

7/25/68

A DOMINANT MODE ANALYSIS OF MICROWAVE HYBRID INTEGRATED CIRCUIT TRANSMISSION LINES

A THESIS

Presented to

The Faculty of the Graduate Division

by

Russell Perry Wharton

In Partial Fulfillment

of the Requirements for the Degree

Doctor of Philosophy

in the School of Electrical Engineering

Georgia Institute of Technology

June, 1970

A DOMINANT MODE ANALYSIS OF MICROWAVE HYBRID

INTEGRATED CIRCUIT TRANSMISSION LINES

Approved: [redacted]

Date approved by Chairman: 7/11/70

ACKNOWLEDGMENTS

I wish to express my sincere appreciation to my thesis advisor, Dr. G. P. Rodrique, for his guidance and assistance during the development of this thesis. I also wish to thank Dr. F. K. Hurd, for his guidance and advice both prior to and during the period of research, and Dr. J. L. Hammond, Jr. for his service as a member of the reading committee.

I also wish to thank the National Science Foundation for the fellowship and to Dr. B. J. Dasher and Dr. D. T. Paris for the opportunity to teach in the School of Electrical Engineering.

To Dr. G. R. Harrison and the staff at Sperry Microwave Electronics Company go a special thank you for the financial support, the many helpful discussions, the preparation of the substrates, the use of their equipment, and the many lasting friendships, all of which helped make this endeavor successful.

My deepest appreciation goes to my wife, Carroll, to whom this thesis is dedicated, for her patience, understanding, and encouragement during the difficult times of intensive work.

TABLE OF CONTENTS

TABLE OF CONTENTS

LIST OF TABLES

LIST OF TABLES
(Concluded)

LIST OF ILLUSTRATIONS

LIST OF ILLUSTRATIONS
(Continued)

LIST OF ILLUSTRATIONS
(Continued)

LIST OF ILLUSTRATIONS
(Continued)

LIST OF ILLUSTRATIONS
(Concluded)

SUMMARY

The objective of this thesis research has been to obtain a complete description of the field configuration of the dominant mode in microstrip. This was accomplished theoretically by numerical analysis procedures which determined the phase constant, the guide wavelength, and the field configuration. The phase constants at various frequencies and the relative amplitude and direction of the magnetic field were determined experimentally. The theoretical and experimental results were then compared in order to more accurately characterize the dominant hybrid coupled microstrip mode.

The theoretical method of attack has been to solve numerically the vector Helmholtz equations for the longitudinal fields. A system of finite-difference equations corresponding to a quantized microstrip region was written and then cast into an eigensystem form. The direct method approach was used to calculate the eigenvalue (which led to the frequency-phase constant diagrams) via the QR transform and the eigenvector (which led to the longitudinal and then transverse fields) via the inverse iteration technique.

The numerical analysis technique predicted that the longitudinal electric and magnetic fields are indeed present and that these fields have a non-negligible amplitude as compared with the transverse fields. The frequency-phase constant curves indicated that the microstrip mode does not propagate as a TEM mode, but instead showed a slight amount of

normal dispersion whenever the guide wavelength is comparable with the substrate thickness. The magnetic field calculations showed that at the air-dielectric interface just past the center strip there is a substantial component of circular polarization in two orthogonal planes. The mode pattern of the magnetic field in the vicinity of the center strip is shaped like an inverted saddle.

To complement and verify the theoretical calculations a loosely coupled transmission resonance experiment was run to determine the f-β diagrams and a ferromagnetic spin resonance absorption experiment was run to determine the relative amplitudes of the magnetic field components. In the former experiment, the f-β curves had the same relative shape indicating a slight dispersion and both approached the TEM curve at low microwave frequencies. In the latter experiment, the measured magnetic fields indicated very good correlation with the theoretical curves in the vicinity of the center strip. The predicted regions of circular polarization were also verified, as was also the saddle mode shape.

As a result of this research, the propagation characteristics and total field configuration of microstrip are more clearly understood. Consequently, the design of some microwave components could be improved and their performance optimized.

CHAPTER I

INTRODUCTION

Motivation for Problem

Microwave Hybrid Integrated Circuit Transmission Lines

Within the last decade, the microwave industry has been investigating the use of microwave hybrid integrated circuits as a replacement for some conventional microwave circuits.[1-3] The hybrid integrated circuits offer a substantial savings in weight and volume as compared with waveguide circulators, isolators, etc., and potentially at a reduced cost, since many RF components can be fabricated simultaneously. These savings are essential in much of the military and space systems and will generate many uses in commercial applications. Monolithic circuits involve development and fabrication of the entire circuit or system and do not allow for changes or replacement of malfunctioning devices. Hybrid integrated circuits increase the circuit flexibility as each device in the circuit can be developed independently and then integrated into the entire subsystem.

The basis of microwave hybrid integrated circuits is the transmission line which connects the various components together and serves as an integral part of several circuit components. Presently, three different planar transmission line configurations are being considered: microstrip,[1] slot line,[4,5] and coplanar waveguide,[6] whose cross sections

are shown in Figure 1.

The substrate is a high dielectric constant dielectric, semiconductor, or ferrimagnetic material, usually .020" to .100" thick with a dielectric constant ranging between 9 and 16. The substrate metallization is a highly conductive metal usually several skin depths thick.

Slot line and coplanar waveguide have their entire RF circuit on the upper surface of the substrate. In slot line, the RF energy is guided in the slot between the two metal surfaces, whereas in coplanar waveguide, the wave is guided along the center strip between the two outside ground planes.

Microstrip, on the other hand, consists of a center strip on the upper surface of the substrate and a ground plane on the lower surface. The RF energy is guided by the center strip with most of the energy concentrated in the high dielectric substrate. The dielectric constant of the substrate and the ratio of center strip width to substrate thickness determines the characteristic impedance and propagation constant of the line. Of the three lines described, microstrip has been used almost exclusively and thus justifiably it has received the most extensive investigation as to propagation characteristics, characteristic impedance, and losses as functions of the center strip's width, thickness, and conductivity and the substrate's thickness, dielectric constant, and loss tangent.

Review of the Microstrip Literature

TEM Microstrip Mode Assumption. Early experimental determinations for such quantities as the characteristic impedance, phase constant, and

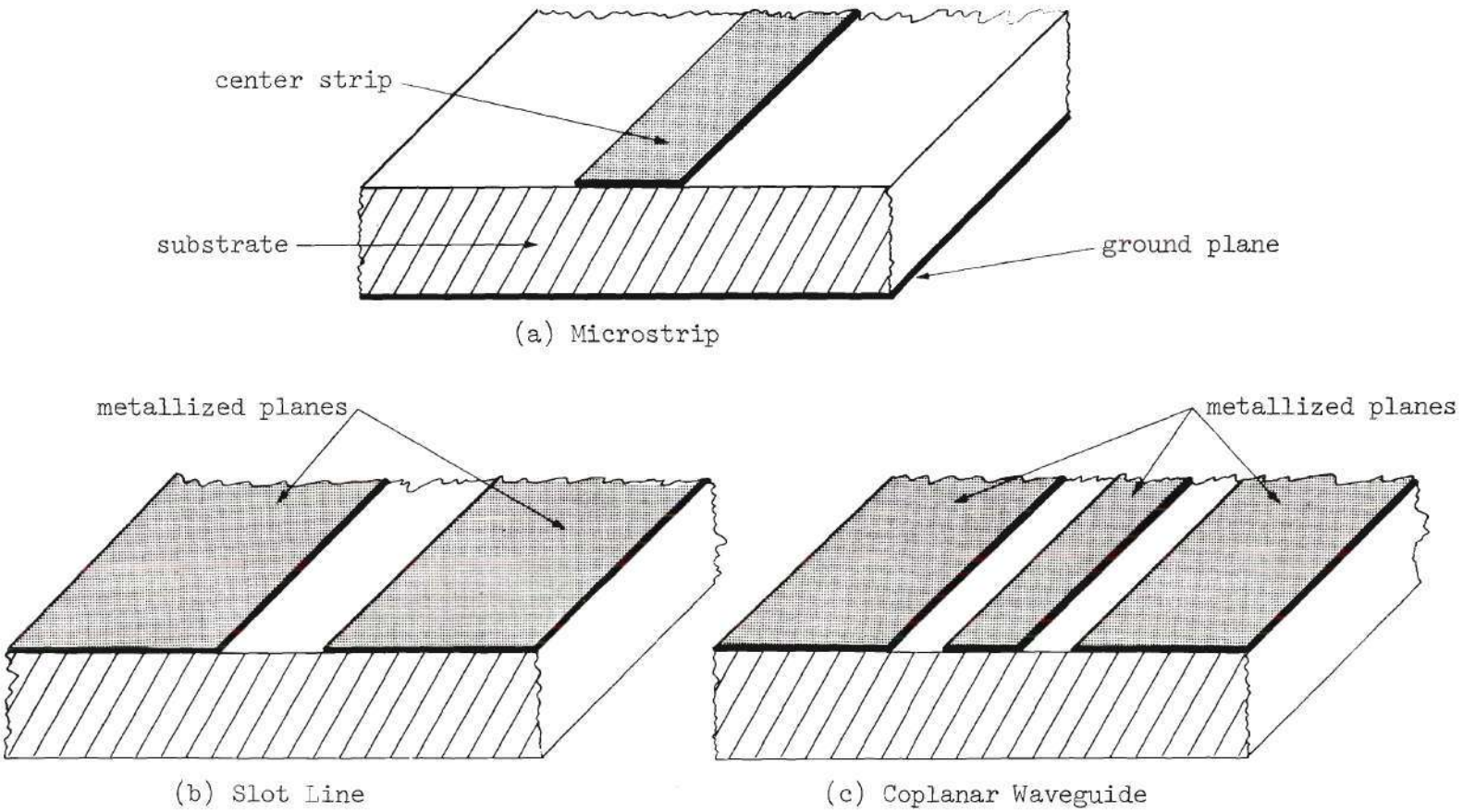

Figure 1. Cross Sections of Microwave Hybrid Integrated Circuit Transmission Lines

loss of microstrip were made by Arditi,[7] while Shafer[8] attempted to determine the field configuration by constructing an oversize model of microstrip using a low dielectric constant material. With special probes he was able to obtain a rough estimate of the field distribution of the microstrip mode propagating in his model. His work verified the existence of a longitudinal magnetic field component. That same year Wu[9] set up the integral equations, whose solution would be a non-TEM mode. However, due to their extremely complicated nature, he was unable to solve them.

Several theoretical analyses were initiated in order to verify the experimental data and to provide new insights into the use of microstrip. Early investigators were unable to obtain analytical expressions for the total field configuration due to the mathematical problems which arose from the presence of the air-dielectric interface. The initial approximations to the field distribution were that the field was entirely transverse to the direction of propagation. If an electromagnetic field is assumed TEM, the vector Helmholtz wave equations

$$\nabla^2 \vec{E} = -\omega^2 \mu_o \epsilon \vec{E} \qquad \nabla^2 \vec{H} = -\omega^2 \mu_o \epsilon \vec{H} \tag{1}$$

reduce to[10]

$$\nabla_T^2 \vec{E} = 0 \quad \nabla_T^2 \vec{H} = 0 \tag{2}$$

Thus, the transverse electric and magnetic fields both satisfy Laplace's equation, and the field distribution in the transverse plane is a static solution. Based on the TEM mode assumption, several methods have been

used to calculate the electromagnetic field and wave parameters.

Assadourian and Rimai[11] assumed the microstrip line to be completely immersed in the dielectric and solved for the characteristic impedance of the TEM mode by conformal mapping techniques. Wheeler[12,13] realized that a purely TEM assumption resulting from a homogeneous dielectric medium was unrealistic and inadequate. He used conformal transformation techniques to obtain expressions for the characteristic impedance of parallel-strip transmission lines separated by a dielectric substrate. The area of the transformed substrate gave him a filling fraction q, which yielded an effective dielectric constant

$$K' = 1 + (K-1)q \tag{3}$$

in terms of the relative dielectric constant K of the substrate. The characteristic impedance

$$Z_o' = Z_o / \sqrt{K'} \tag{4}$$

was then calculated from the free-space characteristic impedance Z_o. These results were based on a propagating TEM mode with a frequency such that the guide wavelength was long compared with the substrate thickness.

Wheeler's method of calculation stimulated interest in generating a more complete set of data. Caulton et al.[14] calculated curves for characteristic impedance and normalized guide wavelength as a function of the ratio of center strip width to substrate thickness. These curves were corroborated experimentally at a single S band frequency and were

assumed to be valid at all microwave frequencies.

Even though the dominant mode of the microstrip line was known to be non-TEM, still other investigators applied various techniques to solve the TEM problem. Finite-difference equation approximations to Laplace's equation, formulated by Green[15] and Schneider[16] were solved by successive-over-relaxation for the transverse fields, and from these iterative solutions the characteristic impedances were calculated.

Steinhelfer[17] using Wheeler's effective dielectric constant, obtained characteristic impedance and loss curves as a function of the microstrip dimensions by using successive-over-relaxation techniques. Bryant and Weiss[18] made use of a dielectric Green's function to solve for the dominant TEM mode of microstrip.

While the previously mentioned investigators realized that the assumption of a TEM mode was not rigorously correct, they continued to use the TEM mode approximation since (1) differences between their theoretical calculations and the available experimental measurements were reasonably small, (2) longitudinal magnetic field components were thought to be of negligible value as compared with the transverse field, and (3) no straightforward approach to calculate the fields of the non-TEM mode was known.

Hybrid Coupled Microstrip Mode. The microstrip mode can be shown to be non-TEM by considering the consequences of requiring the longitudinal field components of a propagating wave to be zero along an air-dielectric interface. As shown in Johnson,[19] for zero longitudinal fields, the nontrivial solution is obtained only if

$$k_c^2 = \omega^2 \mu_o \epsilon - \beta^2 = 0 \tag{5}$$

In air, this means

$$\omega^2 \mu_o \epsilon_o = \beta_{air}^2 \tag{6}$$

and in the dielectric

$$\omega^2 \mu_o \epsilon_o K = \beta_{dielectric}^2 \tag{7}$$

However, along the interface the phase constants of the two wave solutions must match resulting in

$$\omega^2 \mu_o \epsilon_o = \omega^2 \mu_o \epsilon_o K \tag{8}$$

which contradicts the original assumption that there was an air-dielectric interface. Shafer[8] proved that neither a pure TE mode nor a pure TM mode can be supported on microstrip by showing that the fields associated with each mode considered separately cannot match the boundary conditions along the interface and at the center strip independently. In order to satisfy all the boundary conditions, the microstrip mode has to be a combination of TE and TM modes existing simultaneously, thus forming a hybrid coupled mode.

Interest in the hybrid microstrip mode has increased, as evidenced by the theoretical research in the area that has been presented at recent symposiums. Denlinger[20] presented a method for determining the characteristic impedance and propagation velocity of microstrip by determining,

via the dielectric Green's function technique of Bryant and Weiss, the longitudinal currents on an infinitesimally thin wire and then expressing the fields which are generated to be the summation of TE and TM mode fields. His integral equation technique seems to be a basic continuation of Wu's earlier development. Zysman and Varon[21] demonstrated that, at microwave frequencies, the mode propagation velocity deviated considerably from that determined by the TEM electrostatic approximations. Their method was to assume a sum of TE and TM modes, each satisfying the wave equation and external boundary conditions, and the total satisfying the continuity equations on the interface and the continuity equations on the center strip. Both hybrid mode techniques seem, however, to be incapable of determining the microstrip mode field distribution. A finite-difference equation eigensystem approach by Hornsby and Gopinath[22] similar to, but developed independently from, the research in this thesis has just been published. They solve for the hybrid mode that exists on a waveguide enclosed microstrip. Their results will be discussed in a later chapter.

Definition of the Problem

When this research was begun there were no known analytical or numerical calculations for the longitudinal field components which distinguish the microstrip mode from the ordinary TEM mode. Since a longitudinal magnetic field component had been observed experimentally on a microstrip model, an analytical or numerical technique was obviously needed in order to more completely describe the entire electromagnetic field distribution. It is known in the microwave industry that the

development of devices and components using microstrip as a basis cannot be easily achieved without a more complete understanding of the microstrip mode. Thus a more accurate knowledge of the electromagnetic field in the region of the center strip is needed by microwave engineers working in this integrated circuit area.

For example, if theoretically calculated fields indicating a plane of circular polarization of the magnetic field for some specific geometry were known, a resonance isolator could be easily developed by placing a piece of ferrimagnetic material in the region of the circular polarization and applying a DC magnetic field of proper intensity perpendicular to the plane of circular polarization. This would eliminate the costly trial and error procedure which quite frequently does not produce the optimum device.

Purpose of the Research

The purpose of this research has been to more completely determine the RF electromagnetic field distribution of the dominant mode in the region immediately surrounding the center strip in microstrip.

The primary objectives of the work in this thesis have been:

(1) To develop a computer program using state-of-the-art procedures that determines for microstrip the electromagnetic field configuration, phase constant, and guide wavelength at various frequencies.

(2) To experimentally examine the relative amplitude and direction of the magnetic field of the dominant microstrip mode.

(3) To experimentally determine the phase constants at various frequencies for the dominant mode.

(4) To compare the numerical and experimental results in order to characterize the dominant hybrid coupled microstrip mode.

Method of Attack

Theoretical Approach. The theoretical approach has been to solve numerically the vector Helmholtz equation by bounding the microstrip with zero longitudinal field walls and subdividing the region with a system of nodes. A system of finite-difference equations corresponding to the system of nodes is written and then cast into an eigensystem form. The solution of the eigensystem yields the desired phase constant and field configuration at a given frequency. An indirect method, the iterative successive-over-relaxation technique, was attempted since the order of the eigensystem was large, but unfortunately convergence could not be obtained. The direct method approach was used with the eigenvalues being calculated by the QR transform and the eigenvectors by the inverse iteration technique. The transverse fields are numerically determined from Maxwell's equations.

Experimental Approach. The magnetic field on microstrip was experimentally probed with a small yttrium-iron garnet sphere. The ferromagnetic spin resonance absorption for different orientations of a DC biasing magnetic field was measured. From these measurements, the relative magnetic field components were calculated. The phase constant versus frequency curves were experimentally determined by observing the transmission resonances in a loosely coupled length of short circuited microstrip line.

CHAPTER II

THEORETICAL DEVELOPMENT OF THE MICROSTRIP MODEL

Introduction

The electric and magnetic fields of the microstrip transmission line, as in any electromagnetic field configuration, must satisfy Maxwell's equations subject to appropriate boundary conditions. Any propagating mode can be shown to have a z dependence of the form $e^{j\omega t-\gamma z}$. The propagation constant γ is defined as

$$\gamma = \alpha+j\beta \tag{1}$$

where α is the attenuation constant and β is the phase constant. The dielectric media are assumed to be linear, homogeneous, and isotropic. The substrate has a sufficiently low loss tangent and ohmic losses are neglected so that the lossless case is considered, and α is taken as zero. Thus the mode propagates as $e^{j(\omega t-\beta z)}$ in the +z direction. The center strip and ground plane are treated as being infinitely thin and perfectly conducting.

Longitudinal Fields

In most previous theoretical developments for microstrip the investigators chose to neglect the presence and effect of any longitudinal field components. A TEM mode results when these longitudinal fields are neglected, and the hybrid coupled mode is lost in the analysis.

The longitudinal fields can be calculated by manipulating Maxwell's equations as done in Paris and Hurd[23] into the vector Helmholtz wave equations.

$$\nabla^2 \vec{E} = -\omega^2 \mu_o \epsilon \vec{E} \qquad (2)$$
$$\nabla^2 \vec{H} = -\omega^2 \mu_o \epsilon \vec{H}$$

These elliptic partial differential equations are cast into a better form for solution by:

(1) recalling that in rectangular coordinates, the vector Laplacian operator can be written as a sum of the scalar Laplacian operators in each coordinate direction,

$$\nabla^2 \vec{F} = \vec{a}_x \nabla^2 F_x + \vec{a}_y \nabla^2 F_y + \vec{a}_z \nabla^2 F_z \qquad (3)$$

(2) separating the two vector equations into six scalar Helmholtz equations, and

(3) solving two of these six equations,

$$\nabla^2 E_z = -\omega^2 \mu_o \epsilon E_z \qquad (4)$$
$$\nabla^2 H_z = -\omega^2 \mu_o \epsilon H_z$$

for the longitudinal fields E_z and H_z. Since the z dependence has been specified as $e^{-j\beta z}$, the Laplacian operator is replaced by the transverse Laplacian operator ∇_T^2 and the scalar Helmholtz equations reduce to

$$\nabla_T^2 E_z + k_c^2 E_z = 0 \tag{5}$$

$$\nabla_T^2 H_z + k_c^2 H_z = 0$$

where

$$k_c^2 = \omega^2 \mu_o \epsilon - \beta^2. \tag{6}$$

Solution of these two equations, subject to the boundary conditions of the microstrip configuration, yields the spatial distribution of E_z and H_z in the transverse xy-plane.

Transverse Fields

The next step in determining the electromagnetic field configuration of the microstrip mode is to derive the equations for the transverse fields in terms of the longitudinal fields. This derivation is carried out in most standard electromagnetic field texts, and the resulting equations are

$$H_x = \frac{1}{k_c^2}\left(j\omega\epsilon \frac{\partial E_z}{\partial y} - j\beta \frac{\partial H_z}{\partial x}\right) \tag{7}$$

$$H_y = -\frac{1}{k_c^2}\left(j\omega\epsilon \frac{\partial E_z}{\partial x} + j\beta \frac{\partial H_z}{\partial y}\right)$$

$$E_x = -\frac{1}{k_c^2}\left(j\beta \frac{\partial E_z}{\partial x} + j\omega\mu_o \frac{\partial H_z}{\partial y}\right)$$

$$E_y = \frac{1}{k_c^2}\left(-j\beta \frac{\partial E_z}{\partial y} + j\omega\mu_o \frac{\partial H_z}{\partial x}\right)$$

Mathematical Model for Microstrip

The total field configuration of microstrip has not been determined

by purely analytical methods. The reason is that the boundary conditions which must be satisfied on the center strip and air-dielectric interface introduce analytical complications into the solution of the partial differential equations, Equations (5), which cannot be overcome with the present theory. Since analytical methods have failed, finite-difference approximations to Equations (5) are solved on a digital computer using numerical analysis techniques.

A standard numerical analysis technique is to quantize the region of interest by subdividing it by a grid or net and solving these Helmholtz equations at each node.[24] However, microstrip by its very nature is an open structure and as such would have an infinite number of nodes. It is then necessary to enclose the region around the microstrip by some kind of bounding wall. Two obvious choices are:

(1) Enclosing the microstrip in a metal box, or

(2) Enclosing the microstrip in a bounding box on which the longitudinal electric and magnetic fields are zero.

The former method allows for generation of fields by charges and currents in the bounding wall, whereas the latter choice simply requires the longitudinal electric and magnetic fields to fall off to zero as they approach the walls.[†] Experimentally, the microstrip fields are found to decay to zero far away from the center strip. Based on this fact, the zero field walls were chosen to enclose the region and thereby limit the nodes of the net to a finite number. The upper limit to the number of nodes

---

[†]At the walls the longitudinal fields are required to be zero. However, there is no constraint on the normal derivatives of the fields at the bounding walls so that transverse fields may still exist there.

depends on the technique used to solve the equations at each of the nodes and the computer used to carry out the calculations.

Due to the symmetry of microstrip, which can be seen in Figure 1, only half the configuration need be considered, thus halving the number of nodes. The microstrip model is shown in Figure 2. The plane of symmetry is a magnetic wall over which $\frac{\partial E_z}{\partial x} = 0$ and $H_z = 0$.

Finite-Difference Equation Development

Transverse Helmholtz Equations at Nodes in Air and Dielectric

The transverse Helmholtz equations, Equations (5), must be satisfied at each node, and therefore finite-difference equation equivalents to these partial differential equations are determined. Since the equations for E_z and H_z are alike, the symbol ϕ will be used to mean either E_z or H_z in the equations.

The Taylor series approximation for a scalar function is used to derive the finite-difference expressions for the first and second order derivatives,

$$\phi(x+h,y) = \phi(x,y) + h\phi'(x,y) + \frac{h^2\phi''}{2!}(x,y) + R_n(x,y) \tag{8}$$

with

$$|R_n(x,y)| \leq \frac{h^n}{n!} \sup_{x<r<x+h} |\phi^n(r,y)| \tag{9}$$

Equation (8) can be written as

$$\phi(x+h,y) = \phi(x,y) + h\phi'(x,y) + \frac{h^2\phi''}{2!}(x,y) + \frac{h^3\phi'''}{3!}(x,y) + \frac{h^4\phi''''}{4!}(x,y) + \ldots. \tag{10}$$

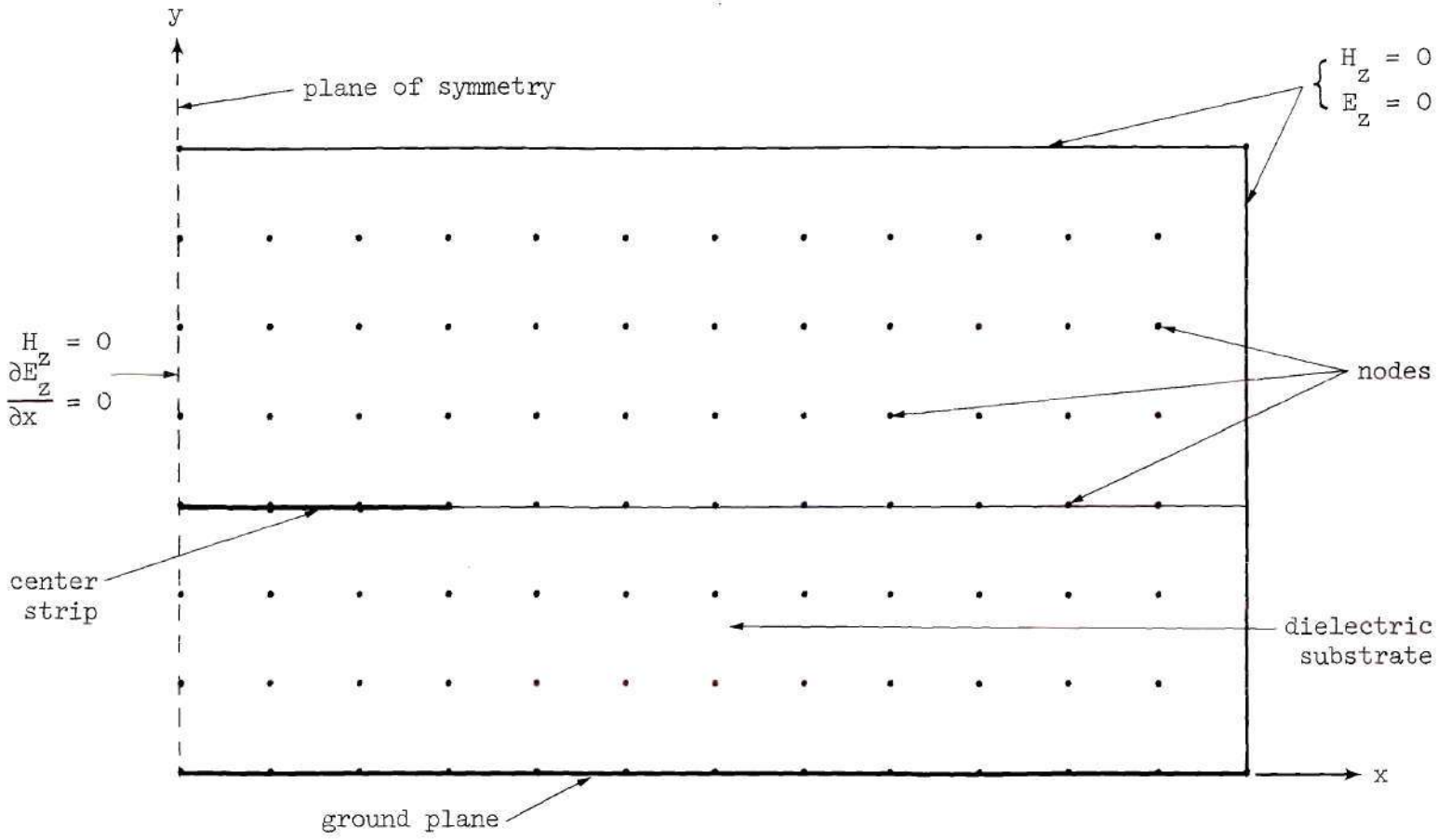

Figure 2. Node System for the Microstrip Model

The scalar field ϕ_4 and ϕ_2 of the nodes adjacent to the center node in the x direction in Figure 3 are

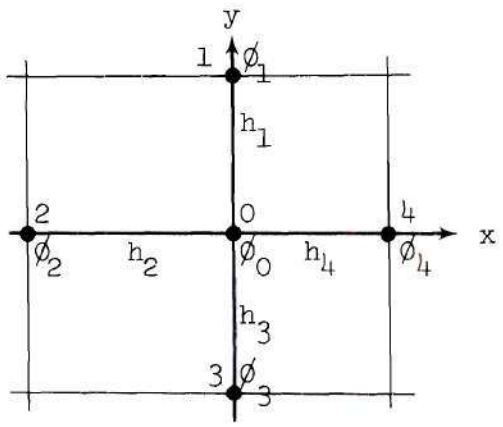

Figure 3. A Typical Arrangement of Neighboring Nodes

$$\phi_4 = \phi_o + h_4 \left(\frac{\partial\phi}{\partial x}\right)_o + \frac{h_4^2}{2!}\left(\frac{\partial^2\phi}{\partial x^2}\right)_o + \frac{h_4^3}{3!}\left(\frac{\partial^3\phi}{\partial x^3}\right)_o + \frac{h_4^4}{4!}\left(\frac{\partial^4\phi}{\partial x^4}\right)_o + \cdots \qquad (11)$$

$$\phi_2 = \phi_o - h_2 \left(\frac{\partial\phi}{\partial x}\right)_o + \frac{h_2^2}{2!}\left(\frac{\partial^2\phi}{\partial x^2}\right)_o - \frac{h_2^3}{3!}\left(\frac{\partial^3\phi}{\partial x^3}\right)_o + \frac{h_2^4}{4!}\left(\frac{\partial^4\phi}{\partial x^4}\right)_o - \cdots$$

Neglecting terms above the fourth order, these two equations are rearranged and added to yield

$$\left(\frac{\partial^2\phi}{\partial x^2}\right)_o = \frac{\phi_4-\phi_o}{h_4^2} + \frac{\phi_2-\phi_o}{h_2^2} - \left(\frac{\partial\phi}{\partial x}\right)_o\left(\frac{1}{h_4} - \frac{1}{h_2}\right) - \left(\frac{\partial^3\phi}{\partial x^3}\right)_o\left(\frac{h_4-h_2}{3!}\right) \qquad (12)$$

$$- \left(\frac{\partial^4\phi}{\partial x^4}\right)\left(\frac{h_4^2+h_2^2}{4!}\right)$$

and subtracted to yield

$$\left(\frac{\partial \phi}{\partial x}\right)_o = \left(\frac{h_2 h_4}{h_2+h_4}\right)\left(\frac{\phi_4}{h_4^2} - \frac{\phi_2}{h_2^2} - \phi_o\left(\frac{1}{h_4^2} - \frac{1}{h_2^2}\right)\right) - \left(\frac{h_2 h_4}{3!}\right)\left(\frac{\partial^3 \phi}{\partial x^3}\right)_o \qquad (13)$$

$$- h_2 h_4 \left(\frac{h_4 - h_2}{4!}\right)\left(\frac{\partial^4 \phi}{\partial x^4}\right)_o$$

Substituting Equation (13) into Equation (12) yields

$$\left(\frac{\partial^2 \phi}{\partial x^2}\right)_o = 2\left(\frac{\phi_4}{h_4(h_2+h_4)} + \frac{\phi_2}{h_2(h_2+h_4)} - \frac{\phi_o}{h_2 h_4}\right) + \left(\frac{\partial^3 \phi}{\partial x^3}\right)_o\left(\frac{h_2 - h_4}{3}\right) \qquad (14)$$

$$+ \left(\frac{\partial^4 \phi}{\partial x^4}\right)_o\left(\frac{-h_4^2 + h_2 h_4 - h_2^2}{12}\right)$$

Neglecting the last two terms, the second order derivative of the function ϕ at the center node is approximated by

$$\left(\frac{\partial^2 \phi}{\partial x^2}\right)_o = 2\left(\frac{\phi_4}{h_4(h_2+h_4)} + \frac{\phi_2}{h_2(h_2+h_4)} - \frac{\phi_o}{h_2 h_4}\right) \qquad (15)$$

Similarly, the second order derivative with respect to y is

$$\left(\frac{\partial^2 \phi}{\partial y^2}\right)_o = 2\left(\frac{\phi_1}{h_1(h_1+h_3)} + \frac{\phi_3}{h_3(h_1+h_3)} - \frac{\phi_o}{h_1 h_3}\right) \qquad (16)$$

The transverse Laplacian is approximated by the sum of Equations (15) and (16). The transverse Helmholtz equation is then approximated by

$$2\left(\frac{\phi_1}{h_1(h_1+h_3)} + \frac{\phi_3}{h_3(h_1+h_3)} + \frac{\phi_2}{h_2(h_2+h_4)} + \frac{\phi_4}{h_4(h_2+h_4)}\right) \qquad (17)$$

$$- \phi_o\left(\frac{1}{h_1 h_3} + \frac{1}{h_2 h_4}\right)\Big) = -k_c^2 \phi_o$$

At a node positioned in the air medium,

$$k_c^2 = k_a^2 = \omega^2 \mu_o \epsilon_o - \beta^2 \tag{18}$$

and Equation (17) becomes

$$2\left(\frac{\phi_1}{h_1(h_1+h_3)} + \frac{\phi_2}{h_2(h_2+h_4)} + \frac{\phi_3}{h_3(h_1+h_3)} + \frac{\phi_4}{h_4(h_2+h_4)} - \phi_o\left(\frac{1}{h_1 h_3} + \frac{1}{h_2 h_4}\right)\right) = -k_a^2 \phi_o \tag{19}$$

At a node positioned in the dielectric,

$$k_c^2 = k_d^2 = \omega^2 \mu_o \epsilon_o \kappa - \beta^2 \tag{20}$$

The equation applying there is

$$2\left(\frac{\phi_1}{h_1(h_1+h_3)} + \frac{\phi_2}{h_2(h_2+h_4)} + \frac{\phi_3}{h_3(h_1+h_3)} + \frac{\phi_4}{h_4(h_2+h_4)} - \phi_o\left(\frac{1}{h_1 h_3} + \frac{1}{h_2 h_4}\right)\right) = -k_d^2 \phi_o \tag{21}$$

These finite-difference approximations to the transverse Helmholtz equations are derived for unequal spacing of the nodes, thus allowing for a more general placement of the nodes in the interior of the configuration.

For equal spacing of the nodes, $h = h_1 = h_2 = h_3 = h_4$, Equations (19) and (21) reduce to

$$\sum_{k=1}^{4} \phi_k - 4\phi_o = -h^2 k_a^2 \phi_o \tag{22}$$

and

$$\sum_{k=1}^{4} \phi_k - 4\phi_o = -h^2 k_d^2 \phi_o \tag{23}$$

Transverse Helmholtz Equations at Nodes on Boundaries

Boundary Conditions at Walls. At positions where the nodes lie on metal boundaries, the boundary conditions require $E_z = 0$ and $\frac{\partial H_z}{\partial y} = 0$. Along the plane of symmetry, the boundary conditions are $H_z = 0$ and $\frac{\partial E_z}{\partial x} = 0$.

For the node arrangement in Figure 4,

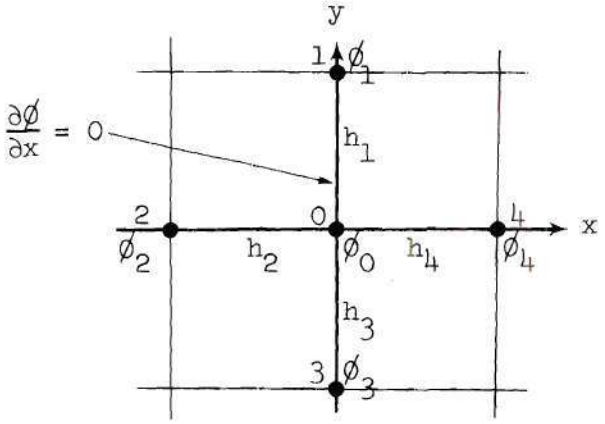

Figure 4. Node Arrangement for the Boundary Condition $\frac{\partial \phi}{\partial x} = 0$

the normal derivative boundary condition $\frac{\partial \phi}{\partial x} = 0$ is approximated by $\phi_4 = \phi_2$ for $h_2 = h_4$. Thus, the transverse Helmholtz equation becomes

$$2\left(\frac{\phi_1}{h_1(h_1+h_3)} + \frac{\phi_3}{h_3(h_1+h_3)} + \frac{\phi_4}{h_4^2} - \phi_o\left(\frac{1}{h_1 h_3} + \frac{1}{h_4^2}\right)\right) = -k_c^2 \phi_o \tag{24}$$

For the boundary condition $\phi = 0$, the approximation is $\phi_2 = -\phi_4$ for $h_2 = h_4$. However, the scalar potential at this node is equal to zero, therefore the node can be eliminated from consideration and the zero value incorporated into the equations for the adjacent nodes, as shown in Figure 5. The Helmholtz equation for the node adjacent to the boundary becomes

$$2\left(\frac{\phi_1}{h_1(h_1+h_3)} + \frac{\phi_3}{h_3(h_1+h_3)} + \frac{\phi_4}{h_4(h_2+h_4)} - \phi_0\left(\frac{1}{h_1 h_3} + \frac{1}{h_2 h_4}\right)\right) = -k_c^2\phi_0 \quad (25)$$

In both Equations (24) and (25) $k_c^2 = k_a^2$ in air and $k_c^2 = k_d^2$ in the dielectric.

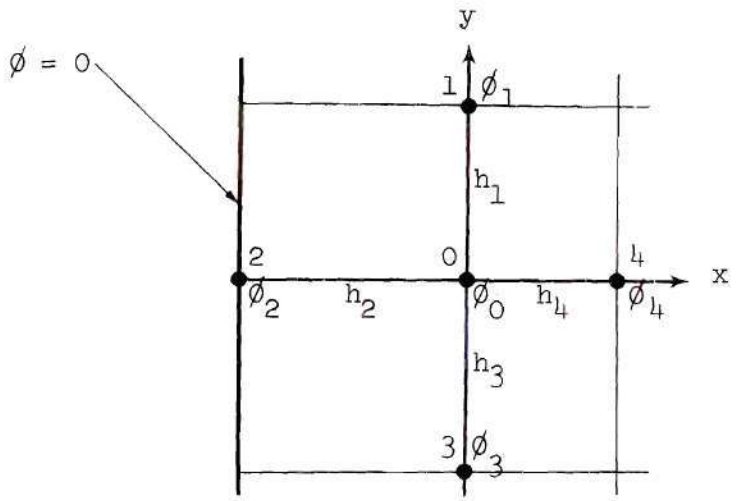

Figure 5. Node Arrangement for the Boundary Condition $\phi = 0$

Boundary Conditions at the Air-Dielectric Interface. Approximations for the Helmholtz equation have been established for all nodes except those lying along the air-dielectric interface. Consider a

typical node positioned on the interface, as shown in Figure 6. See Appendix A for the complete derivation of the interface equations.

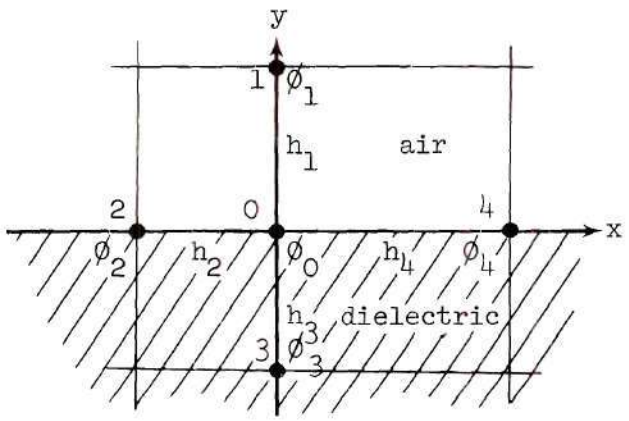

Figure 6. Node Arrangement at the Air-Dielectric Interface

Boundary conditions require that the normal component of the magnetic field be continuous across the interface.

$$H_{y_{air}} = H_{y_{dielectric}} \tag{26}$$

Substituting the equation for H_y from Equations (7) into Equation (26) and defining the unitless parameter

$$T = \frac{k_a^2}{k_d^2} = \frac{\omega^2 \mu_o \epsilon_o - \beta^2}{\omega^2 \mu_o \epsilon_o \kappa - \beta^2} \tag{27}$$

yields

$$\beta\left(\frac{\partial H_z}{\partial y}\right)_A + \omega\epsilon_o\left(\frac{\partial E_z}{\partial x}\right)_A = \beta T\left(\frac{\partial H_z}{\partial y}\right)_D + \omega\epsilon_o \kappa T\left(\frac{\partial E_z}{\partial x}\right)_D \tag{28}$$

Finite-difference approximations to the partial derivatives are substituted into the above equation. The approximating equations are similar to Equation (13) except that the third and fourth order terms are omitted. For example,

$$\left(\frac{\partial H_z}{\partial y}\right)_A = \frac{H_{z_1} h_3}{h_1(h_1+h_3)} - \frac{H_{z_{3_A}} h_1}{h_3(h_1+h_3)} + \frac{h_1-h_3}{h_1 h_3} H_{z_o} \tag{29}$$

where H_{z_1} is the longitudinal magnetic field component at node 1 and $H_{z_{3_A}}$ is the image longitudinal magnetic field value that would exist at node 3 if there was no dielectric present. This image potential is removed by solving the transverse Helmholtz equation

$$2\left(\frac{H_{z_1}}{h_1(h_1+h_3)} + \frac{H_{z_{3_A}}}{h_3(h_1+h_3)} + \frac{H_{z_2}}{h_2(h_2+h_4)} + \frac{H_{z_4}}{h_4(h_2+h_4)} - H_{z_o}\left(\frac{1}{h_1 h_3} + \frac{1}{h_2 h_4}\right)\right) = -k_a^2 H_{z_o} \tag{30}$$

which is valid at an air positioned node, for $H_{z_{3_A}}$ and substituting it into Equation (29). The result of substituting for all the derivatives into Equation (28) is an equation relating the longitudinal electric and magnetic fields at neighboring nodes to the longitudinal magnetic field at the center node of Figure 6. A normalized electric field is defined as

$$\bar{E}_{z_i} = \frac{\chi \omega \epsilon_o}{\beta} E_{z_i} \tag{31}$$

in order to absorb the unknown phase velocity ω/β and to introduce a scale factor X which is adjusted later to aid in the solution of the equations. The final result of Equation (28) is

$$H_{z_1}\left(\frac{2}{h_1(h_1+h_3)}\right) + H_{z_2}\left(\frac{2(h_1+Th_3)}{h_2(h_1+h_3)(h_2+h_4)}\right) + H_{z_3}\left(\frac{2T}{h_3(h_1+h_3)}\right) \qquad (32)$$

$$+ H_{z_4}\left(\frac{2(h_1+Th_3)}{h_4(h_1+h_3)(h_2+h_4)}\right) + H_{z_0}\left(\frac{-2(h_1+Th_3)}{(h_1+h_3)}\left(\frac{1}{h_1h_3}+\frac{1}{h_2h_4}\right)\right.$$

$$\left. + 2\,\frac{h_1-h_3}{h_1h_3}\,\frac{(1-T)}{(h_1+h_3)}\right) + 2\,\frac{(1-\kappa T)}{(h_1+h_3)}\left(\frac{\bar{E}_{z_4}h_2}{h_4(h_2+h_4)} - \frac{\bar{E}_{z_2}h_4}{h_2(h_2+h_4)} + \frac{h_4-h_2}{h_2h_4}\,\bar{E}_{z_0}\right)$$

$$= -k_a^2 H_{z_0}$$

Requiring continuity of the tangential component of the magnetic field yields

$$H_{x_{air}} = H_{x_{dielectric}} \qquad (33)$$

and in a manner similar to the previous derivation results in

$$-\beta\left(\frac{\partial H_z}{\partial x}\right)_A + \omega\epsilon_0\left(\frac{\partial E_z}{\partial y}\right)_A = -\beta T\left(\frac{\partial H_z}{\partial x}\right)_D + \omega\epsilon_0\kappa T\left(\frac{\partial E_z}{\partial y}\right)_D \qquad (34)$$

where the parameter $T = k_a^2/k_d^2$ is again used. Substitution for the partial derivatives and elimination of the image fields results in an equation relating the electric and magnetic fields at neighboring nodes to the electric field at the center node of Figure 6.

$$- \left(\frac{H_{z_4} h_2}{h_4 (h_2+h_4)} - \frac{H_{z_2} h_4}{h_2 (h_2+h_4)} + \frac{h_4 - h_2}{h_2 h_4} H_{z_0} \right) \frac{2(1-T)}{h_1+Kh_3} + \bar{E}_{z_1} \left(\frac{2}{h_1 (h_1+Kh_3)} \right) \quad (35)$$

$$+ \bar{E}_{z_2} \left(\frac{2(h_1+KTh_3)}{(h_1+Kh_3) h_2 (h_2+h_4)} \right) + \bar{E}_{z_3} \left(\frac{2KT}{h_3 (h_1+Kh_3)} \right)$$

$$+ \bar{E}_{z_4} \left(\frac{2(h_1+KTh_3)}{(h_1+Kh_3) h_4 (h_2+h_4)} \right) - \bar{E}_{z_0} \left(\frac{-2(h_1+KTh_3)}{(h_1+Kh_3)} \left(\frac{1}{h_1 h_3} + \frac{1}{h_2 h_4} \right) \right.$$

$$\left. + 2 \frac{(h_1-h_3)}{h_1 h_3} \frac{(1-KT)}{(h_1+Kh_3)} \right) = -k_a^2 \bar{E}_{z_0}$$

At the node where the edge of the center strip coincides with the air-dielectric interface, the boundary conditions are that $E_z = 0$ and that $\frac{\partial H_z}{\partial x} = 0$. The first condition is satisfied by requiring the electric field at that node to be zero and incorporating it into the equations for neighboring electric nodes and the adjacent magnetic node. The second condition is satisfied by requiring $H_{z_2} = H_{z_4}$ and $h_2 = h_4$ in Equation (32), resulting in

$$H_{z_1} \left(\frac{2}{h_1 (h_1+h_3)} \right) + H_{z_4} \left(\frac{2(h_1+Th_3)}{h_4^2 (h_1+h_3)} \right) + H_{z_3} \left(\frac{2T}{h_3 (h_1+h_3)} \right) \quad (36)$$

$$+ H_{z_0} \left(\frac{-2(h_1+Th_3)}{(h_1+h_3)} \left(\frac{1}{h_1 h_3} + \frac{1}{h_4^2} \right) + 2 \frac{h_1-h_3}{h_1 h_3} \frac{(1-T)}{(h_1+h_3)} \right)$$

$$+ \frac{(1-KT)}{h_1+h_3} \left(\frac{\bar{E}_{z_4}}{h_4} - \frac{\bar{E}_{z_2}}{h_4} \right) = -k_a^2 H_{z_0}$$

The edge of the center strip must terminate on a node.

This completes the formulation for the unequal node spacing of the finite-difference approximation to the transverse Helmholtz equation

which must hold at each node in the configuration.

Transverse Helmholtz Equations for Integral Multiple Spacing

If the node distribution is such that all node spacings are integral multiples of a basic spacing H, then the Helmholtz equations can be put into a slightly different form. For example, Equation (19) which applies at an air node, can be written as

$$2\left(\frac{\phi_1}{h_1H(h_1H+h_3H)}+\frac{\phi_2}{h_2H(h_2H+h_4H)}+\frac{\phi_3}{h_3H(h_1H+h_3H)}+\frac{\phi_4}{h_4H(h_2H+h_4H)}\right. \tag{37}$$

$$\left.-\phi_o\left(\frac{1}{h_1Hh_3H}+\frac{1}{h_2Hh_4H}\right)\right)=-k_a^2\phi_o$$

where h_1, h_2, h_3, and h_4 are now integers. Factoring out H^2 yields

$$2\left(\frac{\phi_1}{h_1(h_1+h_3)}+\frac{\phi_2}{h_2(h_2+h_4)}+\frac{\phi_3}{h_3(h_1+h_3)}+\frac{\phi_4}{h_4(h_2+h_4)}\right. \tag{38}$$

$$\left.-\phi_o\left(\frac{1}{h_1h_3}+\frac{1}{h_2h_4}\right)\right)=-k_a^2H^2\phi_o$$

All other nodal equations are modified in the exact same manner, i.e., k_a^2 and k_d^2 are replaced by $k_a^2H^2$ and $k_d^2H^2$, respectively. Once $k_a^2H^2$ and $k_d^2H^2$ are calculated for a general configuration of nodes, the solution can be scaled for any substrate thickness desired by specifying H and solving for k_a^2 and k_d^2.

Transverse Field Equations for Equal Spacing

The solution of the Helmholtz equations yields values for the longitudinal magnetic and scaled electric field intensities at each node.

Using Maxwell's equations, the transverse fields are found from the longitudinal fields. The equations were derived and listed as Equations (7). Recall the use of the scaled electric field

$$\bar{E}_{z_i} = \frac{\chi\omega\epsilon_o}{\beta} E_{z_i} . \tag{31}$$

Equations (7) in air then become

$$H_x = \frac{j\beta}{\chi k_a^2} \frac{\partial \bar{E}_z}{\partial y} - \frac{j\beta}{k_a^2} \frac{\partial H_z}{\partial x} \tag{39}$$

$$H_y = \frac{-j\beta}{\chi k_a^2} \frac{\partial \bar{E}_z}{\partial x} - \frac{j\beta}{k_a^2} \frac{\partial H_z}{\partial y}$$

$$E_x = \frac{-j\beta^2}{\omega\epsilon_o \chi k_a^2} \frac{\partial \bar{E}_z}{\partial x} - \frac{j\omega\mu_o}{k_a^2} \frac{\partial H_z}{\partial y}$$

$$E_y = \frac{-j\beta^2}{\omega\epsilon_o \chi k_a^2} \frac{\partial \bar{E}_z}{\partial y} + \frac{j\omega\mu_o}{k_a^2} \frac{\partial H_z}{\partial x}$$

and in the dielectric, Equations (7) become

$$H_x = \frac{j\beta\kappa}{\chi k_d^2} \frac{\partial \bar{E}_z}{\partial y} - \frac{j\beta}{k_d^2} \frac{\partial H_z}{\partial x} \tag{40}$$

$$H_y = \frac{-j\beta\kappa}{\chi k_d^2} \frac{\partial \bar{E}_z}{\partial x} - \frac{j\beta}{k_d^2} \frac{\partial H_z}{\partial y}$$

$$E_x = \frac{-j\beta^2}{\omega\epsilon_o \chi k_d^2} \frac{\partial \bar{E}_z}{\partial x} - \frac{j\omega\mu_o}{k_d^2} \frac{\partial H_z}{\partial y}$$

$$E_y = \frac{-j\beta^2}{\omega\epsilon_o \chi k_d^2} \frac{\partial \bar{E}_z}{\partial y} + \frac{j\omega\mu_o}{k_d^2} \frac{\partial H_z}{\partial x}$$

For node spacings that are integral multiples of a basic spacing H, artificial nodes can be placed between the original nodes to form a mesh of equally spaced nodes. The longitudinal field values at the intervening artificial nodes are found by simple interpolation. Thus, finite-difference equation approximations for the transverse fields need only be derived for equal node spacing, as shown in the node arrangement of Figure 7.

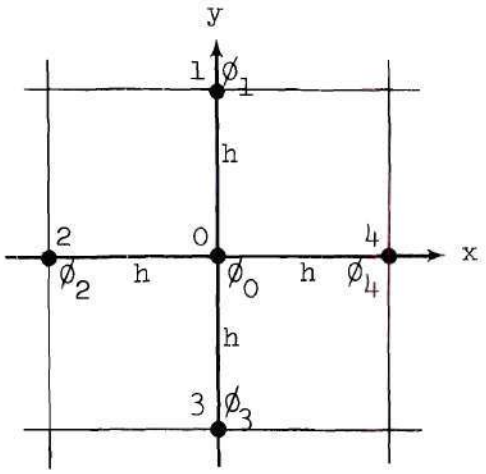

Figure 7. Node Arrangement for Equal Spacing

The central-difference equations for the partial derivatives are

$$\frac{\partial \phi}{\partial x} = \frac{\phi_4 - \phi_2}{2h} \tag{41}$$

and

$$\frac{\partial \phi}{\partial y} = \frac{\phi_1 - \phi_3}{2h} \tag{42}$$

For node positions located in air, the transverse fields are

$$H_x = \frac{j\beta}{\chi k_a^2}\left(\frac{\bar{E}_{z_1} - \bar{E}_{z_3}}{2h}\right) - \frac{j\beta}{k_a^2}\left(\frac{H_{z_4} - H_{z_2}}{2h}\right) \tag{43}$$

$$H_y = \frac{-j\beta}{\chi k_a^2}\left(\frac{\bar{E}_{z_4} - \bar{E}_{z_2}}{2h}\right) - \frac{j\beta}{k_a^2}\left(\frac{H_{z_1} - H_{z_3}}{2h}\right)$$

$$E_x = \frac{-j\beta^2}{\omega\epsilon_o \chi k_a^2}\left(\frac{\bar{E}_{z_4} - \bar{E}_{z_2}}{2h}\right) - \frac{j\omega\mu_o}{k_a^2}\left(\frac{H_{z_1} - H_{z_3}}{2h}\right)$$

$$E_y = \frac{-j\beta^2}{\omega\epsilon_o \chi k_a^2}\left(\frac{\bar{E}_{z_1} - \bar{E}_{z_3}}{2h}\right) + \frac{j\omega\mu_o}{k_a^2}\left(\frac{H_{z_4} - H_{z_2}}{2h}\right)$$

and in the dielectric

$$H_x = \frac{j\beta\kappa}{\chi k_d^2}\left(\frac{\bar{E}_{z_1} - \bar{E}_{z_3}}{2h}\right) - \frac{j\beta}{k_d^2}\left(\frac{H_{z_4} - H_{z_2}}{2h}\right) \tag{44}$$

$$H_y = \frac{-j\beta\kappa}{\chi k_d^2}\left(\frac{\bar{E}_{z_4} - \bar{E}_{z_2}}{2h}\right) - \frac{j\beta}{k_d^2}\left(\frac{H_{z_1} - H_{z_3}}{2h}\right)$$

$$E_x = \frac{-j\beta^2}{\omega\epsilon_o \chi k_d^2}\left(\frac{\bar{E}_{z_4} - \bar{E}_{z_2}}{2h}\right) - \frac{j\omega\mu_o}{k_d^2}\left(\frac{H_{z_1} - H_{z_3}}{2h}\right)$$

$$E_y = \frac{-j\beta^2}{\omega\epsilon_o \chi k_d^2}\left(\frac{\bar{E}_{z_1} - \bar{E}_{z_3}}{2h}\right) + \frac{j\omega\mu_o}{k_d^2}\left(\frac{H_{z_4} - H_{z_2}}{2h}\right)$$

Casting Finite-Difference Equations into a Matrix Eigensystem

Matrix Eigensystem Formulation

In order to determine the field configuration around microstrip,

the finite-difference equation approximation to the transverse Helmholtz equation at each node must be solved. Equations (19), (21), (24), (25), (32), and (35) are the difference equations for various boundary conditions which relate the field values at each node to the corresponding field values at neighboring nodes.

There are two scalar potentials superimposed on each other at each node. One potential corresponds to the scaled longitudinal electric field, $\bar{E}_z$, and the other potential corresponds to the longitudinal magnetic field, H_z. These fields are not directly coupled to each other, except along the air-dielectric interface where the equation for $\bar{E}_z$ at a node is in terms of the adjacent values of $\bar{E}_z$ and H_z. Likewise, the H_z equation is in terms of adjacent values of H_z and $\bar{E}_z$. Were it not for this interface coupling, each scalar potential set could be solved independently. This would, however, result in independent TE and TM mode solutions which would not satisfy the boundary conditions.

If there are n_1 nodes allowing for nonzero H_z values and n_2 nodes allowing for nonzero $\bar{E}_z$ values, then there will be $n = n_1+n_2$ separate nodal equations to be solved simultaneously. At a node in air, a typical magnetic field equation would be like Equation (24) with the ϕ_i replaced by H_{z_i} having the proper subscripts. For a node along the interface, the magnetic field coupling equation would be of the form of Equation (32) and the electric field coupling equation would be like Equation (35).

The set of linear simultaneous equations resulting from writing the equations at each of the n nodes in the dual mesh is of the form

$$A\Phi = -k_a^2\Phi \tag{45}$$

where A is an n × n square matrix given by Equation (46).

$$
\begin{array}{l}
a_{1,1}\ a_{1,2}\ 0\ldots0\ a_{1,b}\ 0\ldots\ldots\ldots

The coefficients of the coupling terms are designated with a circumflex. Φ is the vector whose components comprise the entire longitudinal field set.

$$\Phi = \begin{bmatrix} H_{z_1} \\ H_{z_2} \\ \cdot \\ \cdot \\ E_{z_n} \end{bmatrix} \tag{47}$$

Note that in the finite-difference equation development, the use of the parameter

$$T = \frac{k_a^2}{k_d^2} \tag{48}$$

allowed the set of simultaneous equations to be cast into the basic eigensystem form

$$(A - \lambda I)\ \Phi = 0 \tag{49}$$

where

$$\lambda = -k_a^2 \tag{50}$$

is the eigenvalue, Φ is the eigenvector, and I is the identity matrix.

General Eigensystem Form

The set of equations

$$(A + k_a^2 I)\ \Phi = 0 \tag{51}$$

is a set of simultaneous homogeneous linear equations. Nontrivial solutions exist for this set of homogeneous equations if the order n of the

matrix $(A + k_a^2 I)$ is greater than the rank[†] of the matrix. If the rank is n, the order of the matrix, the solution vector is unique and is the trivial solution, and the determinant of the coefficient matrix $(A + k_a^2 I)$ is nonzero. Since the trivial solution has no physical significance, nontrivial solutions whose coefficient matrix has a zero determinant are sought.

The determinant of the matrix $(A + k_a^2 I)$

$$|A + k_a^2 I| = \begin{vmatrix} (a_{11}+k_a^2) & a_{12} & a_{13} & \cdot & \cdot \\ a_{21} & (a_{22}+k_a^2) & a_{23} & \cdot & \cdot \\ a_{31} & a_{32} & (a_{33}+k_a^2) & \cdot & \cdot \\ \cdot & \cdot & \cdot & \cdot & \cdot \\ \cdot & \cdot & \cdot & \cdot & \cdot \end{vmatrix} = 0 \quad (52)$$

is after expansion an n^{th}-degree polynomial in k_a^2 called the characteristic equation,

$$(k_a^2)^n + C_1(k_a^2)^{n-1} + C_2(k_a^2)^{n-2} + \cdots\cdots\cdots + C_n(k_a)^0 = 0 \quad (53)$$

where $C_1, C_2, \ldots, C_n$ are constants. The roots of this n^{th}-degree polynomial equation are the eigenvalues, characteristic values, or latent roots, of the eigensystem of Equation (51). Direct solution of the characteristic equation for orders greater than three or four is, in general, very difficult. Methods for determining k_a^2 other than by calculating the roots of the characteristic equation will be investigated later.

[†]The rank of a matrix is the order of the largest nonzero determinant of submatrices formed by eliminating rows and columns. It is the number of linearly independent rows or columns of the matrix.

In many engineering problems, the rank of the matrix is usually n-1, thus corresponding to only one linearly dependent equation and n-1 independent equations in the set. Therefore, for a particular eigenvalue, by assuming any value for one component of the eigenvector, the other components can be found. The solution to such a system is determined to within a multiplicative constant.

For the eigensystem of Equation (51), composed of n equations, there are n mathematically acceptable eigenvalues. To each eigenvalue there corresponds an eigenvector such that Equation (51) is satisfied.

Node Numbering of the Configuration

The form of the coefficient matrix A depends upon how the nodes of Figure 2 are numbered. Two general methods were used. In the first form, the magnetic field matrix and electric field matrix are partitioned in the coefficient matrix but are coupled through the matrices C_1 and C_2.

$$A = \begin{bmatrix} H_z & C_1 \\ C_2 & E_z \end{bmatrix} \tag{54}$$

At any node in the configuration of Figures 8 and 9 the number above the node corresponds to the magnetic field node number and the number below the node corresponds to the electric field node number, with the exception that the only nodes on the center strip are magnetic nodes. For example, in order to generate the matrix A in the form of Equation (54), a simplified microstrip model would look like Figure 8.

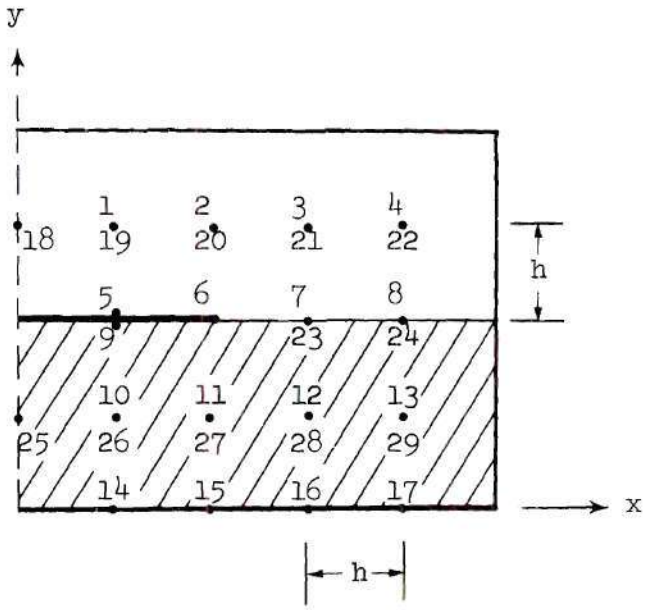

Figure 8. Simplified Microstrip Model with Node Numbering for a Partitioned Matrix

Nodes 12 and 28 physically occupy the same location; however, the equation for node 12 has the form of Equation (21), and is

$$\frac{H_{z_7}}{h^2} + \frac{H_{z_{11}}}{h^2} + \frac{H_{z_{13}}}{h^2} + \frac{H_{z_{16}}}{h^2} - H_{z_{12}}\left(\frac{4}{h^2}\right) = -k_d^2 H_{z_{12}} \tag{55}$$

Node 28 has the form similar to Equation (25), since it is next to a wall on which $E_z = 0$, and has the equation

$$\frac{\overline{E}_{z_{23}}}{h^2} + \frac{\overline{E}_{z_{27}}}{h^2} + \frac{\overline{E}_{z_{29}}}{h^2} - \overline{E}_{z_{28}}\left(\frac{4}{h^2}\right) = -k_d^2 \overline{E}_{z_{28}} \tag{56}$$

Recall that $\overline{E}_z$ is a scaled electric field.

$$\bar{E}_{z_i} = \frac{\chi \omega \varepsilon_0}{\beta} E_{z_i} \tag{31}$$

The reason for using the scale factor χ is best seen in Equation (54). Depending upon which values of T and κ are used, the coupling matrices can be such that, for example, only large numbers appear in C_1 compared with the small numbers that appear in C_2. The effect of this unbalance is that the eigenvector is then composed of approximately half large numbers and the other half small numbers which can reduce the accuracy in their calculation. A quick check of the interface equations indicates a good choice for χ, and thus helps make the solution calculations a bit more accurate.

Another way to number the nodes is shown in Figure 9. The same nodes considered previously

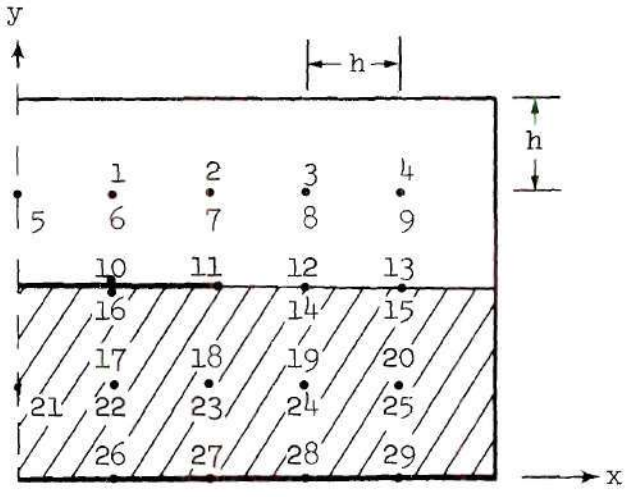

Figure 9. Simplified Microstrip Model with Node Numbering for a Band Matrix

are now nodes 19 and 24. The equation for node 19 is

$$\frac{H_{z_{12}}}{h^2} + \frac{H_{z_{18}}}{h^2} + \frac{H_{z_{20}}}{h^2} + \frac{H_{z_{26}}}{h^2} - H_{z_{19}}\left(\frac{4}{h^2}\right) = -k_d^2 H_{z_{19}} \tag{57}$$

and for node 24 is

$$\frac{\bar{E}_{z_{14}}}{h^2} + \frac{\bar{E}_{z_{23}}}{h^2} + \frac{\bar{E}_{z_{25}}}{h^2} - \bar{E}_{z_{24}}\left(\frac{4}{h^2}\right) = - k_d \bar{E}_{z_{24}} \tag{58}$$

In this form of numbering, the magnetic, electric, and coupling matrices cannot be partitioned, but rather are intermingled. The method does have some merit in that the matrix A is now a band matrix,† the band width being determined by the numbers of nodes used to model the microstrip. The scale factor X has the same exact purpose in the band matrix as it does in the former partitioned matrix.

Specification of Coefficient Matrix

With either form of the coefficient matrix decided upon, all that remains is to determine the numbers that fill each matrix element. After specification of the node spacing and dielectric constant, T alone re-

---

†A band matrix is one where all nonzero matrix elements lie between a lower diagonal and an upper diagonal, e.g.

$$B = \begin{bmatrix} X & X & 0 & 0 & 0 & 0 \\ X & X & X & 0 & 0 & 0 \\ 0 & X & X & X & 0 & 0 \\ 0 & 0 & X & X & X & 0 \\ 0 & 0 & 0 & X & X & X \\ 0 & 0 & 0 & 0 & X & X \end{bmatrix}$$

B is a band matrix having a band width of 3.

mains. Recall that T was the parameter defined in Equation (27) as

$$T = \frac{k_a^2}{k_d^2} = \frac{\omega^2\mu_o\epsilon_o - \beta^2}{\omega^2\mu_o\epsilon_o\kappa - \beta^2} \quad . \tag{27}$$

Since the microstrip medium is composed of two homogeneous dielectric regions, the phase constant, β, will lie between that for a homogeneous air medium $\beta_{air} = \omega\sqrt{\mu_o\epsilon_o}$ and a homogeneous dielectric medium $\beta_{dielectric} = \omega\sqrt{\mu_o\epsilon_o\kappa}$.

$$\omega^2\mu_o\epsilon_o < \beta^2 < \omega^2\mu_o\epsilon_o\kappa \tag{59}$$

This constrains k_a^2 to be negative, since

$$k_a^2 = \omega^2\mu_o\epsilon_o - \beta^2 \tag{60}$$

and constrains k_d^2 to be positive since

$$k_d^2 = \omega^2\mu_o\epsilon_o\kappa - \beta^2 \tag{61}$$

Thus T is chosen to be a negative number, and the coefficient matrix is completely specified. Rewrite Equation (27) as

$$T = \left(\frac{\beta_o^2}{\beta^2} - 1\right)\Big/\left(\frac{\beta_o^2}{\beta^2}\kappa - 1\right) = \left(\frac{\lambda_o^2}{\lambda_o^2} - 1\right)\Big/\left(\frac{\lambda_o^2}{\lambda_o^2}\kappa - 1\right) \tag{62}$$

where

$$\beta_o^2 = \omega^2\mu_o\epsilon_o = (2\pi/\lambda_o)^2 \tag{63}$$

and

$$\beta = 2\pi/\lambda_g \tag{64}$$

Specifying a value for T sets explicitly the particular β/β_o or λ_g/λ_o ratio that will characterize the solution.

The coefficient matrix is real (since losses are neglected), non-symmetric (due to the boundary conditions), and sparse (since the microstrip is modeled with finite-difference equations).

Eigensystem Solutions

After complete specification of the matrix, the eigensystem is solved to determine first the positive eigenvalue,

$$\lambda = -k_a^2 \tag{65}$$

and then the eigenvector,

$$\Phi = \begin{bmatrix} H_{z_1} \\ H_{z_2} \\ \vdots \\ E_{z_n} \\ \vdots \end{bmatrix} \tag{47}$$

From Equation (27), k_d^2 is determined,

$$k_d^2 = \frac{k_a^2}{T} \tag{66}$$

and Equations (60) and (61) are then solved simultaneously to determine the frequency of operation,

$$f = \frac{1}{2\pi\sqrt{\mu_o \epsilon_o}} \sqrt{\frac{k_a^2(1-1/T)}{(1-K)}} \tag{67}$$

and the phase constant of the propagating mode,

$$\beta = \sqrt{-k_a^2 \left(\frac{K+1/T}{K+1}\right)} \tag{68}$$

Since the matrix is real and nonsymmetric and since the main diagonal changes sign, the n mathematically allowable eigenvalues of the n x n matrix are real or occur in complex conjugate pairs.[25] However, only those that are positive correspond to Equations (65) and (59) and can be considered in determining the dominant mode. Negative eigenvalues for a negative T result in the contradicting requirement of $\beta^2 < \omega^2 \mu_o \epsilon_o$ and $\beta^2 > \omega^2 \mu_o \epsilon_o K$.

Methods of Solution of Matrix Eigensystems

There are two classes of techniques used to solve the matrix eigenvalue problem; the indirect method and the direct method. The indirect method is an iterative process which can converge to the lowest eigenvalue and corresponding eigenvector. There is another iterative method, the power method, which can converge to the largest eigenvalue and corresponding eigenvector. The direct method, on the other hand, generates all the eigenvalues and as many corresponding eigenvectors as wanted.

Indirect Method

In many eigensystem problems which have large coefficient matrices,

there is a practical advantage to using the indirect method as opposed to the direct method. The direct method, by its very nature, requires the entire coefficient matrix to be readily accessible when calculating the eigenvalues and eigenvector. When using digital computers, this requires a considerable amount of core memory merely to store the matrix. The indirect method circumvents this requirement in that only one row of the coefficient matrix is needed at any one time, and only then is it generated. This greatly reduces the computer storage requirements, and thus a substantially larger eigenvector is available for use and storage. With the indirect method, the finite-difference equation approximations to the scalar Helmholtz equations which apply at each node are solved for the scalar field (electric or magnetic) at the center node in terms of the surrounding scalar field values. For example, Equation (22) for a magnetic node in air would be rewritten as

$$H_{z_o} = \frac{H_{z_1} + H_{z_2} + H_{z_3} + H_{z_4}}{(4 - h^2 k_a^2)} \tag{69}$$

An initial guess for the eigenvalue $-k_a^2$ and eigenvector Φ is made and the iteration begins. The first magnetic node is updated by substituting the field values of the surrounding magnetic nodes and the guessed eigenvalue into the difference equation corresponding to that particular node. The new field value is calculated and it then replaces the value previously associated with that node. The next magnetic node is updated by substituting into its relevant equation the newly calculated magnetic field value and the adjacent field values. This procedure is continued until all magnetic and electric field node values have been recalculated.

A complete pass through the n potentials is termed an iteration.

After several iterations, the electric and magnetic fields tend to assume the correct relative values with respect to each other even with an inaccurately guessed eigenvalue. With an improved estimate on the eigenvector, the guessed eigenvalue needs correcting so that it is nearer the true eigenvalue.

There is a procedure for determining an improved value for the guessed eigenvalue which depends only upon the relative field values. The Rayleigh quotient[26]

$$\lambda = \frac{\Phi^T A \Phi}{\Phi^T \Phi} \tag{70}$$

where

$$\Phi^T = (H_{z_1}, H_{z_2}, H_{z_3}, \ldots\ldots\ldots, \overline{E}_{z_n}) \tag{71}$$

is the transpose of Φ, gives the new estimate of the eigenvalue λ based on the eigenvector Φ generated by the last iteration. Using this improved estimate for the eigenvalue, the iteration technique is performed several times. Again the Rayleigh quotient is applied to improve the eigenvalue based now on the improved relative field values. The entire process is repeated until convergence is hopefully obtained.

Fox[27] has stated that the Rayleigh quotient has no particular virtue for matrices lacking symmetry. Forsyth and Wasow[28] proved that, unless the coefficient matrix is diagonally dominant,† convergence via

---

†A diagonally dominant matrix is one for which the matrix elements, a_{ij}, satisfy

$$|a_{ii}| > \sum_{\substack{k=1 \\ k \neq i}}^{n} |a_{ik}|, \quad i = 1,2,\ldots,n$$

the iterative indirect technique is not guaranteed. Since the matrix which models the microstrip is not diagonally dominant and is nonsymmetric, there is no way to guarantee convergence of the eigenvector or of the Rayleigh quotient.

The unloaded waveguide problem has been cast into the matrix eigensystem form and solved by Davies and Muilwyk[29] using this iterative process. However, the coefficient matrix resulting from the finite-difference approximations was symmetric and diagonally dominant, thus guaranteeing convergence to the lowest propagating mode. Their method utilized successive-over-relaxation to speed convergence.

Convergence by the indirect method cannot be guaranteed for the microstrip problem, but there is no proof that it will not converge. The indirect method was applied to several matrices modeling the microstrip. It was found that, if the order of the coefficient matrix was around 30 or less, the relaxation procedure would converge, but for matrices of order greater than 30, convergence could not be obtained, regardless of the eigenvector accuracy. As a final check, a matrix of order of about 100 whose eigenvalue and eigenvector were known was considered. The guessed eigenvalue was the correct one and the initial components of the guessed eigenvector were set very close to the known values, but the relaxation process diverged away from the known solution and never did converge, even after several thousand iterations.

This indirect method, when it converges, does so to the lowest eigenvalue and eigenvector. Thus the other n-1 eigenvalues and eigenvectors are obscured.

The indirect method was abandoned in favor of a direct method for this work since the lack of convergence prevented successful application of the technique.

Direct Method

The direct method is the best way to calculate all the eigenvalues of a matrix eigensystem. However, since the complete coefficient matrix must be accessible, there is an upper limit to the size matrix which can be retained in the computer memory core.

Starting with Equation (51)

$$(A + k_a^2 I)\ \Phi = 0 \tag{51}$$

we are interested in finding the n values of k_a^2 which satisfy it. The QR transform was chosen since it is considered to be the best method available for calculating the eigenvalues of a general matrix. The QR transform was developed and after a long experimental period was published by Francis.[30,31] It is briefly outlined in Appendix B.

Eigenvalue Calculations. The coefficient matrix of Equation (51) has been shown to be a real, nonsymmetric, and sparse matrix. This matrix A is transformed initially to an upper Hessenberg matrix or sometimes called an almost triangular matrix, $A^{(1)}$. This reduction is done by the Householder method[32] using similarity transforms.† The matrix has a special form in which all elements below the first subdiagonal are zero. Since $A^{(1)}$ is similar to A, the eigenvalues of $A^{(1)}$ are exactly

---

†B^{-1} A B is a similarity transform of A.

those of A.

$$A^{(1)} = \begin{bmatrix} X & X & X & X & X & X \\ X & X & X & X & X & X \\ 0 & X & X & X & X & X \\ 0 & 0 & X & X & X & X \\ 0 & 0 & 0 & X & X & X \\ 0 & 0 & 0 & 0 & X & X \end{bmatrix} \tag{72}$$

The theory of the QR transform is that any matrix A can be decomposed into the product of a unitary matrix[†] Q and an upper triangular matrix R. The transform consists of forming a sequence of matrices

$$A^{(k+1)} = Q^{(k)*} A^{(k)} Q^{(k)} \tag{73}$$

where the superscript k keeps track of the iterations. It is done by pre-multiplying $A^{(k)}$ by a unitary matrix $Q^{(k)*}$ chosen so as to reduce $A^{(k)}$ to the upper triangular form $R^{(k)}$. Next post-multiply $R^{(k)}$ by $Q^{(k)}$ to get $A^{(k+1)}$. The transform can be written as a similarity transform,

$$A^{(k+1)} = Q^{(k)*} Q^{(k-1)*} \cdots Q^{(1)*} A^{(1)} Q^{(1)} Q^{(2)} \cdots Q^{(k)} \tag{74}$$

As $k \to \infty$, the matrix $A^{(k)}$ tends to upper triangular whereupon the diagonal elements are the eigenvalues of A.

In order to speed convergence the origin of the eigenvalues is shifted by the amount $k_s^{(k)}$ before the iteration and shifted back after the iteration, thus making the transform become

---

[†]U is a unitary matrix if $U^{-1} = U^*$ where the asterisk implies the complex conjugate transpose of the matrix.

$$A^{(k)} - k_s^{(k)}I = Q^{(k)}R^{(k)} \qquad R^{(k)}Q^{(k)} + k_s^{(k)}I = A^{(k+1)} \tag{75}$$

or

$$A^{(k+1)} = Q^{(k)*}A^{(k)}Q^{(k)} \tag{76}$$

where

$$Q^{(k)*}\left(A^{(k)} - k_s^{(k)}I\right) = R^{(k)} \tag{77}$$

The iteration procedure is not changed except for the shift.

If the matrix is real but nonsymmetric, as A is in Equation (51), then complex eigenvalues which require complex shifts are allowable. Francis developed a form of the QR transform which performs two iterations at one time, thus eliminating the need for complex matrices. The transform is defined by

$$A^{(k)} - k_s^{(k)}I = Q^{(k)}R^{(k)} \qquad R^{(k)}Q^{(k)} + k_s^{(k)}I = A^{(k+1)} \tag{78}$$

$$A^{(k+1)} - k_s^{(k+1)}I = Q^{(k+1)}R^{(k+1)} \qquad R^{(k+1)}Q^{(k+1)} + k_s^{(k+1)}I = A^{(k+2)}$$

or

$$A^{(k+2)} = \left(Q^{(k+1)}Q^{(k)}\right)^* A^{(k)}\left(Q^{(k)}Q^{(k+1)}\right) \tag{79}$$

where the possibly complex matrices $Q^{(k)}$, $Q^{(k+1)}$, $R^{(k)}$, and $R^{(k+1)}$ are not explicitly calculated and, as a result, all calculations are performed in the real field.

The technique for a double iteration is to perform an initial similarity transformation on $A^{(k)}$ and then reduce the resulting matrix to upper Hessenberg form by Householder's method. This yields $A^{(k+2)}$,

the matrix which would be obtained after two iterations of the QR transform. After each double iteration, the subdiagonal elements are inspected. If $a^{(k)}_{n,n-1}$ is zero, then $a^{(k)}_{n,n}$ is accepted as an eigenvalue and the matrix is deflated by eliminating the last row and column. If $a_{n-1,n-2}$ is zero, the eigenvalues of the bottom 2 x 2 submatrix are accepted as eigenvalues and the last two rows and columns are eliminated. If either is zero, do the following: accept the eigenvalue, deflate the matrix and start another double iteration on the reduced matrix. If neither is zero, proceed with another double iteration. The process is continued until the matrix has been reduced to either a 2 x 2 matrix from which the eigenvalues are directly calculated or a 1 x 1 matrix which is the last eigenvalue. Starting with the n x n coefficient matrix, repeated application of the double QR transform results in the n eigenvalues satisfying Equation (51).

Eigenvector Calculations. The best method for determining the eigenvector corresponding to a particular eigenvalue is the Wielandt iteration or inverse iteration technique.[33] With this procedure, one iterates with $(A - pI)^{-1}$ for a value of p where A is the coefficient matrix and p is close to the eigenvalue. Inverse iteration is effective with a full matrix, but if A is reduced to upper Hessenberg form $A^{(1)}$ at the start, the process is far more efficient.

The iteration is expressed in the form

$$\Phi^{(k+1)} = \left(A^{(1)} - pI\right)^{-1} \Phi^{(k)} \qquad (80)$$

where $\Phi^{(k)}$ is the eigenvector after the k^{th} iteration. In practice, it is better to rearrange Equation (80) to

$$\Phi^{(k)} = \left(A^{(1)} - pI\right) \Phi^{(k+1)} \tag{81}$$

The eigenvalues of $(A^{(1)} - pI)^{-1}$ are $(\lambda-p)^{-1}$. If p is a close approximation to λ, but not to any other of the eigenvalues of $A^{(1)}$, then $(\lambda-p)^{-1}$ is much larger than the other eigenvalues. By iterating with $(A^{(1)} - pI)^{-1}$, rapid convergence to $\Phi^{(k)}$ is obtained, since this is the corresponding eigenvector of $(A^{(1)} - pI)^{-1}$ as well as that of A.

Beginning with an arbitrary eigenvector $U^{(0)}$ for the eigenvalue λ,

$$(A^{(1)} - \lambda I)\ \Phi^{(1)} = U^{(0)} \tag{82}$$

is solved directly via Gaussian elimination with partial pivoting for $\Phi^{(1)}$. The element of maximum modulus $M^{(1)}$ of the solution vector $\Phi^{(1)}$ is then determined. An improved estimate of the eigenvector will be

$$U^{(1)} = \Phi^{(1)}/M^{(1)} \tag{83}$$

With a forward substitution of $U^{(1)}$ into Equation (82)

$$(A^{(1)} - \lambda I)\ \Phi^{(2)} = U^{(1)} \tag{84}$$

is solved for $\Phi^{(2)}$ as before with partial pivoting and back substitution.

This iteration process converges to that eigenvector corresponding to the accurate approximation of the eigenvalue λ. Although $(A^{(1)} - pI)$ is almost singular when λ is close to p, this does not affect the accuracy of the process.

The eigenvector components correspond physically to the longitudinal magnetic and scaled electric field magnitudes at the nodes in the microstrip configuration. The longitudinal electric field is calculated from

$$E_{z_i} = \frac{\beta}{\chi\omega\epsilon_o} \bar{E}_{z_i} \tag{85}$$

Errors in Numerical Analysis

There are several types of errors which can cause the numerical answers to problems to deviate from the true solution. Since an analytical solution to the microstrip problem has not been found, it is necessary to compare the numerical answers with experimental results in order to determine what error exists. The errors in the theoretical results are classed in two areas; those that are inherent in the mathematical formulation and those that arise in actually calculating the numerical solutions on a computer.

Errors in the Mathematical Formulation

Three types of errors arise in formulating the mathematical model. The specification of the dielectric constant may be in error by as much as five percent. This type of error is classed as an error due to the inaccuracies of the physical data.

Physical Situation Approximations. Errors arise whenever a mathematical model is used to approximate the physical situation. For example, the assumption that the center strip is infinitely thin is not completely accurate. There is a slight error introduced when the conductivity of the center strip and ground plane and the loss tangent of the dielectric substrate are assumed negligible. The largest contributor to error in this group is that error which arises when the open microstrip configuration is bounded by the electric and magnetic walls, thus requiring the longitudinal fields to approach zero a finite distance away from the center strip. Only if an extremely large bounding box were allowed would the error introduced by this boundary condition become completely negligible.

Finite-Difference Approximations. The major contribution to total error is mesh or truncation error. It arises from the replacement of the elliptical differential equation by a finite-difference equation. In particular, at the node points of the modeled configuration, the first and second order partial derivatives are replaced by the truncated infinite series to get the finite series approximation, as in Equations (13) and (14).

With respect to the node arrangement of Figure 3, the finite-difference approximation for the first order derivative is, from Equation (13)

$$\left(\frac{\partial \phi}{\partial x}\right)_o = \left(\frac{h_2 h_4}{h_2+h_4}\right)\left(\frac{\phi_4}{h_4^2} - \frac{\phi_2}{h_2^2} - \phi_o\left(\frac{1}{h_4^2} - \frac{1}{h_2^2}\right)\right) - R \qquad (86)$$

where the remainder

$$|R| \leq \frac{1}{6} h^2 M_3 \tag{87}$$

if

$$h \geq \max(h_4, h_2) \tag{88}$$

M_k, $k = 1,2,3,\ldots$ denotes the supremum of absolute values of all the partial derivatives of $\Phi(x,y)$ of order k in the interval of interest. The largest term of the error in the finite-difference form of the equation contains the factor h^2. Thus the approximation has an error $O(h^2)$ as $h \to 0$.

Considering Equation (8), it is obvious that the forward difference approximation to the derivative is

$$\left(\frac{\partial \phi}{\partial x}\right)_o = \frac{\phi_4 - \phi_o}{h} + O(h) \tag{89}$$

The backward difference derivative also has an error of order h.

The second order derivative is from Equation (14)

$$\left(\frac{\partial^2 \phi}{\partial x^2}\right)_o = 2\left(\frac{\phi_4}{h_4(h_2+h_4)} + \frac{\phi_2}{h_2(h_2+h_4)} - \frac{\phi_o}{h_2 h_4}\right) + R \tag{90}$$

where

$$|R| \leq \frac{1}{3} hM_3 + \frac{1}{12} h^2 M_4 \tag{91}$$

if

$$h \geq \max(h_4, h_2) \tag{92}$$

Here the largest term of the remainder has a leading factor of h. Thus the approximation has an error $O(h)$ as $h \to 0$. For an equally spaced net, $h = h_2 = h_4$, and

$$\left(\frac{\partial^2 \phi}{\partial x^2}\right)_0 = \frac{\phi_4 + \phi_2 - 2\phi_0}{h^2} + R \tag{93}$$

where

$$|R| \leq \frac{1}{12} h^2 M_4 \tag{94}$$

Equations (91) and (94) show the advantage of using equally spaced nets, in that the error term in the finite-difference expressions drops from $O(h)$ to $O(h^2)$, as $h \to 0$, when $h = h_2 = h_4$.

Whenever there is a reentrant corner, which appears here as the edge of the center strip, the finite-difference approximation suffers since Taylor's expansion is inaccurate, due to the unbounded nature of the field derivatives near the singularity. Sinnott, et al.[34] have stated that, for solutions whose order of error is normally $O(h^2)$, if a thin edge is present, the dominant error term is $O(h)$ rather than $O(h^2)$.

According to Green,[35] there is no purely theoretical way to determine the percent error to be anticipated when finite-difference techniques are employed. The most positive way to determine an estimate of error is to make a numerical evaluation of a problem which can be solved analytically and then compare results. In some cases, the numerical evaluation can be compared with experimental results. Another technique when using finite-difference equations is to halve the spacing between nodes, solve the problem a second time and observe the percentage change

in results. A small change would imply that the difference approximations are adequate and that further reduction in mesh size is not necessary.

Walsh[36] has pointed out that, since an estimate of the error can not be made, then an upper bound would be helpful but that we are a long way from achieving this in the field of partial differential equations. Upper bounds for the error can generally be obtained in terms of the quantities such as M_2 and M_3, but these quantities are seldom known. It has been proved that, under quite general conditions, the error does tend to zero as the mesh size, h, approaches zero.[37]

Computational Error

The errors which occur in calculating a solution to a numerical problem on a digital computer are generally referred to as roundoff error. One type of roundoff error occurs when the computer handles a fraction which transforms to a nonterminating decimal. The fraction is not accurately represented. When a number is stored in the computer, there are only k digits available when working in single precision. The accumulation of the effects of restricting these numerical values to the finite number of places results in a roundoff error which can build up after a large number of operations.

The only place roundoff error could be of consequence in this dissertation is in the QR algorithm and the inverse iteration algorithm. In his work on the QR algorithm, Francis[38] points out that, since there are basically two stages in determining eigenvalues, reduction to upper Hessenberg form and the actual QR iteration, and since neither involves

the use of multiples greater than one, then roundoff error builds up only gradually. In the inverse iteration algorithm, the same applies in the reduction to upper Hessenberg form, and since partial pivoting is used in the Gaussian elimination, roundoff errors should build up only gradually there also.

CHAPTER III

NUMERICAL CALCULATIONS

Calculation Procedures

A theoretical eigensystem approach for the determination of the dominant mode's f-β diagram and field configuration in microstrip was outlined in Chapter II. This method of solution of the eigensystem, the direct method, required millions of calculations. Moreover, the same procedure was repeated for different values of relative dielectric constant, substrate thickness, and strip width to substrate thickness ratio. In addition, each combination of the above parameters was considered at several frequencies in the microwave spectrum. This large number of calculations prohibited computing the solution by hand. Consequently, a high speed digital computer was used.

Computer Requirement

Since direct methods were employed to calculate the eigenvalues and eigenvectors, all elements of the large coefficient matrix, A, in Equation (51) of Chapter II

$$(A + k_a^2 I)\ \Phi = 0 \qquad (1)$$

have to be stored in the memory core of the digital computer. This requirement necessitates the use of a computer with at least fifty thousand words of usable core. Based on the number of calculations involved, the

computer needs to be a high speed machine. It must also carry at least seven decimal places when representing a number and be capable of operating in double precision.

Computer Programs and Program Sequencing

Matrix Generation. The coefficient matrix A of Equation (1) was generated by a program which was written to allow for easily changing the modeling configuration, dielectric constant and frequency. The technique was to determine the finite-difference equations which represented all of the possible individual node configurations that were encountered when describing the microstrip. These equations were programmed as functions of the node spacing parameters h_i, $i = 1, 2, 3$, and 4, the parameter T, and the relative dielectric constant K.

The first step in the matrix generation was to read into the computer values for T and K. Then for each of the n electric and magnetic nodes, the node number, the node numbers of the adjacent nodes, the node's spacing parameters, and a label number which directed the computer to the finite-difference equation that applied to that particular node were read into the computer. In effect, each row of the matrix A was generated in turn until the entire matrix was filled according to the specifications of that particular problem. For a specific configuration, the frequency and/or relative dielectric constant was varied by simply changing the initial data card and recomputing the matrix.

After the matrix was generated, the trace† of the matrix A was

---

†The trace of A is the sum of the diagonal elements

$$a_{11} + a_{22} + a_{33} + \cdots + a_{nn} = \sum_{k=1}^{n} a_{kk}$$

computed. The matrix was then transformed into an upper Hessenberg matrix $A^{(1)}$ whose form is given by Equation (72) of Chapter II. The trace of $A^{(1)}$ was then computed and compared with the previously calculated trace of A. Since the two matrices A and $A^{(1)}$ were similar, the traces of the two matrices should be equal.†

Eigenvalue Computations. The eigenvalues were calculated by two subroutines. One performed the actual double QR transform, and the other subroutine was a control program that tested for convergence and made the decision when to accept the eigenvalues which were calculated. After all the eigenvalues had been calculated they were summed. The sum of the eigenvalues equaled the trace of the original and upper Hessenberg matrix provided all calculations were performed accurately. This was true since the QR transform reduced the matrix $A^{(1)}$ to a similar triangular matrix which had as its eigenvalues the diagonal elements. The basic QR algorithm programmed in Fortran was obtained from the University of Tennessee SHARE library.

Eigenvector Computations. The eigenvector corresponding to any one of the eigenvalues could now be calculated. The n component eigenvector

$$\Phi^T = (H_{z_1}, H_{z_2}, \cdots, \bar{E}_{z_n}) \tag{2}$$

was calculated by the inverse iteration technique in which the eigenvector was normalized to its component of largest modulus. The inverse

---

†The matrices might differ slightly due to roundoff error. A large difference would imply that the computer had made an error which had not been detected and corrected by the computer's own control program.

iteration subroutine in Algol was obtained from the Georgia Tech computer library.

f-β Computations. In order to calculate the frequency f and phase constant β corresponding to a particular eigenvalue λ, initially the value of k_a^2 had to be determined.

$$k_a^2 = -\frac{\lambda}{H^2} \tag{3}$$

(Recall that all the node spacings are an integral multiple of a basic node spacing H which is determined when the substrate thickness is specified.) Then the frequency and phase constant were calculated from Equations (67) and (68) of Chapter II, which are repeated here.

$$f = \frac{1}{2\pi\sqrt{\mu_o \epsilon_o}}\sqrt{\frac{k_a^2(1-1/T)}{(1-K)}} \tag{4}$$

$$\beta = \sqrt{-k_a^2\left(\frac{K+1/T}{K+1}\right)} \tag{5}$$

True Longitudinal Field Computations. The eigenvector, Equation (2), contains the components of the true longitudinal magnetic field and the scaled longitudinal electric field. The true electric fields E_{z_i} are related to the scaled electric fields $\bar{E}_{z_i}$ by the following equation.

$$E_{z_i} = \frac{\beta}{X\omega\epsilon_o}\bar{E}_{z_i} \tag{6}$$

The scale factor X was specified at the beginning of the calculations,

and f and β were calculated from Equations (4) and (5) above.

Transverse Field Computations. Another subroutine used the above calculated eigenvalue, frequency, phase constant, and eigenvector to compute the transverse fields via Equations (43) and (44) of Chapter II. Equation (6) was incorporated into the subroutine so that the final listing was the electric and magnetic field components at each node. The magnitude and direction of the transverse electric and magnetic field vectors were also computed.

Numerical Results

Numerical calculations were made for microstrip configurations having ratios of strip width w to substrate thickness b of one and two. A detailed discussion of the numerical results for the .055" alumina substrate with a w/b = 2 follows. The calculated eigenvalues and eigenvectors are initially discussed. Next the calculated f-β diagram is presented and discussed. Then the calculated transverse fields are presented. Finally, the mode pattern of the total magnetic field is discussed.

The nodal distribution and numbering for this w/b = 2 configuration are shown in Figure 10. The number above the node corresponds to the magnetic field node number and the number below corresponds to the electric field node number with the exception that all nodes on the metal surfaces (center strip and ground plane) correspond to magnetic nodes. There are 147 electric and magnetic nodes, and so the resulting coefficient matrix of the eigensystem has an order of 147.

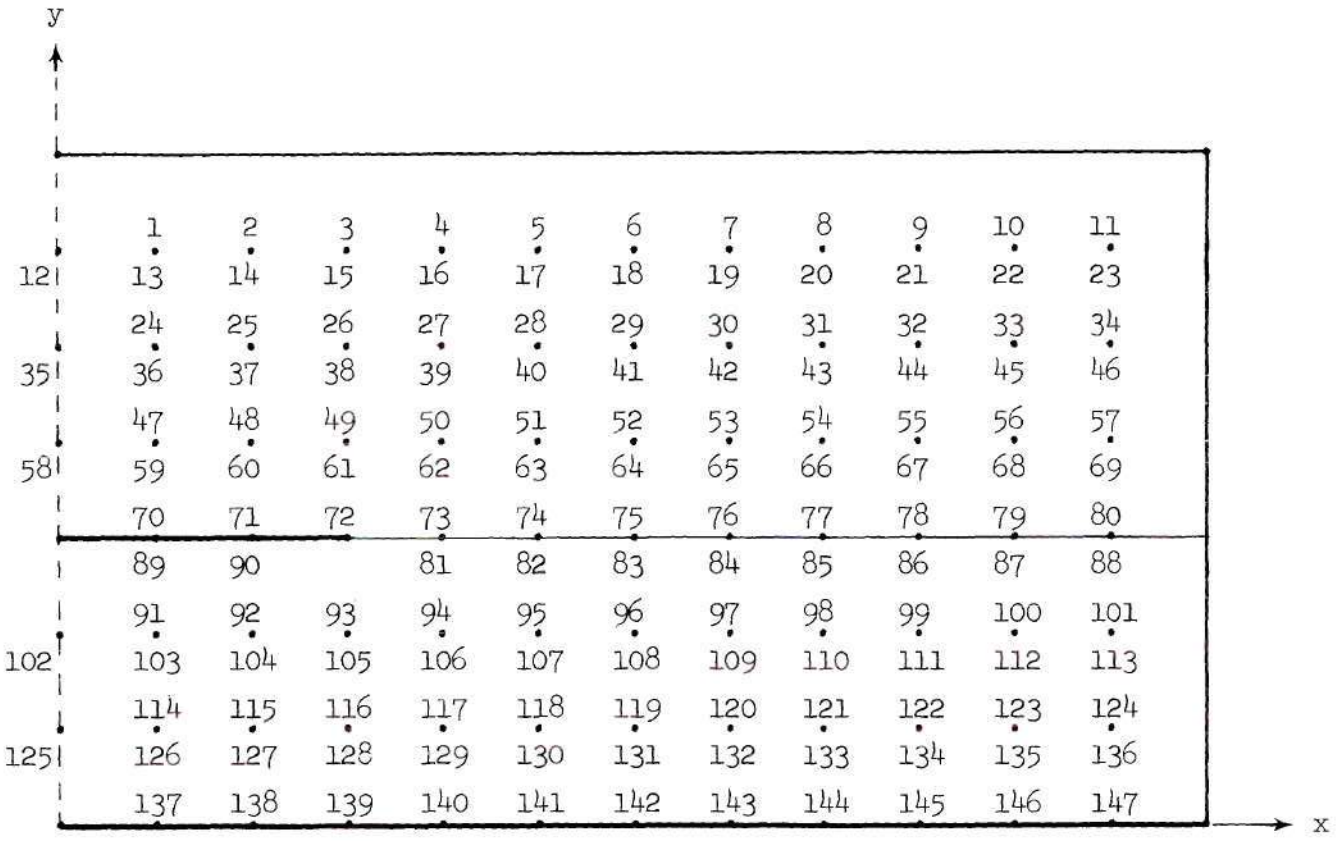

Figure 10. Microstrip Model for w/b = 2

Eigenvalues

The previously outlined procedures were used to calculate the 147 mathematically acceptable eigenvalues of A for values of T, -3 to -11. For each value of T, the number of positive and negative eigenvalues was approximately the same. The listing of the eigenvalues of small modulus has a rather interesting form as seen in Table 1.

Table 1. Eigenvalues of Small Modulus for Several Values of T for an Alumina Substrate with w/b = 2

Eigenvalues					T
1	2	3	4	5	
3.14310	1.08030	0.10135	± j0.03254	-0.60693	-11.0
2.76580	0.91336	0.09478	0.03646	-0.60718	-10.0
2.38740	0.74738	0.08230	-0.02265	-0.60748	- 9.0
2.00780	0.58278	0.06195	-0.07444	-0.60783	- 8.0
1.62720	0.42027	0.03778	-0.12385	-0.60826	- 7.0
1.24550	0.26150	0.00974	-0.17297	-0.60878	- 6.0
0.86364	0.11233	-0.02702	-0.22425	-0.60945	- 5.0
0.48463	0.00048	-0.09969	-0.09969	-0.61037	- 4.0
0.12759	-0.06881	-0.22446	-0.36329	-0.61175	- 3.0

An important point to observe is that the lowest positive eigenvalue breaks from column to column as T is varied.

Observe the variation of the eigenvalues in Table 1 as a function of T, i.e. in each of the first four columns, positive eigenvalues approach and pass through zero as T is varied down to -3. This behavior

would suggest the possibility of each column corresponding to some type of mathematical mode. The negative eigenvalues in the positive columns approach zero for T of increasing magnitude, while there is a column of negative eigenvalues (column 5 of Table 1) which changes less than one percent as T varies from -3 to -11. This implies that, for higher values of T, no new columns of positive eigenvalues will appear. This was verified for values of T up to -25.

The complex conjugate eigenvalues which occurred at T = -11, in Table 1, might seem to imply a coupling of two mathematical modes. However, in the experimental work such coupling has not been observed to occur in microstrip at the frequencies calculated. Other microstrip experimental investigators have not reported the simultaneous existence of two such modes and their consequent coupling at X-band. Calculations of the eigenvalues for a w/b = 1 configuration for matrices of order 147 and 185 did not reveal any such phenomena. Waveguide enclosed microstrip calculations also did not exhibit these complex eigenvalues. Thus, no physical evidence to substantiate the existence of these coupled modes is presently available.

Eigenvectors

The eigenvector corresponding to the lowest positive eigenvalue for T = -9 is displayed in Figure 11. The values above the nodes are the magnetic field values and those below are the electric field values.

An eigenvector, corresponding to an eigenvalue in each of the four positive columns of Table 1, was calculated and is plotted along the air-dielectric interface in Figures 12, 13, 14, and 15. The eigenvector

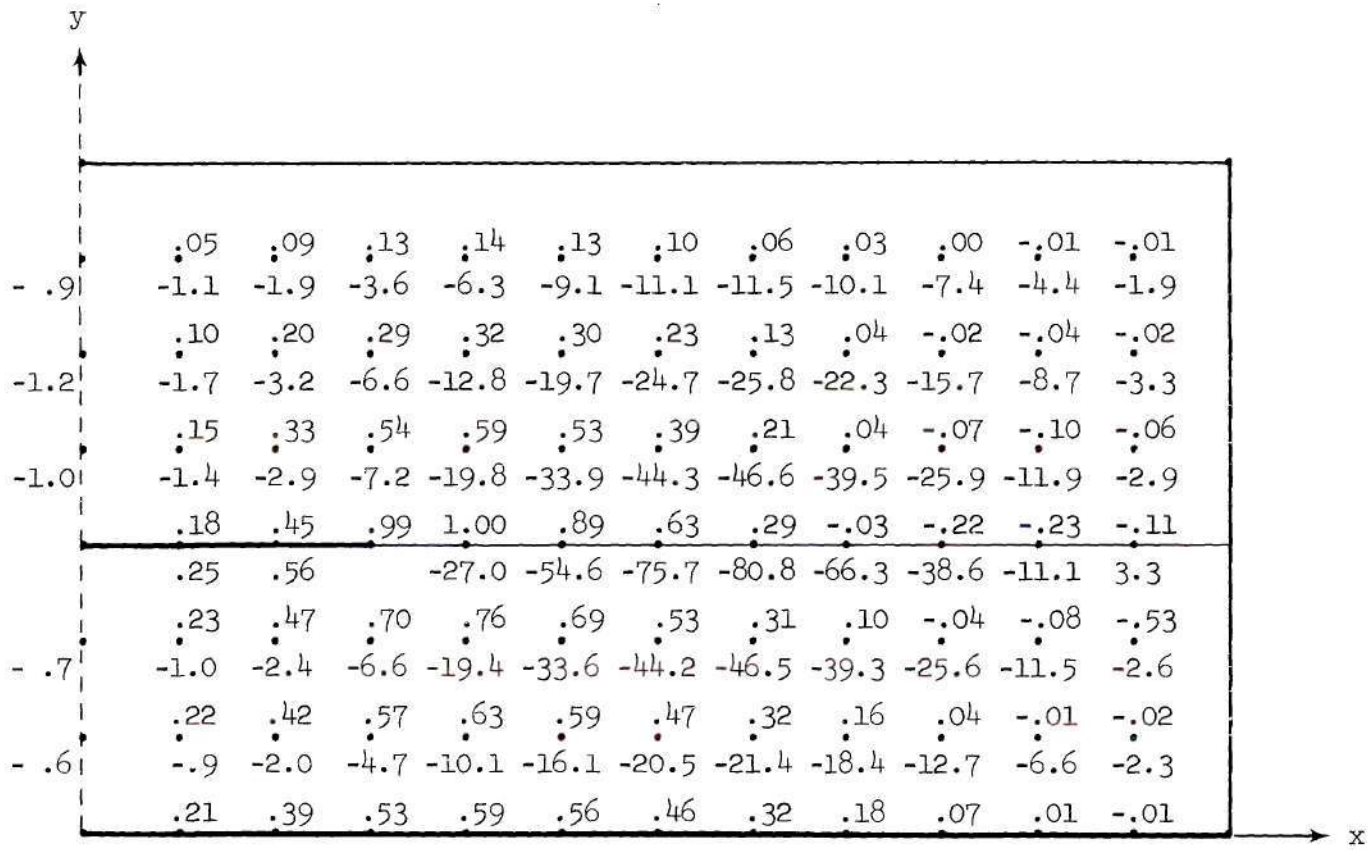

Figure 11. Longitudinal Fields for T = -9, K = 9.5, w/b = 2, and b = .055"

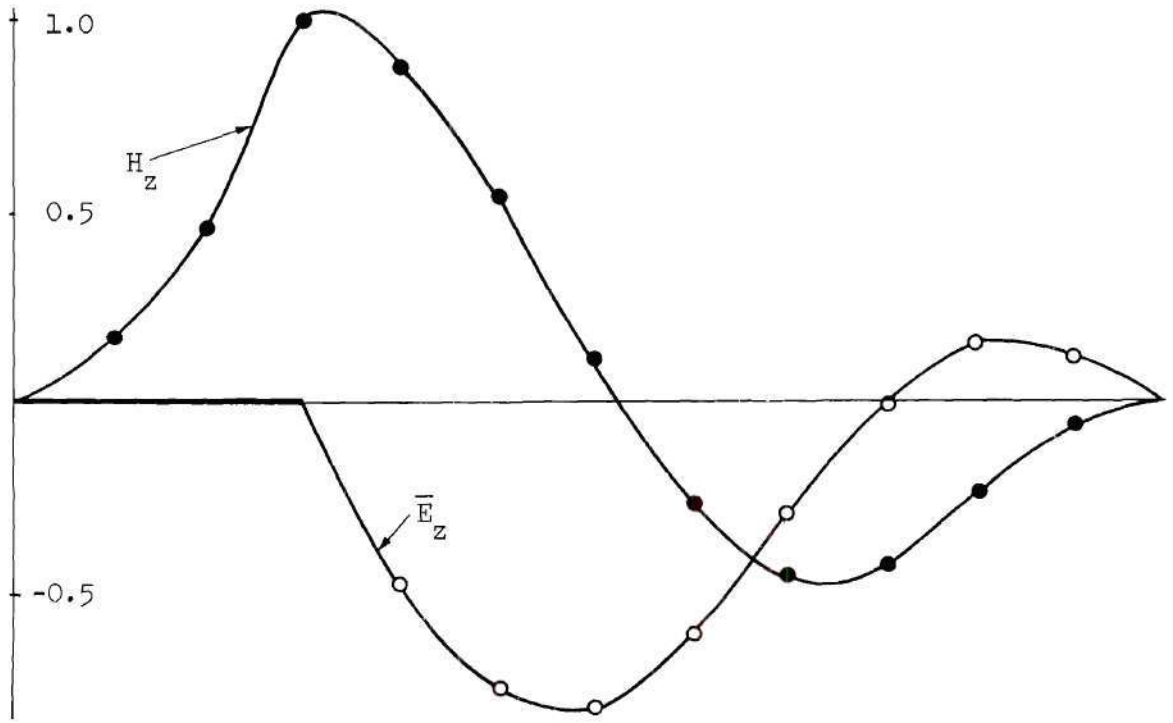

Figure 12. Eigenvector for Lowest Mathematical Mode for T = -10 and f = 7.04 GHz

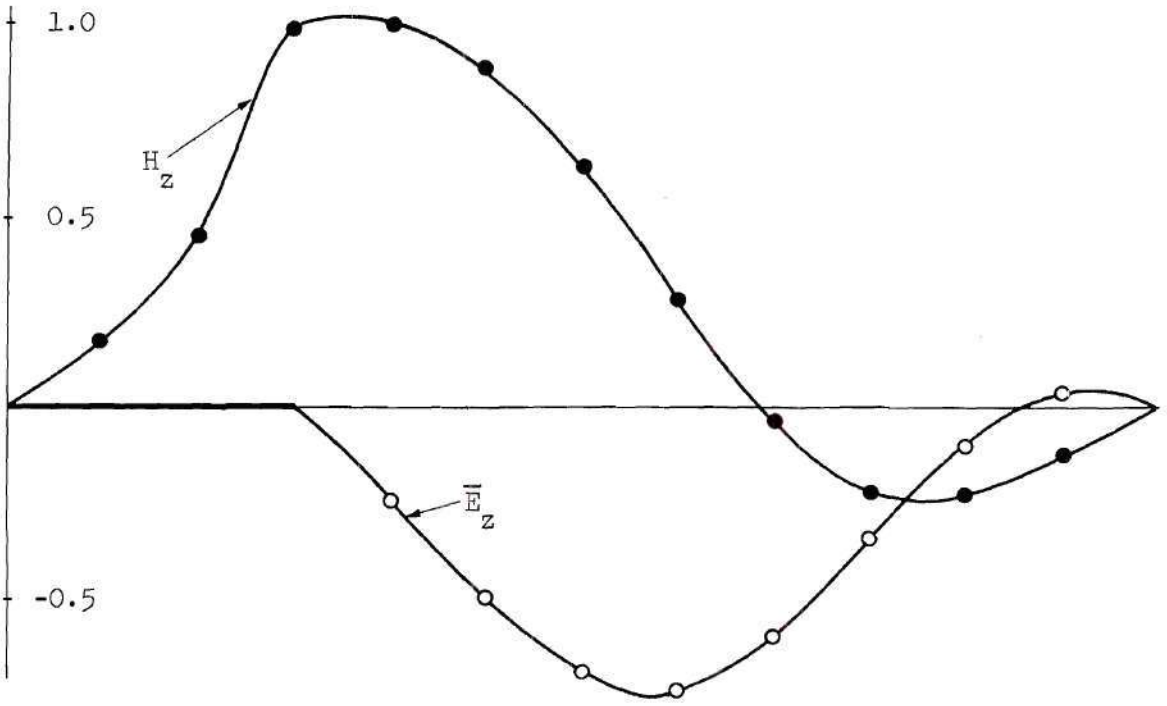

Figure 13. Eigenvector for Second Lowest Mathematical Mode for T = -9 and f = 10.62 GHz

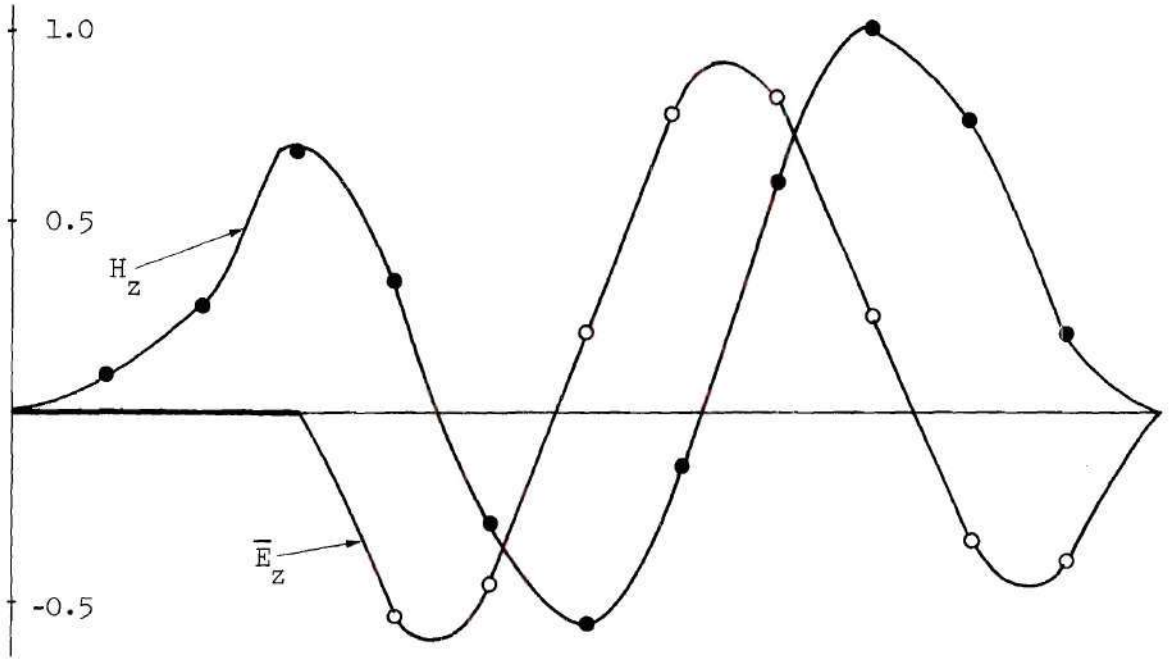

Figure 14. Eigenvector for Third Lowest Mathematical Mode for T = -5 and f = 12.9 GHz

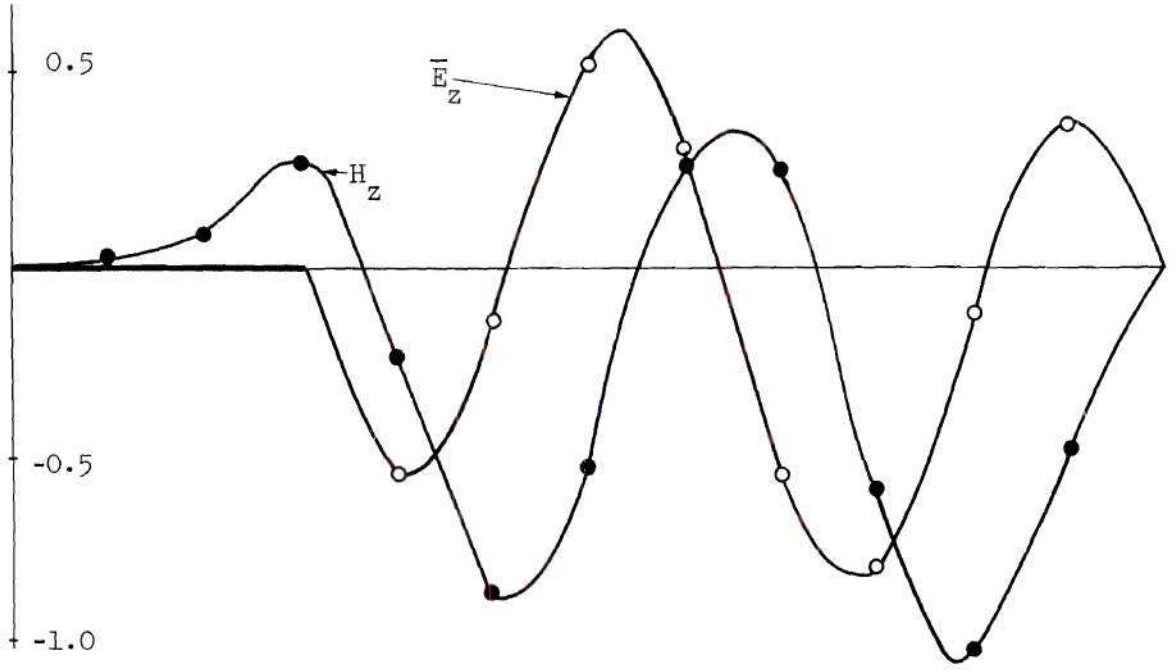

Figure 15. Eigenvector for Fourth Lowest Mathematical Mode for T = -3 and f = 14.49 GHz

calculated from the eigenvalue of column 4 is called the lowest order mathematical mode. That eigenvector corresponding to an eigenvalue in column 3 is the second lowest, and so forth. The region of prime interest was along the air-dielectric interface, since this was the region most accessible for probing the fields. Consequently, the longitudinal fields were plotted as field strength versus position away from the plane of symmetry. For a meaningful comparison, the plots had to correspond to frequencies approximately in the same frequency band. For this reason, the eigenvectors correspond to different values of T. The frequencies on each curve were calculated from Equation (4) for a substrate thickness of .055 inch.

The longitudinal field variations of the lowest order mode, Figure 12, are similar to those of the second lowest mode, Figure 13. The fields of the higher order mathematical modes, Figures 14 and 15, have more undulations than do those of Figures 12 and 13. These field variations are characteristic of higher order modes. Note, however, the pecularity of their shape. Both the longitudinal electric and magnetic fields have increasingly higher amplitude peaks as the distance from the center strip increases. Since these fields result in noncutoff modes having high energy densities away from the center strip, they are not considered to represent physically important modes as intuitively one suspects the dominant mode to be one whose energy density is concentrated nearer the center strip.

In order to help determine which mode (the lowest or second lowest) is the dominant microstrip mode, calculations were made for the microstrip

configuration having a w/b = 1. Similar modes again appeared. At low microwave frequencies, the positive and negative peaks of the lowest order magnetic field solution were nearly equal. At higher microwave frequencies the amplitude of the negative peak of this mode increased and became larger than the positive peak. The early experimental work of Shafer[8] and the experimental work in this dissertation did not confirm the approximately equal positive and negative excursions of H_z. The results of both experimental procedures corresponded more closely with the second lowest solution, i.e. Figure 13. Also, as will be displayed later, the f-β diagram corresponding to the mode of Figure 13 and column 3 of Table 1 is closer to the experimentally determined f-β curve than is the mode of Figure 12 and column 4 of Table 1.

The origin of the lowest mode, the third lowest mode, and so forth is not explicitly known. By the very nature of matrix eigensystems, an n x n system demands that there be n eigenvalues and corresponding eigenvectors. Thus mathematical modes are to be expected in the set of solutions for large matrix eigensystems.

Based on this evidence, the solutions of column 3 of Table 1, i.e. the second lowest mode, are accepted as those solutions corresponding to the dominant microstrip mode.

Frequency-Phase Constant Calculations

In order to determine the frequency corresponding to the eigenvalue and eigenvector obtained for a particular value of T, the substrate thickness has to be specified. The basic node spacing of H = 0.04658 centimeters on the n = 147 microstrip model of Figure 10 corresponded

to a substrate thickness of .055 inch and a k_a^2 given by Equation (3). Each positive eigenvalue of column 3 in Table 1, i.e. the eigenvalues of the dominant mode, was substituted into Equation (3) and the value of k_a^2 for each value of T was calculated. The frequency and phase constant were then calculated from Equations (4) and (5) for each value of T.

Frequency-Phase Constant Diagram. The final result of the frequency and phase constant calculations is best displayed as an f-β diagram in Figure 16. The straight line labeled TEM corresponds to a TEM mode solution that would propagate if the microstrip were fully loaded with a homogeneous dielectric having a relative permittivity of 9.5. The frequency-phase constant curve for the lowest order mathematical mode corresponding to Figure 12 and column 4 of Table 1 was also calculated and is shown in comparison with the calculated curve of the dominant mode. The lowest order mode curve lies just to the right of the dominant mode curve.

Note that $\beta \rightarrow 0$ as $f \rightarrow 0$. This means that the dominant microstrip mode does not have a cutoff and thus propagates at all frequencies. The other mathematical modes investigated also had a theoretical zero frequency cutoff. If these mathematical modes are real physical modes, then they should have been observed experimentally. However, experimental measurements for the f-β diagrams which might have revealed their presence did not yield any evidence to support their existence. This will be discussed further in the experimental results section of Chapter V.

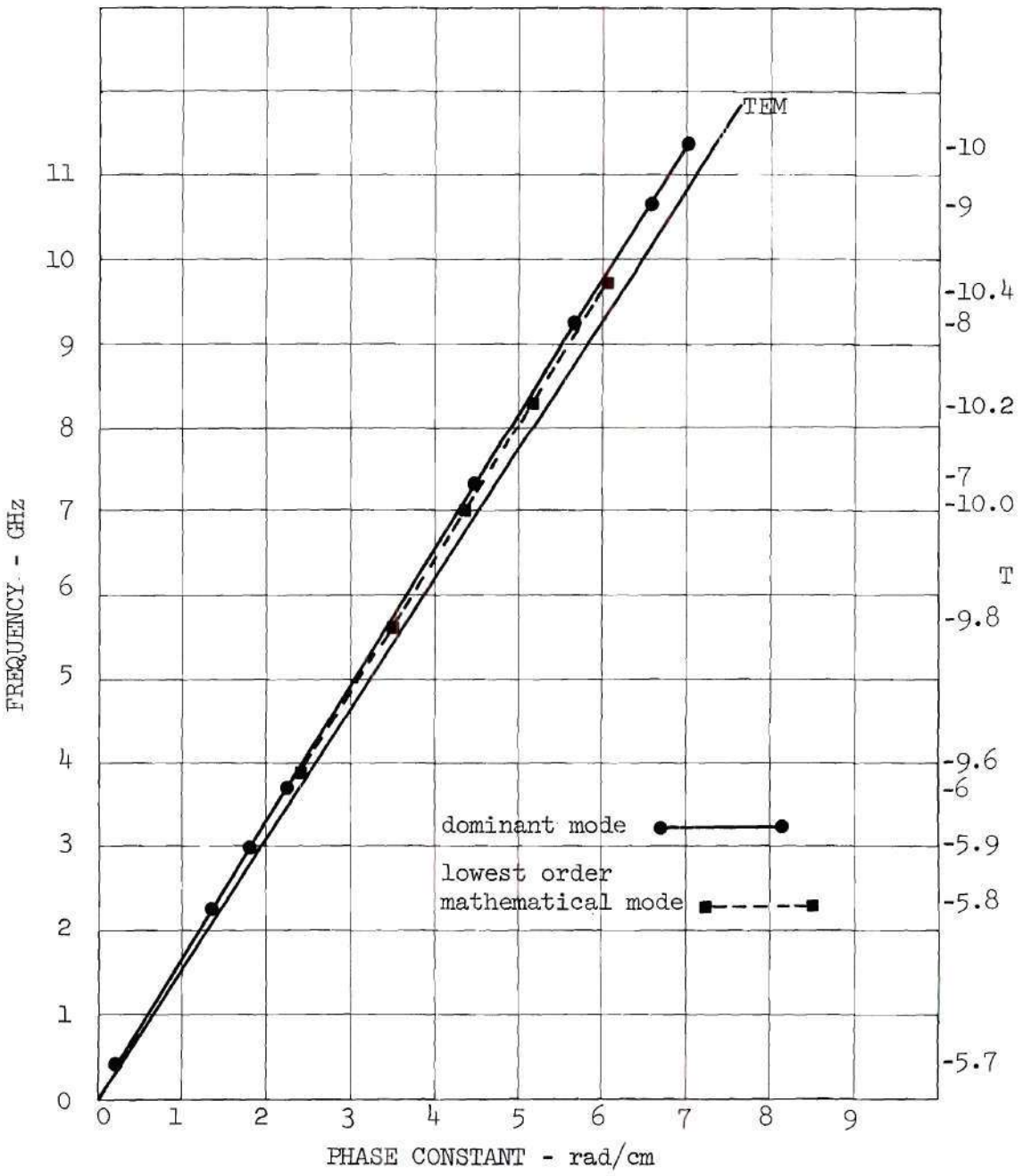

Figure 16. f-β Diagram for the Dominant Mode and the Lowest Order Mathematical Mode for w/b = 2, K = 9.5, and b = .055"

Microwave Dispersion. If microstrip was a nondispersive transmission line, the f-β plot would be a straight line. However, in Figure 16, for the microwave region, the curve turns in towards the TEM plot and converges below 1 GHz. From the diagram it is seen that $\frac{d\omega}{d\beta} < \frac{\omega}{\beta}$ and that microstrip propagation is normally dispersive. Although it had been believed that microstrip was slightly dispersive, the TEM methods of analysis failed to provide any evidence to that fact. The numerical analysis method employed here does display the dispersiveness.

Transverse Field Distribution

The transverse fields were calculated from the longitudinal fields of the .055 inch alumina substrate with w/b = 2. The transverse components of the electric and magnetic fields were then combined to form a transverse field vector in order to provide a more complete picture of the microstrip mode.

Transverse Magnetic Fields. The transverse magnetic field vector at each node for the .055 inch alumina suhstrate with a .110 inch center strip at 10.63 GHz is shown in Figure 17. Note that, in the vicinity of the center strip, the transverse magnetic field loops around that conductor. This behavior is as expected since the microstrip mode is presumed to be somewhat similar to a TEM mode for which the magnetic field is entirely transverse and loops around the center conductor.

Transverse Electric Fields. The transverse electric field distribution for the same configuration is drawn in vector form at each node in Figure 18. Here again, note the similarity of this transverse electric field to that of a TEM mode which would exist in the vicinity of

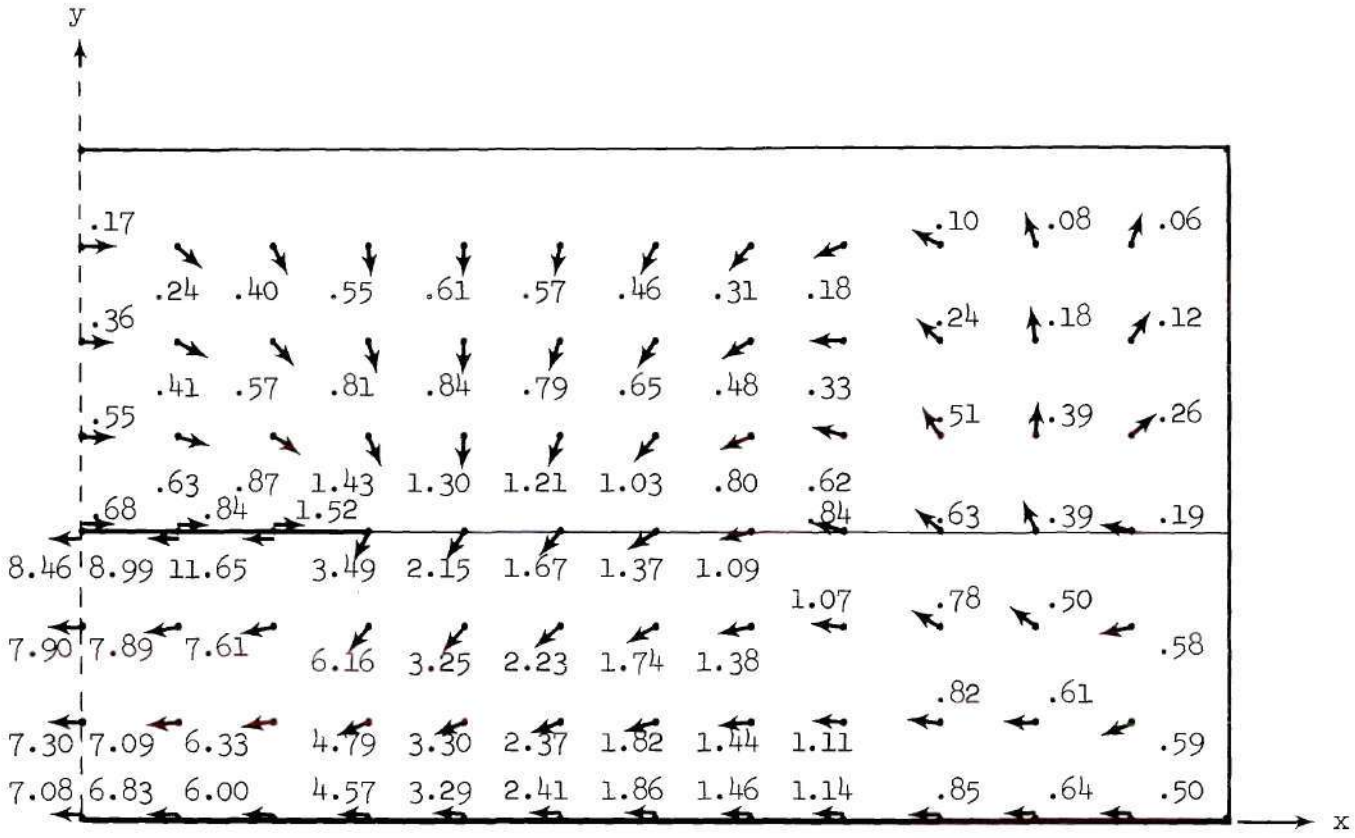

Figure 17. Transverse Magnetic Field Distribution of the Dominant Microstrip Mode on the .055" Alumina Substrate at 10.63 GHz

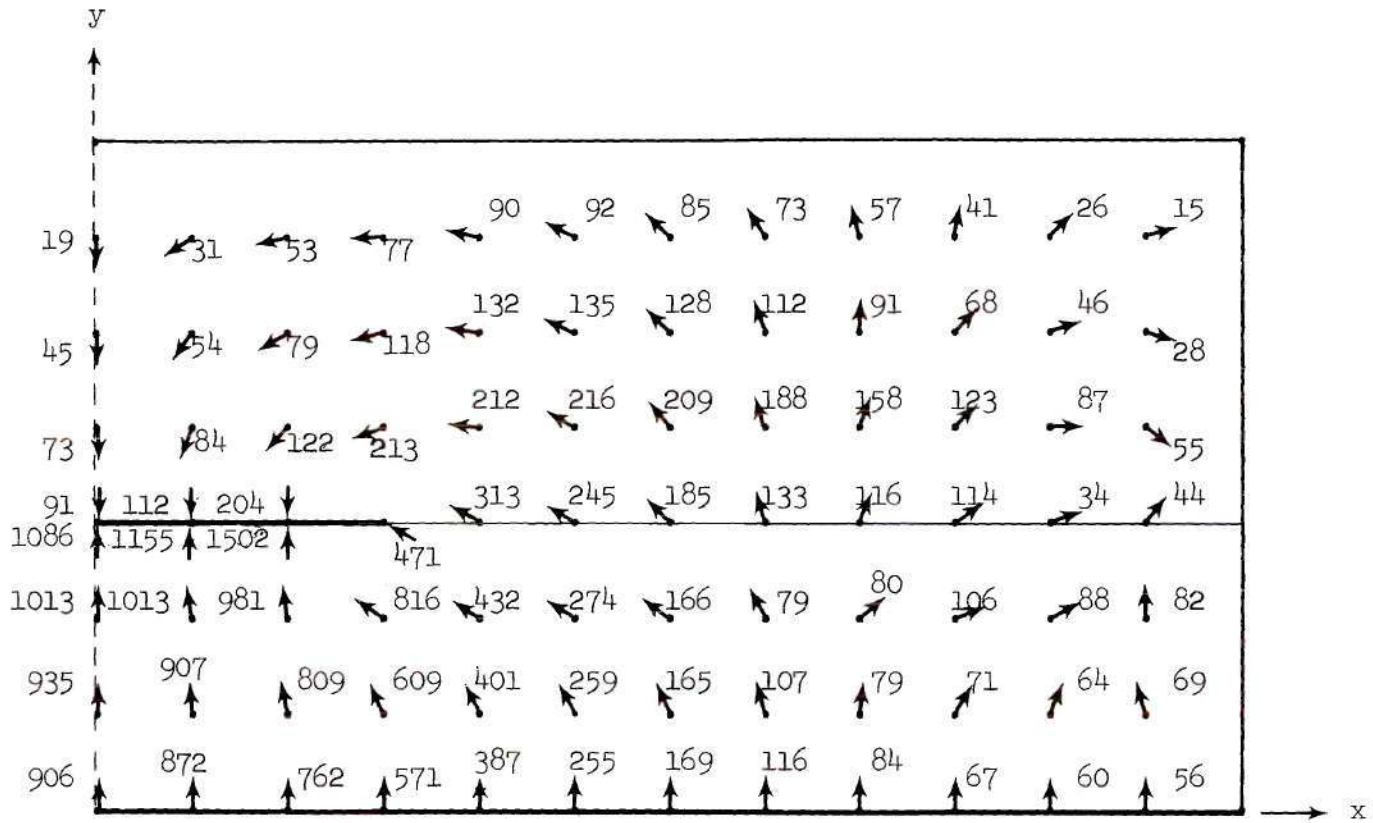

Figure 18. Transverse Electric Field Distribution of the Dominant Microstrip Mode on the .055" Alumina Substrate at 10.63 GHz

the center strip of a fully loaded line. For both the TEM and the hybrid coupled mode, the total energy concentration is high in the region under the center strip.

Effect of Frequency Change. It was observed in the f-β plot of Figure 16 that the microstrip mode curve approached the TEM mode straight line at low microwave frequencies. This behavior suggests the possibility of the longitudinal electric and magnetic fields becoming smaller in comparison with the transverse fields as the frequency was reduced, thus approaching a quasi-TEM mode. To check this, fields at a frequency of 4.97 GHz were calculated and compared with those at 10.63 GHz. The resulting longitudinal magnetic and scaled electric fields along the air-dielectric interface are plotted in Figure 19. The fields, normalized to unity, at the two frequencies were similar. The transverse fields are displayed in vector form in Figure 20.

The transverse magnetic fields at 10.63 GHz were smaller than those at 4.97 GHz. Each complete field distribution was normalized to the maximum of the eigenvector which in these cases was the maximum longitudinal magnetic component. In other words, for approximately equal amplitude transverse field distributions, the relative amplitude of the longitudinal magnetic field at 4.97 GHz was smaller than that at 10.63 GHz. Thus, as the frequency is lowered and the guide wavelength becomes much larger than the substrate thickness, the longitudinal fields decrease in amplitude and the microstrip mode approaches a TEM mode.

Transverse Field of a Higher Order Mathematical Mode. As a matter of interest, the transverse field distributions were calculated for the

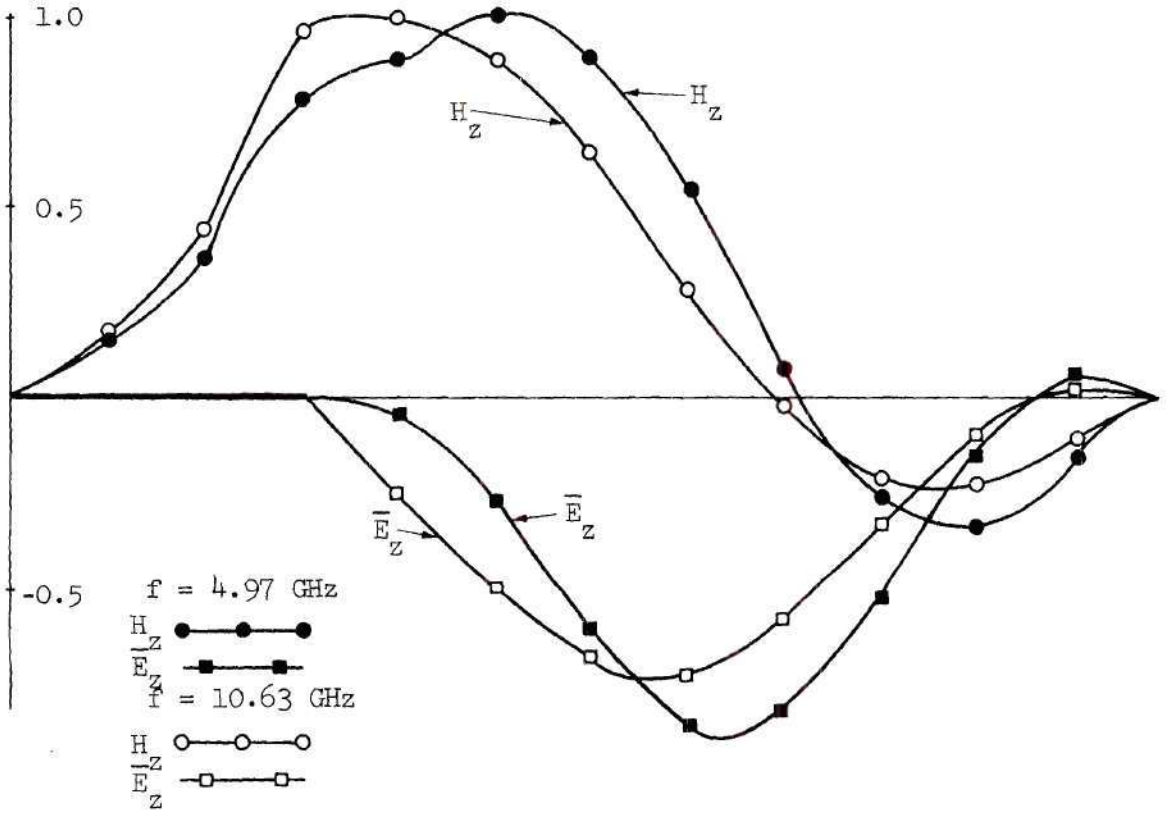

Figure 19. Longitudinal Fields of the Dominant Microstrip Mode at 4.97 GHz and 10.63 GHz

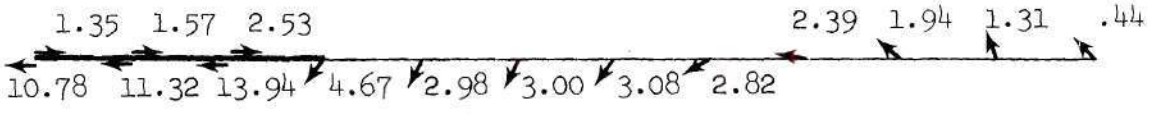

(a) f = 4.97 GHz

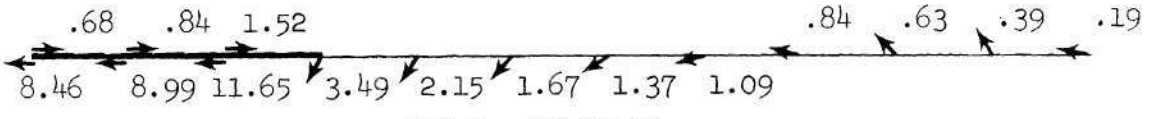

(b) f = 10.63 GHz

Figure 20. Transverse Magnetic Fields of the Dominant Microstrip Mode at 4.97 GHz and 10.63 GHz

longitudinal fields of Figure 14. The transverse magnetic field vectors at each node are shown in Figure 21 and the transverse electric field vectors at each node are shown in Figure 22. Note the relatively high field intensities which are concentrated away from the center strip. No experimental evidence as yet supports the existence of this mathematical mode.

Total Magnetic Field of the Dominant Mode

A typical magnetic field mode pattern in the neighborhood of the center strip is sketched in Figure 23. This mode pattern was based on calculations for the .055" alumina substrate with a w/b = 2 whose longitudinal magnetic fields and transverse magnetic fields (which are in time quadrature as required by Maxwell's equations) are given in Figures 11 and 17, respectively.

This mode has a distinctive feature not found in a TEM mode. The field distribution of a TEM mode lies entirely transverse to the direction of propagation. For this hybrid coupled mode, at an instant of time and for a specific location on the line the fields are purely transverse. However, at a point $\lambda_g/8$ down the line there are both transverse and longitudinal fields and at a point $\lambda_g/4$ down the line the fields are purely longitudinal.

A distinguishing characteristic causes the hybrid coupled mode to sometimes be referred to as a saddle mode since the magnetic field looks like an inverted saddle as it loops back into the substrate on either side of the center strip and closes on itself under the conductor.

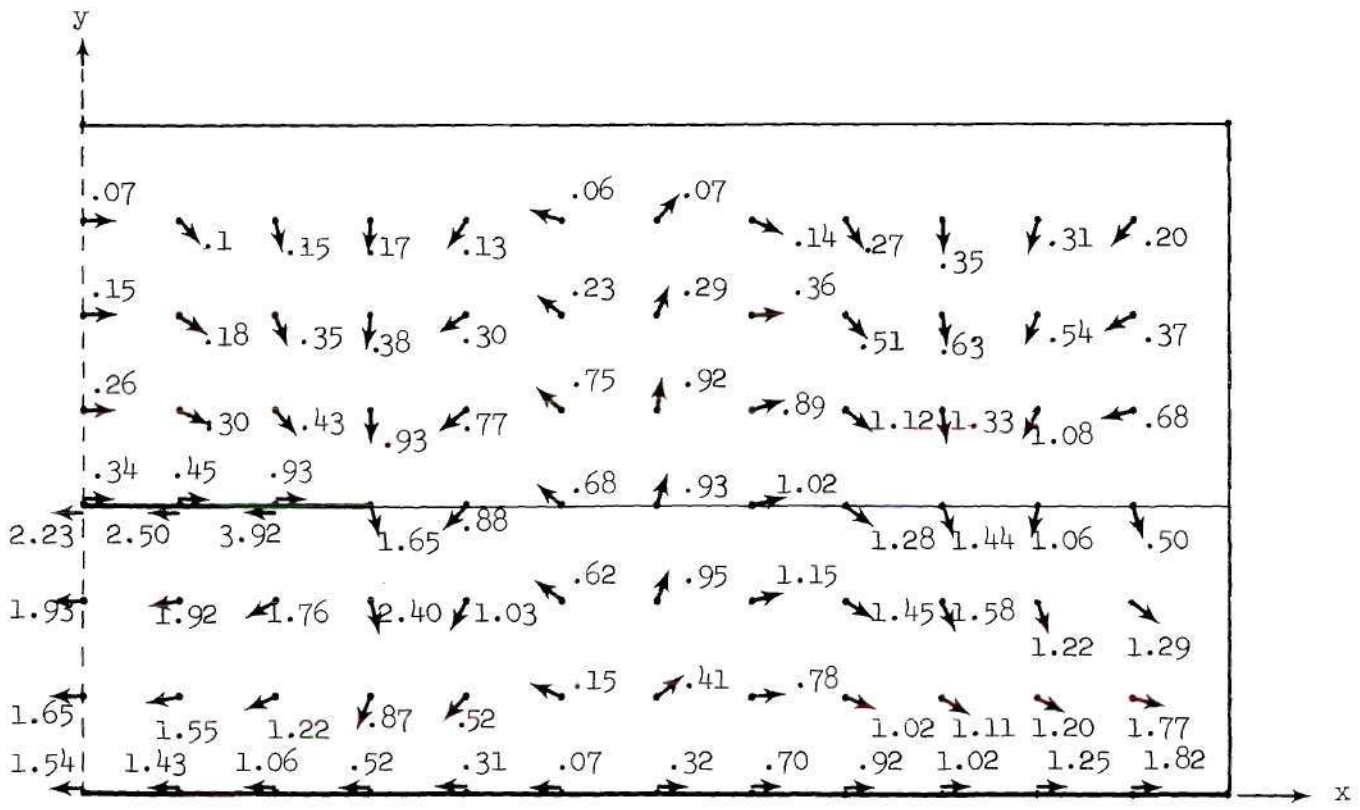

Figure 21. Transverse Magnetic Field Distribution of a Higher Order Mathematical Mode for the .055" Alumina Substrate at 12.91 GHz

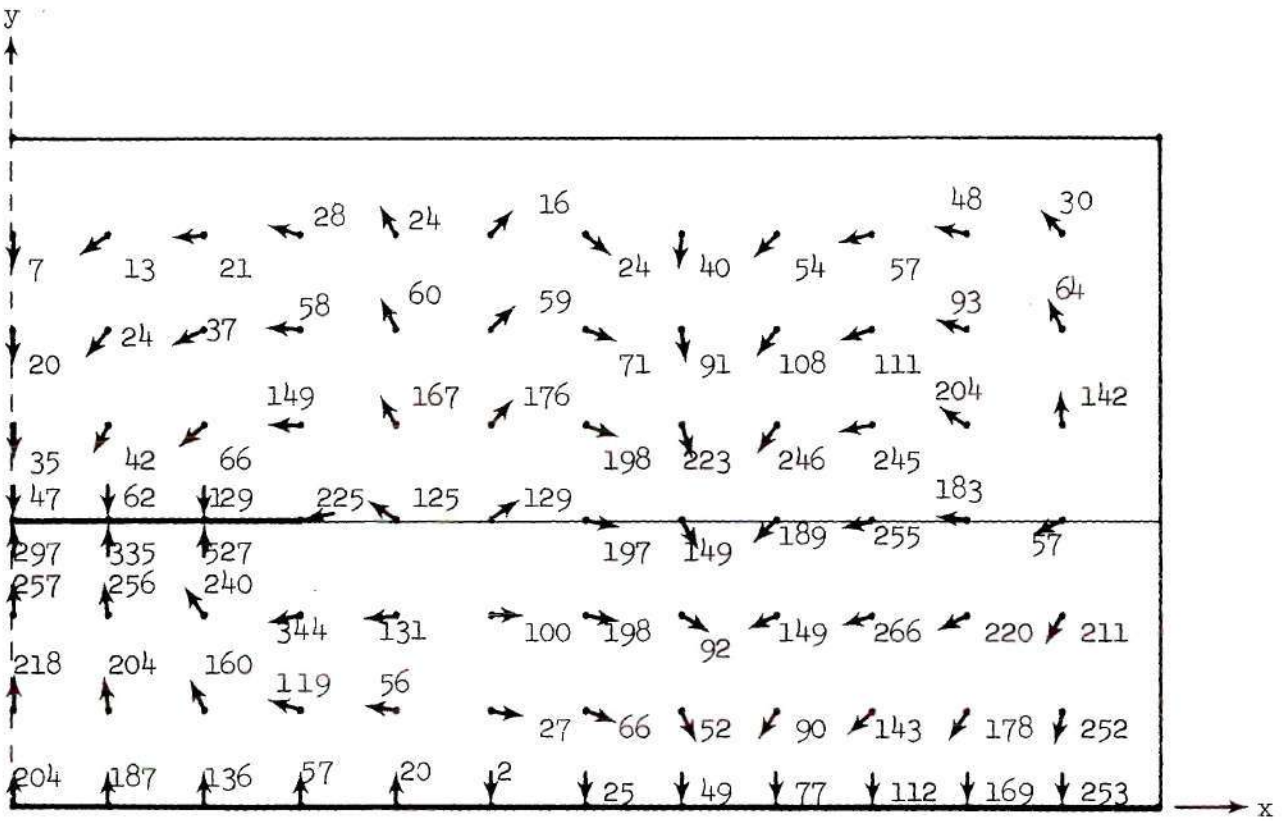

Figure 22. Transverse Electric Field Distribution of a Higher Order Mathematical Mode for the .055" Alumina Substrate at 12.91 GHz

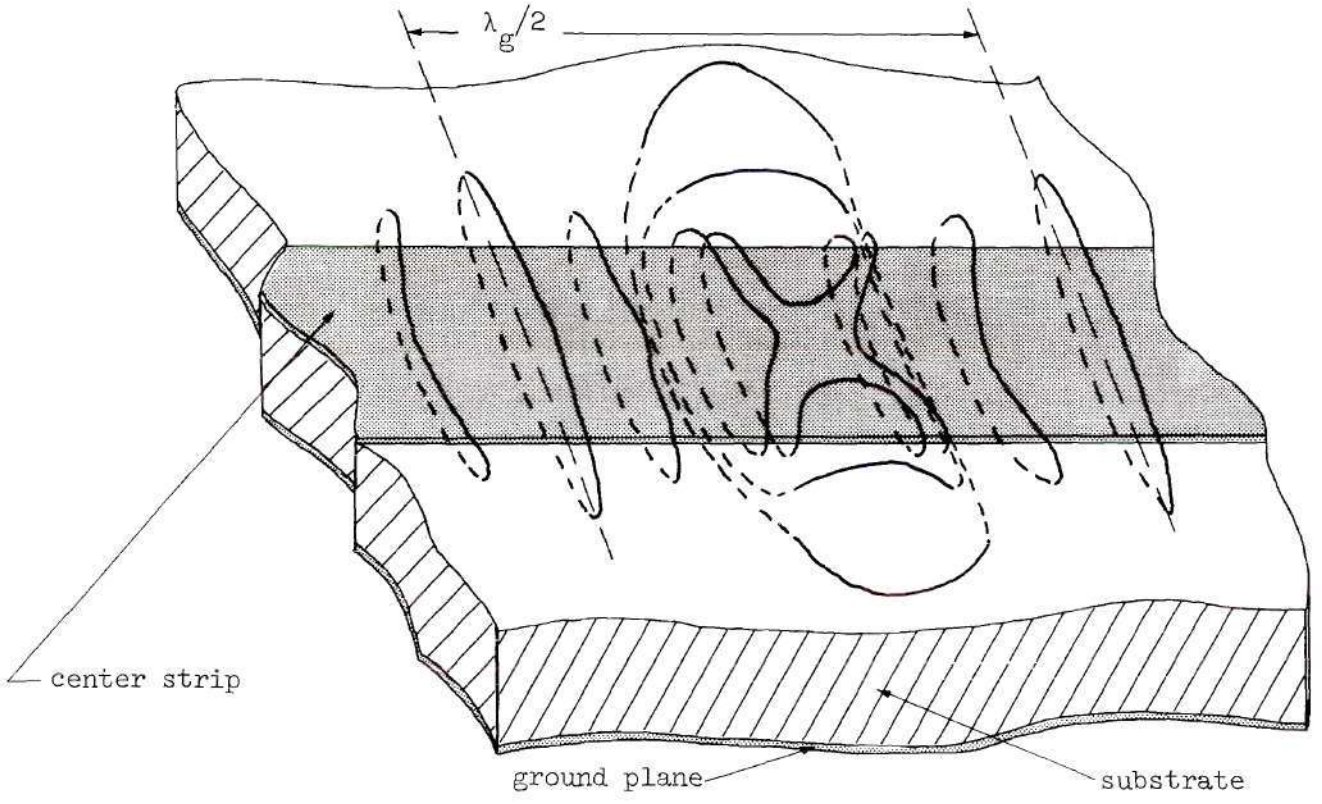

Figure 23. Magnetic Field Distribution of the Dominant Microstrip Mode in the Vicinity of the Center Strip

Other Microstrip Calculations

Frequency-Phase Constant Calculations

Frequency-phase constant calculations were made for four other microstrip lines with the parameters listed in Table 2.

Table 2. Parameters of Other Microstrip Lines

Dielectric Constant	Substrate Thickness	w/b
9.5	.025"	1
9.5	.025"	2
9.5	.055"	1
16	.055"	2

The f-β curves for these cases are plotted in Figures 24 through 27. The shape of each is similar to the dispersion curve of the dominant mode in Figure 16, in that each exhibits dispersion in the microwave band and each approaches the TEM straight line at low microwave frequencies. Since the f-β curve retains its shape relative to the TEM curve, these results imply that the microstrip mode of propagation is not greatly perturbed by changes in physical dimensions and dielectric constant.

Field Calculations

The longitudinal field distributions for the four configurations of Table 2 are shown in Figures 28 through 31. The fields are similar to the fields of Figure 11, thus they are only plotted along the inter-

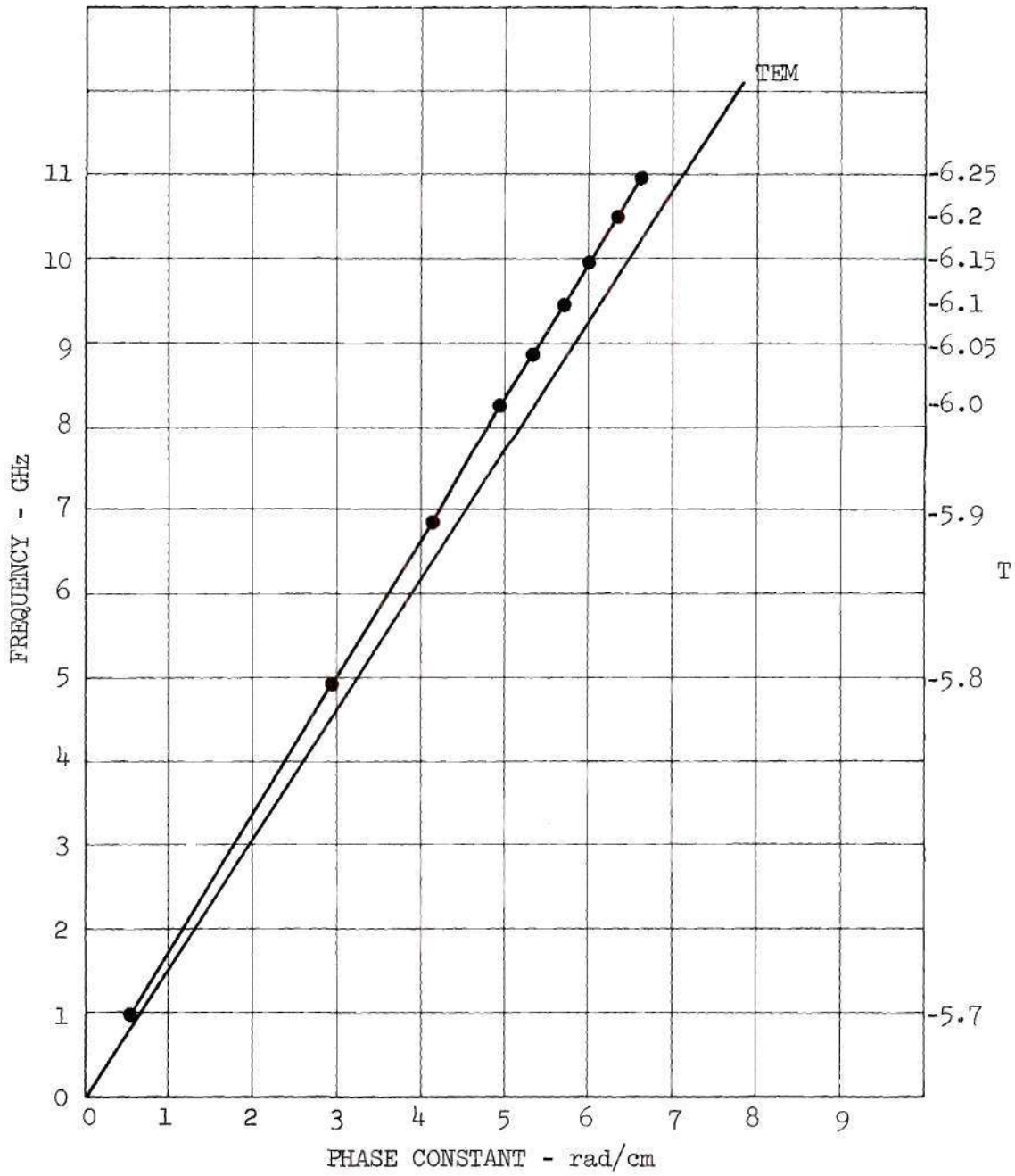

Figure 24. f-β Diagram for the Dominant Microstrip Mode on a .025" Alumina Substrate with w/b = 2

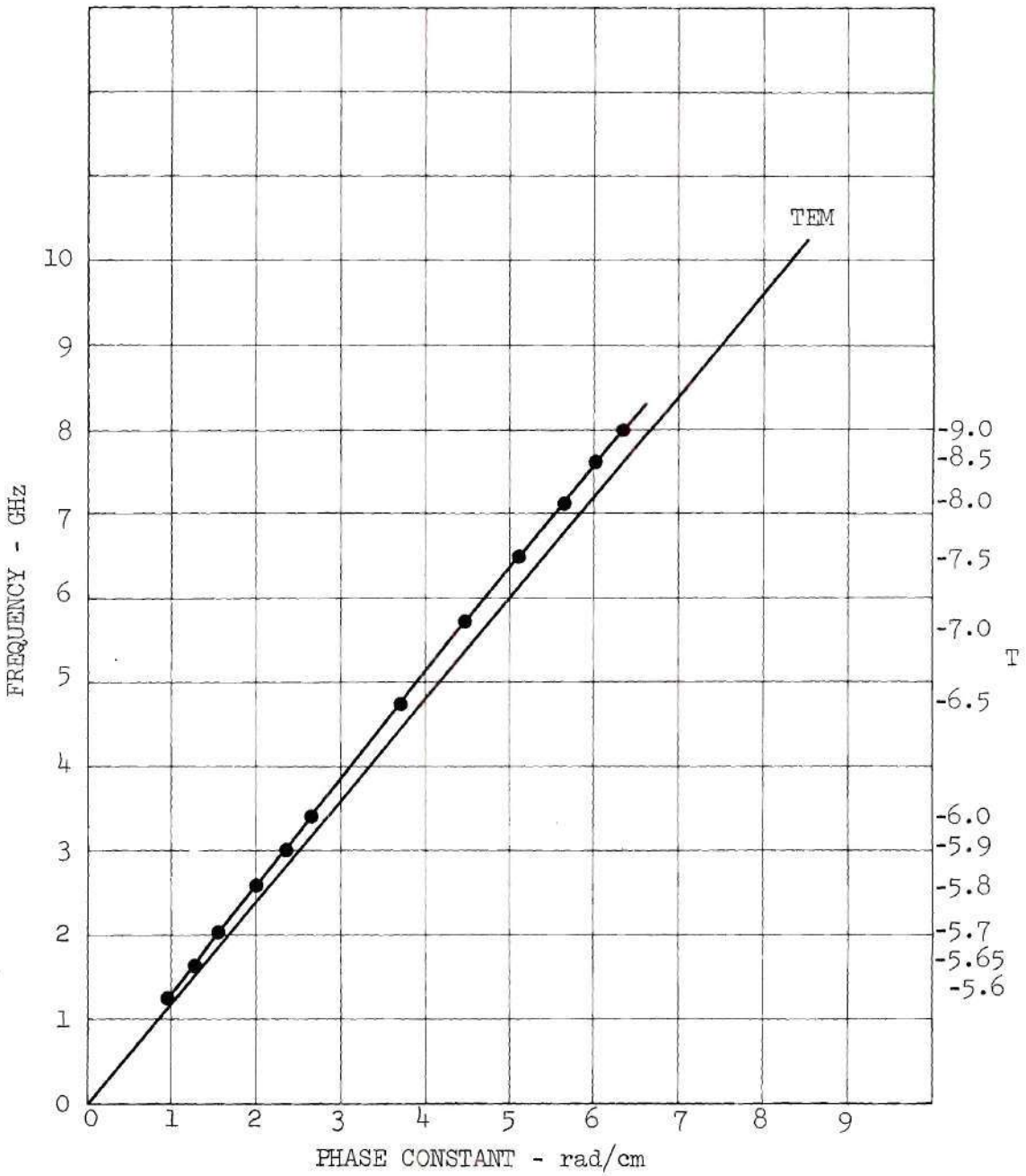

Figure 25. f-β Diagram for the Dominant Microstrip Mode on a .055" D-16 Substrate with w/b = 2

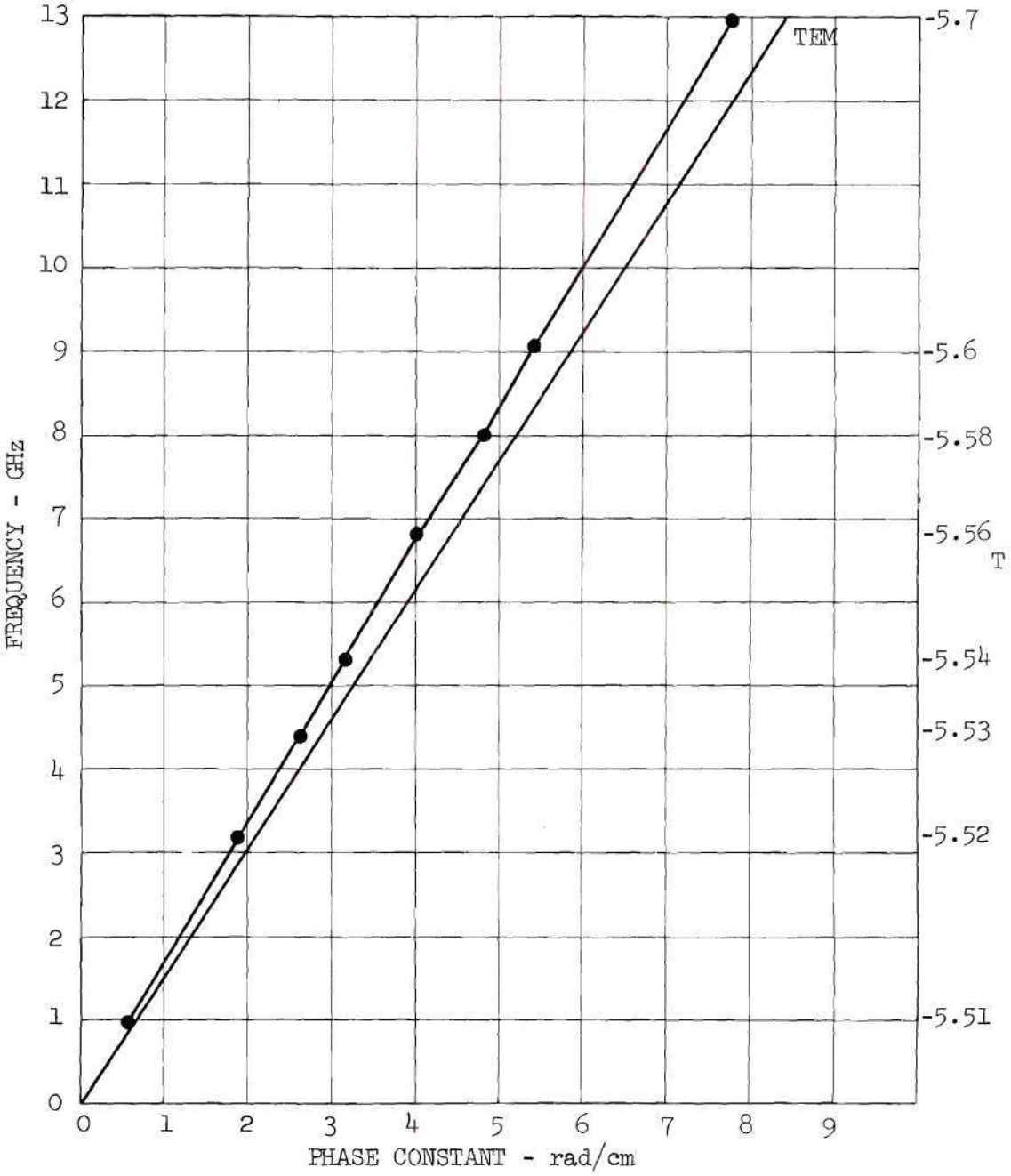

Figure 26. f-β Diagram for the Dominant Microstrip Mode on a .025" Alumina Substrate with w/b = 1

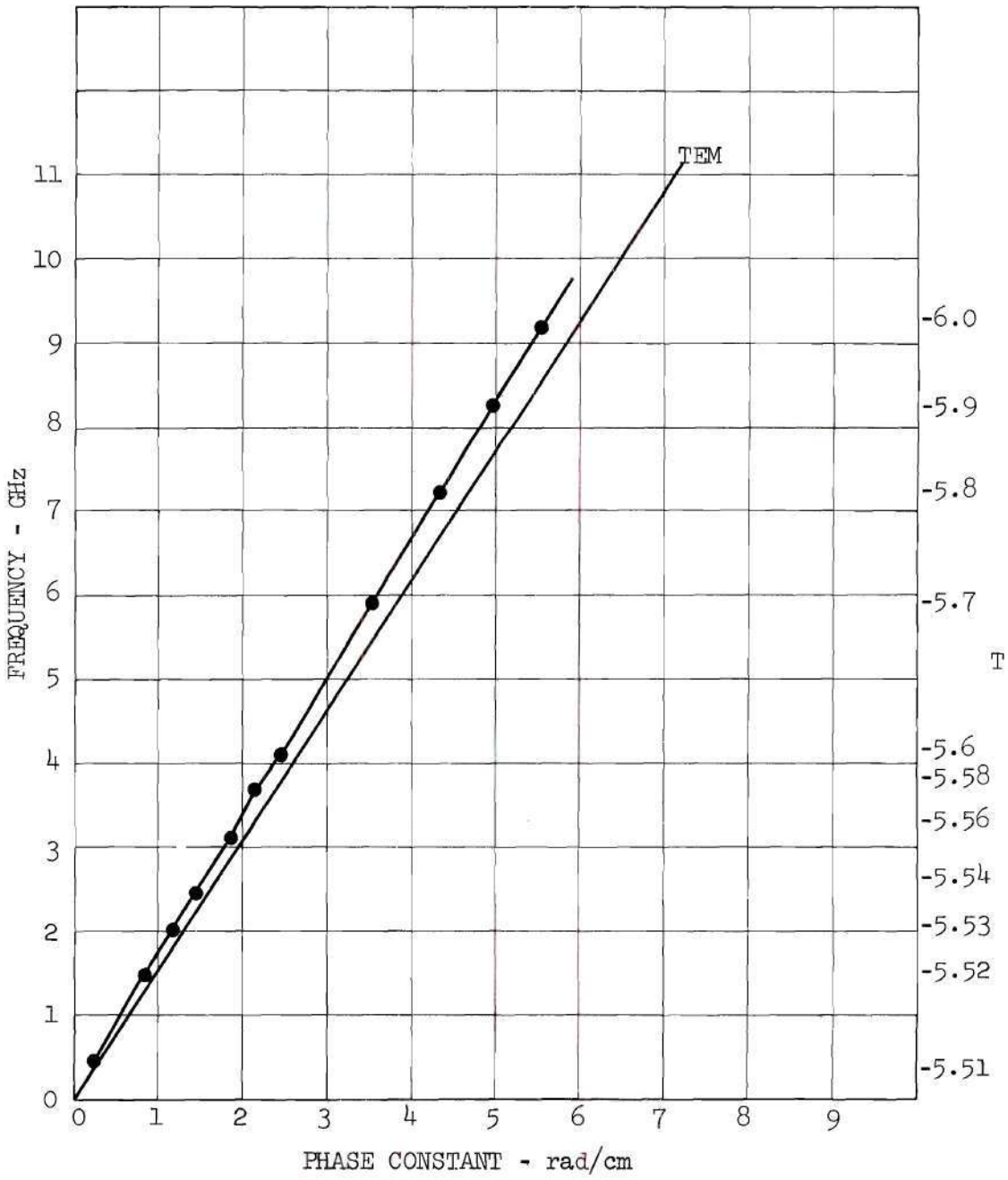

Figure 27. f-β Diagram for the Dominant Microstrip Mode on a .055" Alumina Substrate with w/b = 1

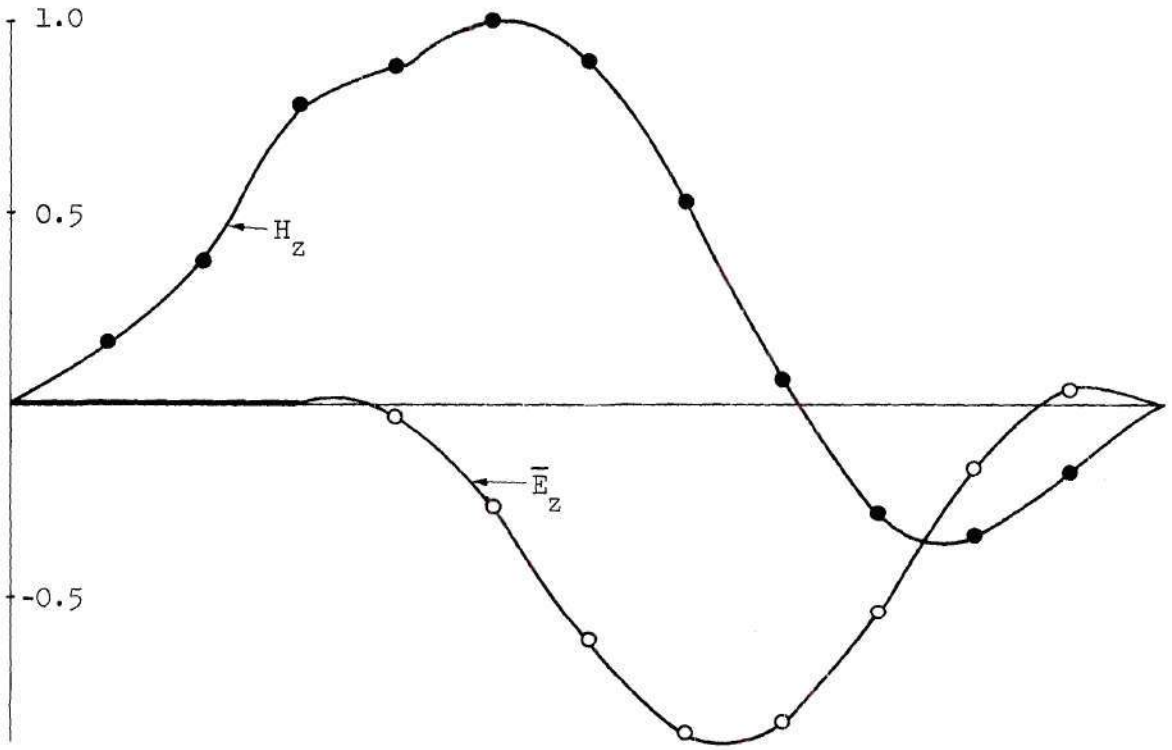

Figure 28. Longitudinal Fields for the Dominant Microstrip Mode on a .025" Alumina Substrate with w/b = 2

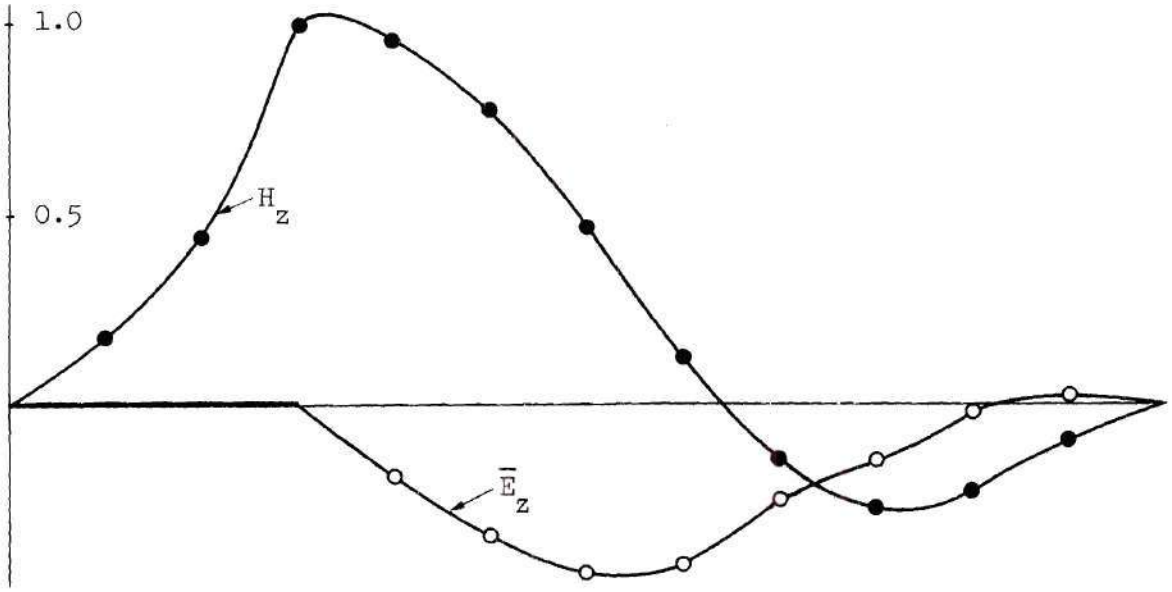

Figure 29. Longitudinal Fields for the Dominant Microstrip Mode on a .055" D-16 Substrate with w/b = 2

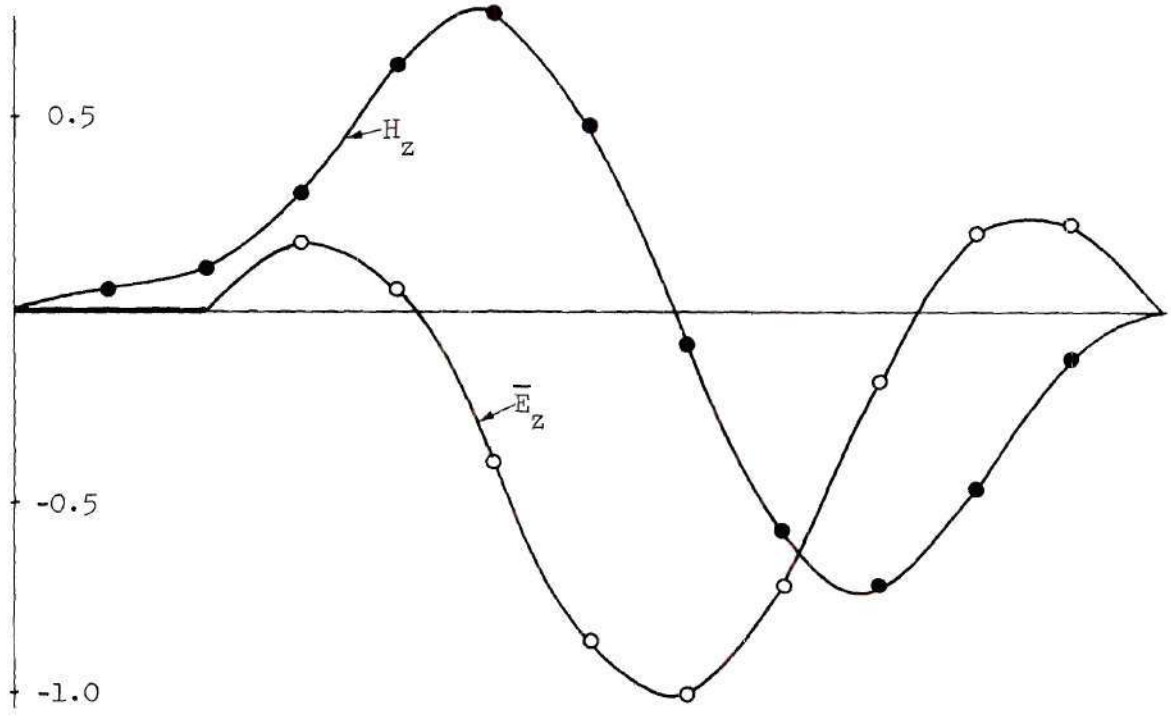

Figure 30. Longitudinal Fields for the Dominant Microstrip Mode on a .025" Alumina Substrate with w/b = 1

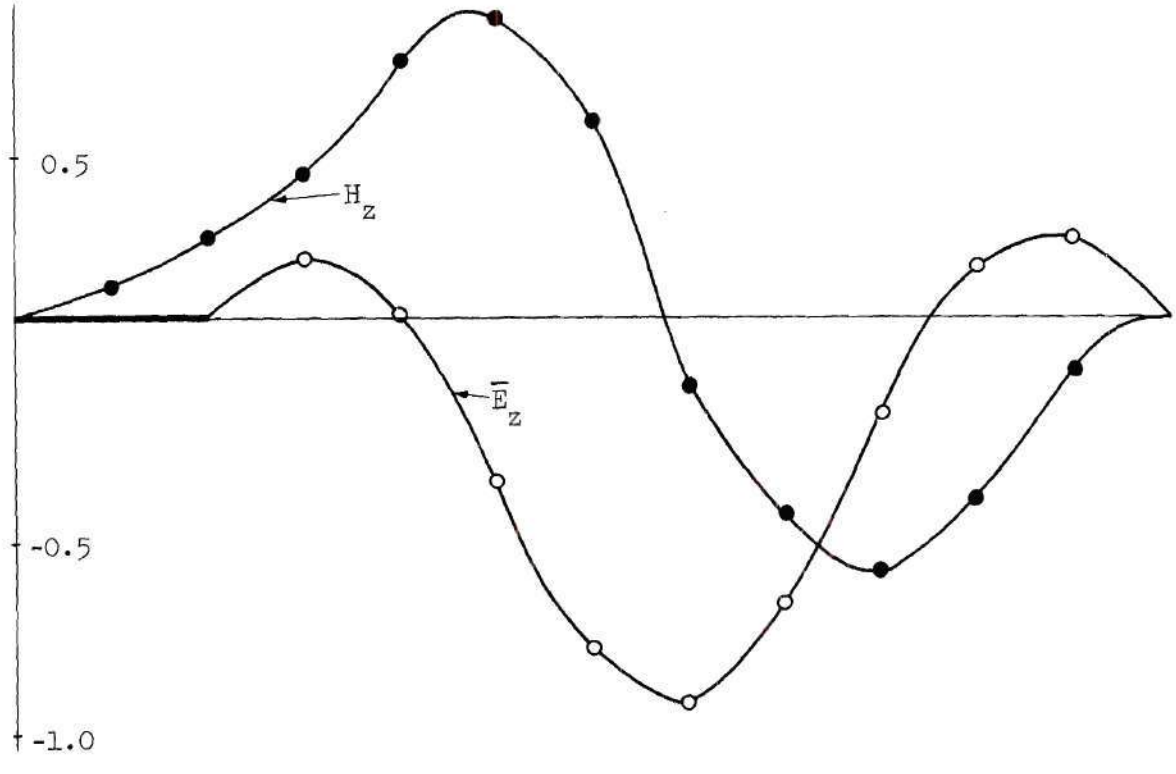

Figure 31. Longitudinal Fields for the Dominant Microstrip Mode on a .055" Alumina Substrate with w/b = 1

face. The dominant mode has the same basic saddle mode shape as depicted in Figure 23 irrespective of dielectric constant or physical dimensions.

It might be noted in passing that, in Figures 28 and 29, the element of maximum modulus is a magnetic field component whereas in Figures 30 and 31 it is a scaled electric field component. This is purely a result of the choice of the scale parameter χ (see Equation (6)) which was arbitrarily set equal to ten for these four calculations.

CHAPTER IV

EXPERIMENTAL PROCEDURES

The solutions to the eigensystem problem set up in Chapter II and solved in Chapter III led to theoretical descriptions of microstrip frequency-phase constant diagrams and electromagnetic field distributions. Experiments were designed to verify the f-β diagram and the relative magnitudes of the RF magnetic fields of the microstrip hybrid coupled mode. The experimental procedures are described below, the experimental errors are discussed at the end of this chapter, and the results of the experiments will be presented in Chapter V.

Loosely Coupled Transmission Resonance Experiment

Theory of Transmission Resonance

The phase constants for microwave frequencies between 2 to 12 GHz were determined by loosely coupling RF energy through a microstrip line of known length which had been short circuited at both ends. The shorted line was resonant at frequencies for which the line length, ℓ, was an integral number of guide half-wavelengths $\lambda_g/2$. At these resonant frequencies maximum energy was coupled through the shorted microstrip section. Stated mathematically, these resonances occurred at frequencies for which

$$\ell = \frac{n\lambda_g}{2} = \frac{n\pi}{\beta}, \quad n = 1, 2, 3, 4, \ldots\ldots \tag{1}$$

The line was sufficiently long so that several resonances occurred in the frequency range of interest.

For each resonance, the value of n was determined in the following manner:

(1) the frequency at which a transmission resonance occurred was noted,

(2) the value of β corresponding to that particular frequency was taken off the theoretically obtained f-β diagram, and

(3) equation (1) was solved for a noninteger value of n, and the integer nearest to n was chosen.

As an experimental check on the calculated value of n, a metal probe mounted on a moving carriage and positioned just over the center strip was moved over the entire length of the microstrip line. The metal probe perturbed the standing wave on the line least when in the vicinity of an electric field minimum and most when in the vicinity of an electric field maximum. The field perturbations were evidenced by a shift in the resonant frequency. The length of the line in guide half-wavelengths was found and n determined by counting the number of frequency shifts encountered as the probe was moved from one end of the shorted line to the other.

Then β was calculated from

$$\beta = \frac{2\pi}{\lambda_g} = \frac{n\pi}{\ell} \qquad (2)$$

The dispersion curve was then plotted from the f-β combinations obtained.

Transmission Resonance Experimental Setup

Microstrip Lines. Six typical microstrip lines were fabricated on two standard substrate materials, alumina and D-16 (a magnesium titanate). Alumina, with a relative dielectric constant of approximately 9.5, was available in two substrate thicknesses, .025" and .055". D-16, with a relative dielectric constant of approximately 16, was available in a .055" thickness. The metalization of the substrate was accomplished by vacuum depositing thin films of first chromium and then gold on the substrate. This was followed by electroplating four to six microns of silver to the thin film of gold. The etching was accomplished by standard photoresist techniques. Table 3 lists the substrate thicknesses, b, the relative dielectric constants, the center strip widths, w, the w/b ratios, and the characteristic impedances, Z_o, of the six microstrip lines which were used.

Table 3. Parameters of the Experimental Microstrip Lines

Substrate Thickness b	Relative Dielectric Constant	Center Strip Width w	w/b Ratio	Characteristic Impedance Z_o
.055"	9.5	.110"	2	33 Ω
		.055"	1	50 Ω
.025"	9.5	.050"	2	33 Ω
		.025"	1	50 Ω
.055"	16.0	.110"	2	25 Ω
		.033"	0.6	50 Ω

Two lines were etched on each substrate. The spacing was such that there

was effectively no coupling between the lines. The length of each substrate and thus each microstrip line was three inches.

Test Piece. A drawing of the test piece for the loosely coupled transmission experiment is shown in Figure 32. The coupling loop was formed by soldering a piece of wire from the center conductor of the OSM miniature connector to the bulkhead of the mounting plate. The loops were positioned close to but not touching the center strip. The radius of curvature of the loop was about 1/16 inch. The microstrip was shorted at both ends by spot welding .050" wide strips of gold ribbon to the center conductor and the ground plane. The mounting plates were affixed to the brass base and the substrate was set into place. The microstrip's ground plane had to make good contact with the brass base and mounting plates so that the effective short circuit would be at the ends of the center strip.

Equipment. A photograph of the equipment used in this set of measurements and in the spin resonance absorption experiment (discussed later) is shown in Figure 33. Two of the microwave sweep generators and the oscilloscope used are on the left side of the picture. A block diagram of the setup used to perform the transmission resonance experiment is shown in Figure 34. Three sweep generators were necessary in order to cover the frequency range between 2 and 12 GHz. The sweep voltage of the microwave sweep generators was coupled to the horizontal amplifier of the oscilloscope so that a visual display of the transmission resonances versus frequency was obtained as the frequency was swept. At a frequency for which resonance transmission occurred, maximum energy was coupled

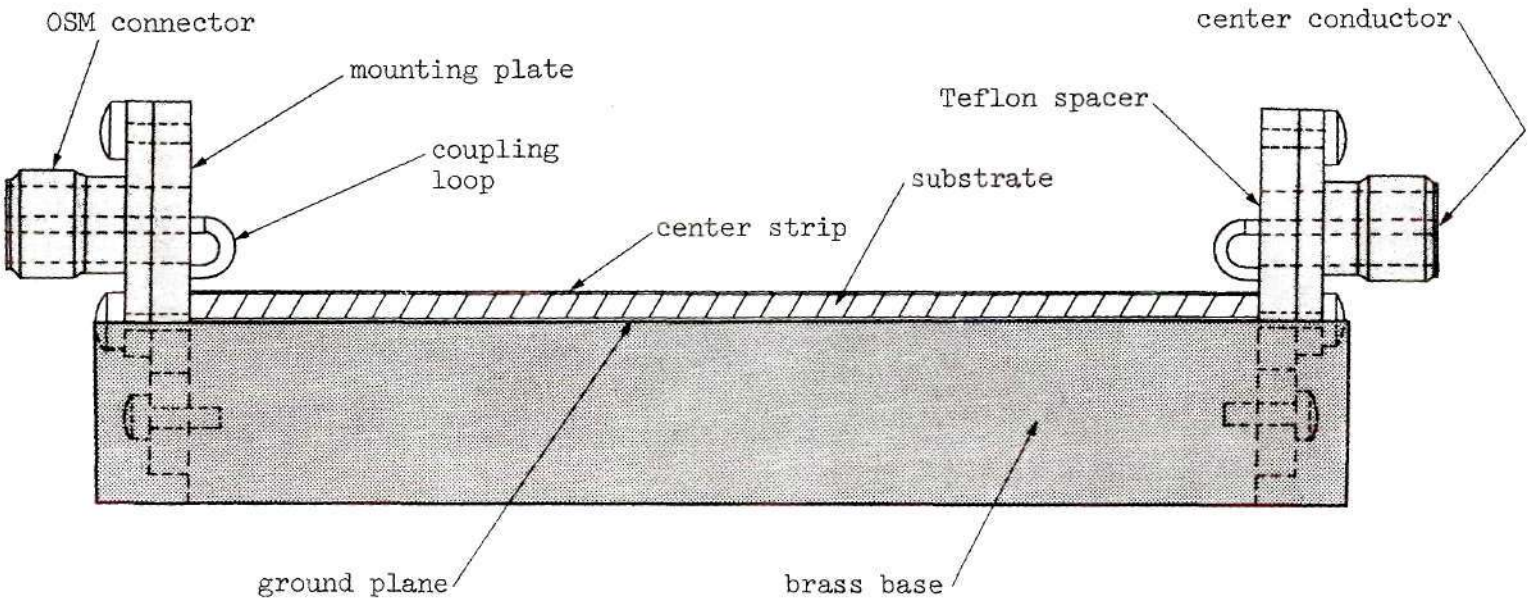

Figure 32. Transmission Resonance Test Piece

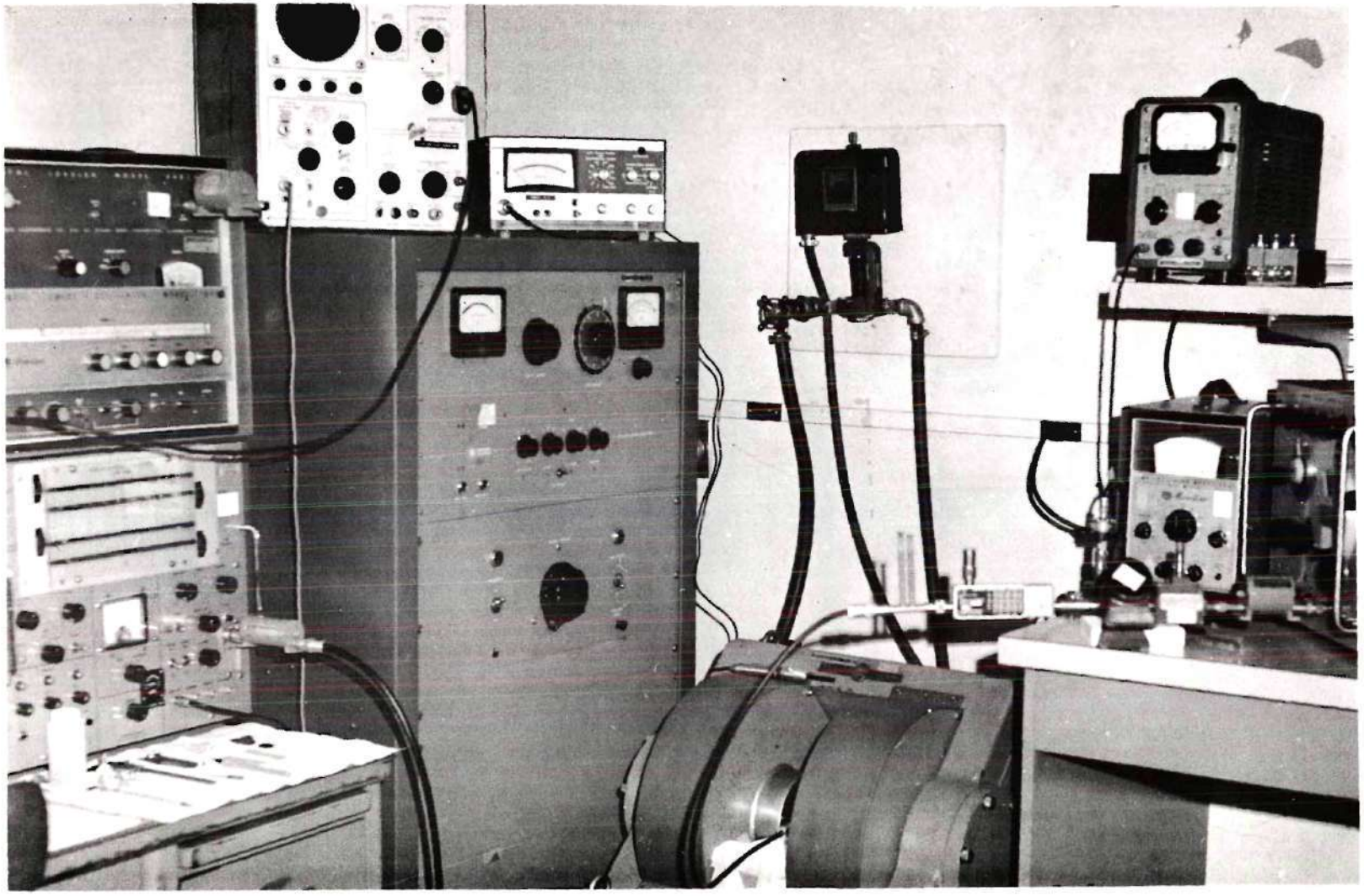

Figure 33. A Photograph of the Equipment Used in the Experimental Research

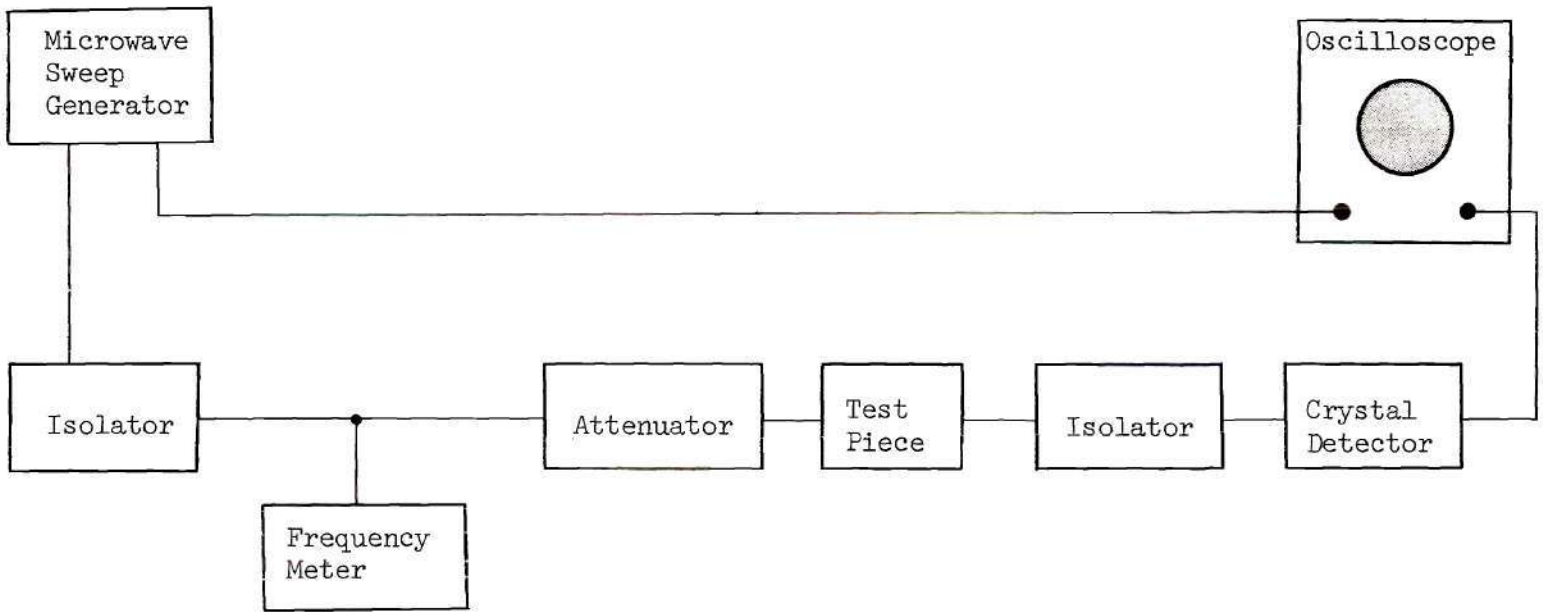

Figure 34. A Block Diagram of the Loosely Coupled Transmission Resonance Experimental Setup

through the test piece. The detected signal appeared as a high Q resonance on the oscilloscope. The frequency of each transmission resonance was determined with a cavity type reaction frequency meter.

Experimental Procedure

The f-β curves were obtained by:

(1) sweeping the microwave generators over the frequency range desired,

(2) monitoring the oscilloscope for the transmission resonances,

(3) determining the frequency of each resonance,

(4) determining the integral value of n for each resonance, and finally

(5) calculating the β and plotting it versus the measured frequency for each observed resonance.

Ferromagnetic Spin Resonance Absorption Experiment

The technique devised to determine the RF magnetic field components was to probe the microstrip with a small sphere of ferrimagnetic material (yttrium-iron garnet or YIG), measure the amount of spin resonance absorption, and calculate the RF fields from the measured absorptions.

Before proceeding with the discussion of this spin resonance absorption setup, it is both helpful and instructive to consider the theory of ferromagnetic spin resonance absorption and the theory by which the RF magnetic field components are calculated from the measured resonance absorptions.

Theory of Ferromagnetic Resonance Absorption

YIG Probe. YIG, a ferrimagnetic garnet, is composed of nonmagnetic

trivalent yttrium, trivalent iron, and oxygen, $Y_3Fe_2(FeO_4)_3$. According to the Néel theory of ferrimagnetism[39] the unpaired electron spins of the Fe^{3+} ions which lie in two nonidentical antiparallel sublattices are taken in total to constitute a single magnetic moment. A more detailed description of the crystal structure and properties of garnets can be found in Lax and Button.[40]

Uniform Precession Mode. If a uniform RF magnetic field, clockwise† circularly polarized in a plane normal to a DC biasing magnetic field $\vec{H}_o$ (clockwise when looking in the direction of the DC field), has an RF frequency near the precession frequency ω_o, then an appreciable amount of energy will be absorbed by the ferrimagnetic sample. At resonance, energy in the RF electromagnetic wave is transferred to the electron spins of the iron ions and as a result the precession angle of the magnetization vector increases from its steady-state alignment along $\vec{H}_o$. The magnetization vector tends to return to its aligned state and the energy lost in doing this appears as a heating of the crystal lattice. On the other hand, if the magnetic field is counterclockwise circularly polarized, there will be no spin resonance absorption exhibited by the YIG. The mode of precession in which all the magnetization vectors of the electron spins are in phase is known as the uniform precession mode.

The precession frequency of the magnetization vector is given by

$$\omega_o = \gamma H_i \tag{3}$$

---

†The clockwise polarization is sometimes referred to as positive polarization. Likewise, counterclockwise polarization is called negative polarization.

where γ is the gyromagnetic ratio (~ 2.8 megahertz/oersted) and H_i is the effective internal magnetic field. The internal magnetic field is a function of the external DC biasing field, the shape and properties of the sample, and the mode of precession of the magnetization.

This ferromagnetic spin resonance is best understood by considering the tensor permeability $\overleftrightarrow{\mu}$ characterizing this material. Wang[41] derives an expression for $\overleftrightarrow{\mu}$ in which magnetic losses are neglected. The permeability tensor is then given by

$$\overleftrightarrow{\mu} = \begin{bmatrix} \mu & +j\kappa & 0 \\ -j\kappa & \mu & 0 \\ 0 & 0 & \mu_o \end{bmatrix} \tag{4}$$

where

$$\mu = \mu_o \left(1 + \frac{\omega_M \omega_o}{\omega_o^2 - \omega^2}\right) \tag{5}$$

$$\kappa = \frac{\mu_o \omega \omega_M}{\omega_o^2 - \omega^2} \tag{6}$$

and μ_o is the permeability of free space, $\omega_M = \gamma\mu_o M$, and M is the spontaneous magnetization. In this derivation, all time varying terms of order higher than the first will be neglected and only the uniform precession mode is considered. Thus the fields considered must be at low RF power levels.

The tensor permeability can be reduced to a scalar form by following the standard development where one assumes that the sample is excited by a uniform clockwise (CW) circularly polarized magnetic field in a plane

normal to the DC magnetic field. The DC field will be assumed to be in the +z direction for the development of the scalar permeabilities. The components of the CW field are denoted as:

$$h_x = h_+ \qquad h_y = -jh_+ \tag{7}$$
$$b_x = b_+ \qquad b_y = -jb_+$$

For a counterclockwise (CCW) circularly polarized magnetic field, the components are denoted as:

$$h_x = h_- \qquad h_y = +jh_- \tag{8}$$
$$b_x = b_- \qquad b_y = +jb_-$$

The total RF magnetic field intensity can then be written as

$$h_x = h_+ + h_- \qquad h_y = -j(h_+ - h_-) \tag{9}$$

and the total RF magnetic flux density is

$$b_x = b_+ + b_- \qquad b_y = -j(b_+ - b_-) \tag{10}$$

However, $\vec{b}$ and $\vec{h}$ are related by the permeability tensor of Equation (4).

$$b_x = \mu h_x + j\kappa h_y \tag{11}$$
$$b_y = -j\kappa h_x + \mu h_y$$

Substituting Equations (9) and (10) into Equation (11) yields

$$b_+ + b_- = \mu(h_+ + h_-) + j\kappa(-j(h_+ - h_-)) \tag{12}$$

$$-j(b_+ - b_-) = -j\kappa(h_+ + h_-) + \mu(-j(h_+ - h_-))$$

and after rearranging yields

$$b_+ + b_- = (\mu + \kappa)\, h_+ + (\mu - \kappa)\, h_- \tag{13}$$

$$b_+ - b_- = (\mu + \kappa)\, h_+ - (\mu - \kappa)\, h_-$$

Thus

$$b_+ = (\mu + \kappa)\, h_+ \qquad b_- = (\mu - \kappa)\, h_- \tag{14}$$

The scalar quantities $(\mu + \kappa)$ and $(\mu - \kappa)$ are the effective permeabilities for the clockwise and counterclockwise circularly polarized waves, respectively. Upon substitution of Equations (5) and (6), they become

$$\mu + \kappa = \mu_o + \frac{\mu_o \omega_M \omega_o}{\omega_o^2 - \omega^2} + \frac{\mu_o \omega \omega_M}{\omega_o^2 - \omega^2} = \mu_o + \frac{\mu_o \omega_M\, (\omega_o + \omega)}{\omega_o^2 - \omega^2} \tag{15}$$

$$\mu - \kappa = \mu_o + \frac{\mu_o \omega_M \omega_o}{\omega_o^2 - \omega^2} - \frac{\mu_o \omega \omega_M}{\omega_o^2 - \omega^2} = \mu_o + \frac{\mu_o \omega_M\, (\omega_o - \omega)}{\omega_o^2 - \omega^2}$$

Factoring the denominator and canceling terms yields

$$\mu + \kappa = \mu_o + \frac{\mu_o \omega_M}{\omega_o - \omega} \tag{16}$$

$$\mu - \kappa = \mu_o + \frac{\mu_o \omega_M}{\omega_o + \omega}$$

Whenever the RF frequency ω equals the precession frequency ω_o,

$$\mu - K = \mu_o \left(1 + \frac{\omega_M}{2\omega_o}\right) \tag{17}$$

but $\mu + K$ becomes undefined due to the division by zero. When magnetic losses are included, the resonance absorption is finite rather than infinite as it is here. The CCW fields exhibit no resonance loss due to spin coupling effects whereas the CW fields show a strong resonance absorption.

Walker Modes. It was assumed that the RF magnetic field was uniform over the YIG sphere in the previously discussed ferromagnetic spin resonance absorption theory. Other modes of precession are possible in the YIG sphere and nonuniform magnetic fields can excite them. If the driving field is not uniform, then it is possible that the magnetization vector in different regions of the YIG sphere will be driven nonuniformally. Then, in addition to the principal uniform precession mode, other modes of absorption will appear at different RF frequencies. The appearance of these other modes, called Walker or magnetostatic modes, reduces the amount of absorption of the uniform mode. An analysis of Walker modes is found in Lax and Button[42] and the reader is referred there for a theoretical discussion of the modes.

In this research, the nonuniform modes which appeared were not theoretically analyzed. Instead, their appearance was only noted to indicate that the absorption by the principal uniform precession mode was probably reduced.

Determination of the RF Magnetic Field Components from the Measured Spin Resonance Absorption

The RF magnetic field was experimentally determined in component pairs: (h_z,h_x) and (h_z,h_y). This resulted because the field data were calculated from measured resonance absorptions as a function of the DC magnetic field orientations. In the experiment $\vec{H}_o$ was oriented in the $\pm x$ and $\pm y$ directions and microwave energy propagated in the $+z$ direction.

In general, the magnetic field components are expressed as

$$H_z = h_z \cos(\omega t - \beta z) \tag{18}$$

$$H_y = h_y \sin(\omega t - \beta z)$$

$$H_x = h_x \sin(\omega t - \beta z)$$

Maxwell's equations require that the transverse fields be in time quadrature with the longitudinal fields, thus, in either the xz- or yz-planes, the resultant magnetic field is elliptically polarized.

Resolution of the Elliptically Polarized Field into Two Circularly Polarized Fields. For the orientation of Figure 35, the DC biasing magnetic field is normal to the plane of the substrate. With this orientation, the plane of polarization of interest is the xz-plane and the fields are

$$H_z = h_z \cos(\omega t - \beta z) \tag{19}$$

$$H_x = h_x \sin(\omega t - \beta z)$$

These result in an elliptically polarized field in the xz-plane.

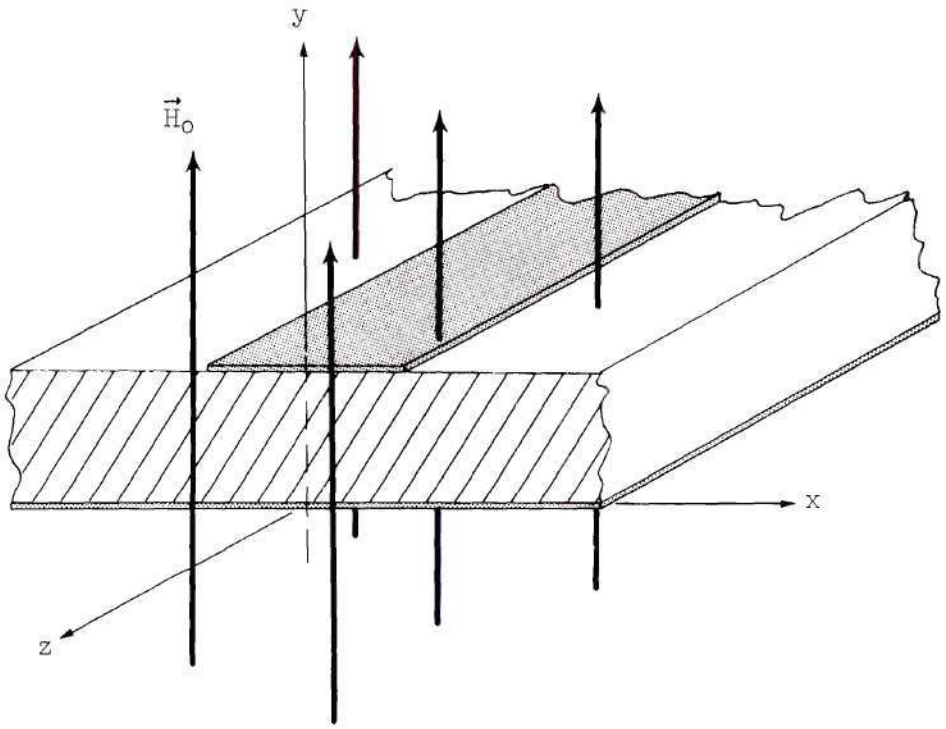

Figure 35. Orientation of the DC Magnetic Field Normal to the Plane of the Substrate

An elliptically polarized field can be resolved into two circularly polarized fields rotating in opposite directions.

$$\vec{H}_{xz} = \vec{a}_z h_z \cos(\omega t - \beta z) + \vec{a}_x h_x \sin(\omega t - \beta z) \tag{20}$$

$$= \vec{a}_z \frac{h_z}{2} \cos(\omega t - \beta z) + \vec{a}_x \frac{h_z}{2} \sin(\omega t - \beta z) + \vec{a}_z \frac{h_z}{2} \cos(\omega t - \beta z)$$

$$- \vec{a}_x \frac{h_z}{2} \sin(\omega t - \beta z) + \vec{a}_x \frac{h_x}{2} \sin(\omega t - \beta z) + \vec{a}_z \frac{h_x}{2} \cos(\omega t - \beta z)$$

$$+ \vec{a}_x \frac{h_x}{2} \sin(\omega t - \beta z) - \vec{a}_z \frac{h_x}{2} \cos(\omega t - \beta z)$$

Rearranging and combining terms, yields

$$\vec{H}_{xz} = \vec{a}_z \left(\frac{h_z}{2} + \frac{h_x}{2}\right) \cos(\omega t - \beta z) + \vec{a}_x \left(\frac{h_z}{2} + \frac{h_x}{2}\right) \sin(\omega t - \beta z) \qquad (21)$$

$$+ \vec{a}_z \left(\frac{h_z}{2} - \frac{h_x}{2}\right) \cos(\omega t - \beta z) - \vec{a}_x \left(\frac{h_z}{2} - \frac{h_x}{2}\right) \sin(\omega t - \beta z)$$

The first two terms constitute a circularly polarized field of amplitude $\frac{h_z}{2} + \frac{h_x}{2}$ which is rotating in the same sense as the original elliptical field. The last two terms constitute a circularly polarized field of amplitude $\frac{h_z}{2} - \frac{h_x}{2}$ rotating in an opposite sense.

If the RF magnetic field is such that h_z and h_x are both positive, then the field in the xz-plane is

$$\vec{H}_{xz} = \vec{a}_z h_z \cos(\omega t - \beta z) + \vec{a}_x h_x \sin(\omega t - \beta z) \qquad (22)$$

which rotates CW about the DC field (see Figure 35). Resolution of this field yields two circularly polarized fields, one of magnitude $\left(\frac{h_z}{2} + \frac{h_x}{2}\right)$ rotating clockwise and one of magnitude $\left(\frac{h_z}{2} - \frac{h_x}{2}\right)$ rotating counterclockwise.

If the RF field is such that h_z is positive and h_x is negative, then the field is

$$\vec{H}_{xz} = \vec{a}_z |h_z| \cos(\omega t - \beta z) - \vec{a}_x |h_x| \sin(\omega t - \beta z) \qquad (23)$$

Resolution yields a CW field of amplitude $\left(\frac{|h_z|}{2} - \frac{|h_x|}{2}\right)$ and a CCW field

of amplitude $\left(\frac{|h_z|}{2} + \frac{|h_x|}{2}\right)$.

If the direction of the DC magnetic field is reversed, then for the field of Equation (22), the circularly polarized component rotating CW has an amplitude $\left(\frac{h_z}{2} - \frac{h_x}{2}\right)$ and the component rotating CCW has an amplitude $\left(\frac{h_z}{2} + \frac{h_x}{2}\right)$. The field of Equation (23) has a CW field of amplitude $\left(\frac{|h_z|}{2} + \frac{|h_x|}{2}\right)$ and a CCW field of amplitude $\left(\frac{|h_z|}{2} - \frac{|h_x|}{2}\right)$.

For the orientation in which the DC magnetic field is parallel to the plane of the substrate as in Figure 36, the fields lying in this yz-plane are

$$H_z = h_z \cos(\omega t - \beta z) \qquad H_y = h_y \sin(\omega t - \beta z) \tag{24}$$

Resolving the elliptically polarized field having these components into two circularly polarized fields results in

$$\vec{H}_{yz} = \vec{a}_z \left(\frac{h_z}{2} + \frac{h_y}{2}\right) \cos(\omega t - \beta z) + \vec{a}_y \left(\frac{h_z}{2} + \frac{h_y}{2}\right) \sin(\omega t - \beta z) \tag{25}$$
$$+ \vec{a}_z \left(\frac{h_z}{2} - \frac{h_y}{2}\right) \cos(\omega t - \beta z) - \vec{a}_y \left(\frac{h_z}{2} - \frac{h_y}{2}\right) \sin(\omega t - \beta z)$$

For a positive h_z and negative h_y, the elliptically polarized field is

$$\vec{H}_{yz} = \vec{a}_z |h_z| \cos(\omega t - \beta z) - \vec{a}_y |h_y| \sin(\omega t - \beta z) \tag{26}$$

which is a CW field when looking in the direction of the DC magnetic

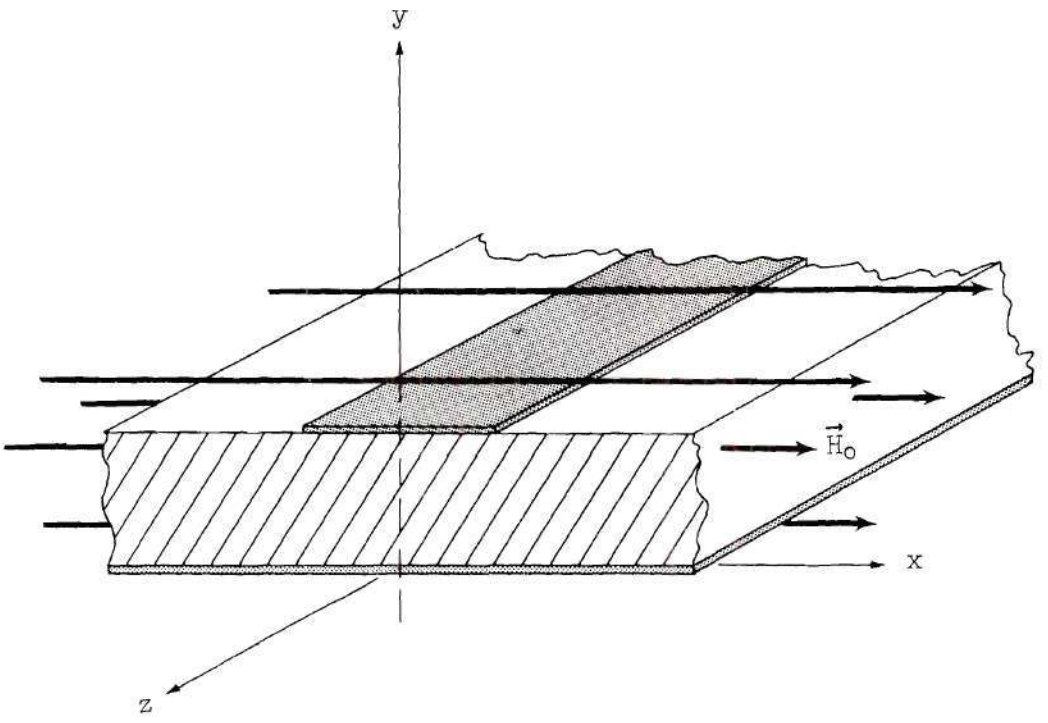

Figure 36. Orientation of the DC magnetic Field in the Plane of the Substrate

field. Resolution yields a CW rotating field of amplitude $\left(\frac{|h_z|}{2} + \frac{|h_y|}{2}\right)$ and a CCW rotating field of amplitude $\left(\frac{|h_z|}{2} - \frac{|h_y|}{2}\right)$. A positive h_z and h_y yields a CCW elliptically polarized field given by

$$\vec{H}_{yz} = \vec{a}_z|h_z|\cos(\omega t - \beta z) + \vec{a}_y|h_y|\sin(\omega t - \beta z) \qquad (27)$$

Resolution of this wave yields a CW rotating field of amplitude $\left(\frac{|h_z|}{2} - \frac{|h_y|}{2}\right)$ and a CCW rotating field of amplitude $\left(\frac{|h_z|}{2} + \frac{|h_y|}{2}\right)$. Reversing the DC field direction results in a simple interchange of the amplitudes of the CW and CCW fields.

Tables 4 and 5 provide a summary of the amplitude of the CW components as functions of the signs of the RF magnetic field components and the directions of the DC biasing field. Note that the amplitudes of the CW fields remain the same when the signs of both components are reversed. This is why the absolute value symbol is on the amplitude expressions. For example, in Table 4, the RF field components $+h_z$, $+h_x$ and $-h_z$, $-h_x$ both have the same magnitude of CW circularly polarized field.

Table 4. Field Amplitudes and Polarizations for a DC Field Normal to the Plane of the Substrate

Field Component Magnitudes	Polarizations of the Elliptical Field	Amplitudes of CW Circularly Polarized Field in xz-Plane	
		$\vec{H}_o = H_o\vec{a}_y$	$\vec{H}_o = -H_o\vec{a}_y$
$+h_z, +h_x$ or $-h_z, -h_x$	CW CW	$\left\lvert \frac{\lvert h_z \rvert}{2} + \frac{\lvert h_x \rvert}{2} \right\rvert$	$\left\lvert \frac{\lvert h_z \rvert}{2} - \frac{\lvert h_x \rvert}{2} \right\rvert$
$+h_z, -h_x$ or $-h_z, +h_x$	CCW CCW	$\left\lvert \frac{\lvert h_z \rvert}{2} - \frac{\lvert h_x \rvert}{2} \right\rvert$	$\left\lvert \frac{\lvert h_z \rvert}{2} + \frac{\lvert h_x \rvert}{2} \right\rvert$

The relative signs of the magnetic field components contributing to the resonance absorption are easily determined using Tables 4 and 5. For example, consider the orientation corresponding to Table 4. If the absorption measured for an $\vec{H}_o$ in the minus y direction is greater than

that for $\vec{H}_o$ in the plus y direction, then immediately it is known that the components comprising the field are of opposite sign.

Table 5. Field Amplitudes and Polarizations for a DC Field Parallel to the Plane of the Substrate

Field Component Magnitudes	Polarizations of the Elliptical Field	Amplitudes of CW Circularly Polarized Field in yz-Plane	
		$\vec{H}_o = H_o\vec{a}_x$	$\vec{H}_o = -H_o\vec{a}_x$
$+h_z, +h_y$ or $-h_z, -h_y$	CCW CCW	$\left\lvert \frac{\lvert h_z \rvert}{2} - \frac{\lvert h_y \rvert}{2} \right\rvert$	$\left\lvert \frac{\lvert h_z \rvert}{2} + \frac{\lvert h_y \rvert}{2} \right\rvert$
$+h_z, -h_y$ or $-h_z, +h_y$	CW CW	$\left\lvert \frac{\lvert h_z \rvert}{2} + \frac{\lvert h_y \rvert}{2} \right\rvert$	$\left\lvert \frac{\lvert h_z \rvert}{2} - \frac{\lvert h_y \rvert}{2} \right\rvert$

Relationship Between the Measured Resonance Absorption and the Magnitude of the RF Magnetic Field. The measured resonance absorption data is the ratio in dB of the power levels out of the microstrip line at resonance to that at off resonance, i.e. it is the power in dB absorbed by the YIG sphere. The measurement technique will be explained in detail in the section on experimental procedure. A relationship is derived which relates the magnitude of the spin resonance absorption to the magnitude of the CW circularly polarized magnetic field which causes the resonance absorption.

The connection between the power absorbed and the RF driving field

is found by considering the term $\vec{H} \cdot \frac{\partial \vec{B}^{*}}{\partial t}$† which represents a power density in the complex Poynting theorem.‡ The rate of change of stored energy in a unit volume is then

$$P = \int_V \vec{H} \cdot \frac{\partial \vec{B}^{*}}{\partial t} \, dV = j\omega \int_V \overleftrightarrow{\mu} \, |\vec{H}|^2 \, dV \tag{28}$$

and the power absorbed per unit volume is

$$P/u.v. = j\omega \overleftrightarrow{\mu} \, |\vec{H}|^2 \tag{29}$$

It has already been shown that an elliptically polarized RF magnetic field can be resolved into two circularly polarized fields, one CW and the other CCW about a normal to the plane of the polarization.

$$P/u.v. = j\omega \overleftrightarrow{\mu} \, |\vec{H}_{CW} + \vec{H}_{CCW}|^2 \tag{30}$$

$$= j\omega \overleftrightarrow{\mu} \, (\vec{H}_{CW} + \vec{H}_{CCW}) \cdot (\vec{H}_{CW} + \vec{H}_{CCW})^{*}$$

$$= j\omega \overleftrightarrow{\mu} \, (|\vec{H}_{CW}|^2 + |\vec{H}_{CCW}|^2 + \vec{H}_{CW} \cdot \vec{H}^{*}_{CCW} + \vec{H}_{CCW} \cdot \vec{H}^{*}_{CW})$$

$$P/u.v. = j\omega \overleftrightarrow{\mu} \, (|\vec{H}_{CW}|^2 + |\vec{H}_{CCW}|^2) + j\omega \overleftrightarrow{\mu} \, (\vec{H}_{CW} \cdot \vec{H}^{*}_{CCW} + \vec{H}_{CCW} \cdot \vec{H}^{*}_{CW}) \tag{31}$$

The second term of Equation (31) is zero. This is shown by letting

---

†The asterisk implies the complex conjugate.

‡Poynting's theorem is discussed in practically all fundamental electromagnetic field theory testbooks, for example, Paris and Hurd.[43]

$$\vec{H}_{CW} = A(\vec{a}_z - j\vec{a}_x)\, e^{j(\omega t - \beta z)} \tag{32}$$

$$\vec{H}_{CCW} = B(\vec{a}_z + j\vec{a}_x)\, e^{j(\omega t - \beta z)}$$

and by letting

$$\theta = \omega t - \beta z \tag{33}$$

Performing the dot product operation yields

$$\vec{H}_{CW}\cdot\vec{H}^{*}_{CCW} = Ae^{j\theta}B^{*}e^{-j\theta} + (-jAe^{j\theta})(-jB^{*}e^{-j\theta}) \tag{34}$$

$$= AB^{*} - AB^{*} = 0$$

and

$$\vec{H}_{CCW}\cdot\vec{H}^{*}_{CW} = Be^{j\theta}A^{*}e^{-j\theta} + (jBe^{j\theta})(jA^{*}e^{-j\theta}) \tag{35}$$

$$= BA^{*} - BA^{*} = 0$$

The power absorbed per unit volume is then

$$P/u.v. = j\omega\, \overleftrightarrow{\mu}\, (|\vec{H}_{CW}|^2 + |\vec{H}_{CCW}|^2) \tag{36}$$

$$= j\omega\, \overleftrightarrow{\mu}\, |\vec{H}_{CW}|^2 + j\omega\, \overleftrightarrow{\mu}\, |\vec{H}_{CCW}|^2$$

It has been shown that, for RF magnetic fields which are circularly polarized, the permeability tensor of Equation (4) can be represented as two effective scalar permeabilities, one for each direction of

circular polarization. Substituting these effective permeabilities of Equation (16) into Equation (36) yields

$$P/u.v. = j\omega\left(\mu_o + \frac{\mu_o\omega_M}{\omega_o - \omega}\right)|\vec{H}_{CW}|^2 + j\omega\left(\mu_o + \frac{\mu_o\omega_M}{\omega_o + \omega}\right)|\vec{H}_{CCW}|^2 \qquad (37)$$

As the RF frequency is varied through ω_o, the first term will have a zero in the denominator and will exhibit a resonance, whereas the second term will experience a negligible change. The size of the YIG sphere remains constant so, as a result, at a resonance the power absorbed by the sample is proportional to the square of the magnitude of that CW circularly polarized component of the magnetic field.

$$P_{absorbed} \propto |H_{CW}|^2 \qquad (38)$$

From equations like Equations (21) and (25), the components of the CW circularly polarized field are related to the components of the RF magnetic field. Thus the power absorbed is proportional to terms like $\left|\frac{|h_z|}{2} \pm \frac{|h_x|}{2}\right|^2$ or $\left|\frac{|h_z|}{2} \pm \frac{|h_y|}{2}\right|^2$.

The power absorbed at resonance was not measured directly. Instead, it was the ratio in dB of the "at resonance" and the "off resonance" power levels which were transmitted through the section.

$$\text{Absorption in dB} = 10 \log \left(\frac{\text{Power}_{\text{off resonance}}}{\text{Power}_{\text{at resonance}}}\right) \qquad (39)$$

$$= 10 \log \left(\frac{\text{Power}_{\text{off resonance}}}{\text{Power}_{\text{off resonance}} - \text{Power}_{\text{absorbed}}}\right)$$

$$= 10 \log \left(\frac{1}{1 - \frac{\text{Power}_{\text{absorbed}}}{\text{Power}_{\text{off resonance}}}} \right)$$

Rearranging this equation yields

$$\frac{\text{Power}_{\text{absorbed}}}{\text{Power}_{\text{off resonance}}} = 1 - \frac{1}{\text{antilog} \left(\frac{\text{Absorption in dB}}{10} \right)} \qquad (40)$$

The power level into the microstrip line is kept constant so that the

$$\text{Power}_{\text{absorbed}} \propto 1 - \frac{1}{\text{antilog} \left(\frac{\text{Absorption in dB}}{10} \right)} \qquad (41)$$

Combining Equations (38) and (41) yields

$$|H_{CW}| \propto \left(1 - \frac{1}{\text{antilog} \left(\frac{\text{Absorption in dB}}{10} \right)} \right)^{\frac{1}{2}} \qquad (42)$$

Thus by Equation (42) the amount of resonance absorption is related to the CW circularly polarized component of the magnetic field.

RF Magnetic Field Component Calculations. The procedure for calculating the field components from the experimental data was to:

(1) measure the magnitude of the absorption for the two anti-parallel DC magnetic field orientations of Figure 36 (the experimental techniques for measuring absorption will be discussed in detail in a later section),

(2) determine the relative signs of the two field components

from the measured absorptions with the aid of Table 5,

(3) calculate the relative magnitude of the CW circularly polarized component of the RF magnetic field for each antiparallel orientation by Equation (42),

(4) relate the larger value of step (3), call it H_{CW1}, to $\left|\frac{|h_z|}{2} + \frac{|h_y|}{2}\right|$ and the lesser value, call it H_{CW2}, to $\left|\frac{|h_z|}{2} - \frac{|h_y|}{2}\right|$,

(5) solve these to yield $h_z = H_{CW1} \pm H_{CW2}$ and $h_y = H_{CW1} \mp H_{CW2}$ (the choice of signs is not determined until step (7),

(6) repeat steps (1) through (5) to solve for the values of h_z and h_x using Table 4 for the orientation of Figure 35, and finally,

(7) determine the values for h_x, h_y, and h_z by comparing the results of step (5) and using the signs which make the two calculations for h_z, from the two orthogonal orientations, the closest.

Spin Resonance Experimental Setup

Microstrip Lines. Three microstrip lines, selected from the group of lines used in the transmission resonance experiment, were modified for use in the spin resonance absorption experiment. The short circuits on the ends of each microstrip line were removed. Since the characteristic impedance of the experimental system was 50 ohms, the line whose impedance was 50 ohms needed no alterations. However, the alumina lines with ratios of strip width to substrate thickness of two, having characteristic impedances of approximately 33 ohms, had to be matched to the system to eliminate any standing waves. This was accomplished by etching a one inch taper on each end of the test line so that

the input and output impedances were about 50 ohms. With this taper standing waves were minimized and the 33 ohm portion of the line could be probed for the true fields.

Test Piece. A photograph of the test piece showing the tapers on the line, the brass base, the OSM connectors and the OSM to type N adaptors is shown in Figure 37. The connection between the center conductor of the OSM connector and the center strip of the microstrip line was a pressure fit connection. It was not necessary to solder these two conductors for proper connection.

Equipment. The equipment used in this experiment is shown in the center and on the right hand side of the photograph of Figure 33. The setup used in the ferromagnetic spin resonance absorption experiment is block diagrammed in Figure 38. The source for the single frequency microwave signal was a Hewlett-Packard model 620A SHF signal generator. This particular instrument is noted for its frequency and output power stability. The magnitude of the resonance absorption was measured with an SWR indicator calibrated to read power levels in dB below a set level. The power meter was used to ensure against power levels exceeding one milliwatt, otherwise, a large resonant absorption could cause heating of the YIG sphere, resulting in an increase in the line width and a decrease in the "on resonance" permeability. The double stub tuners were used to match out the residual discontinuity between the connectors and the microstrip. The gaussmeter was used to measure the flux density between the poles of the electromagnet.

The DC biasing magnetic field was supplied by the regulated electromagnet. The poles of the electromagnet with a test piece between

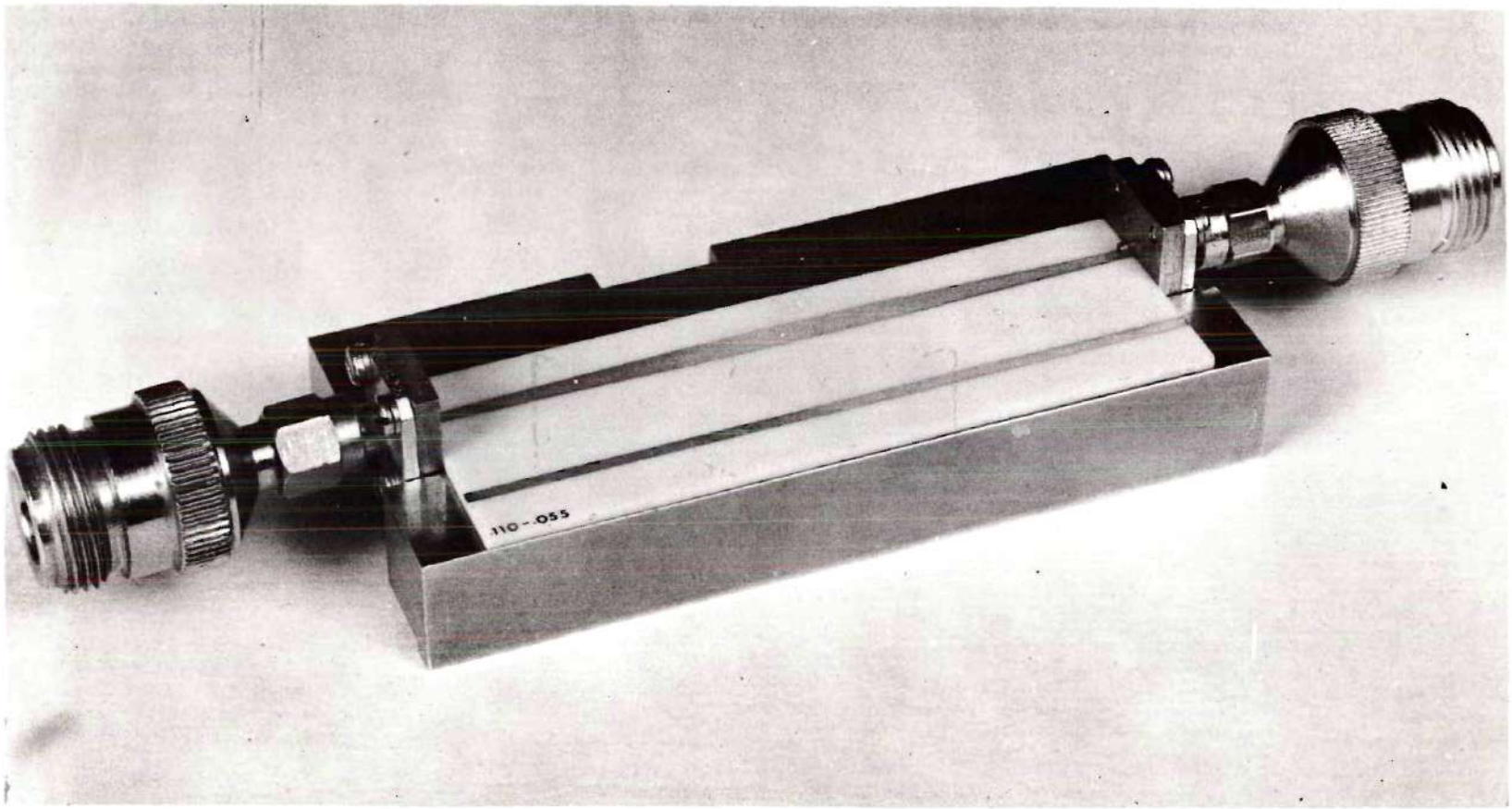

Figure 37. Photograph of the Microstrip Test Piece

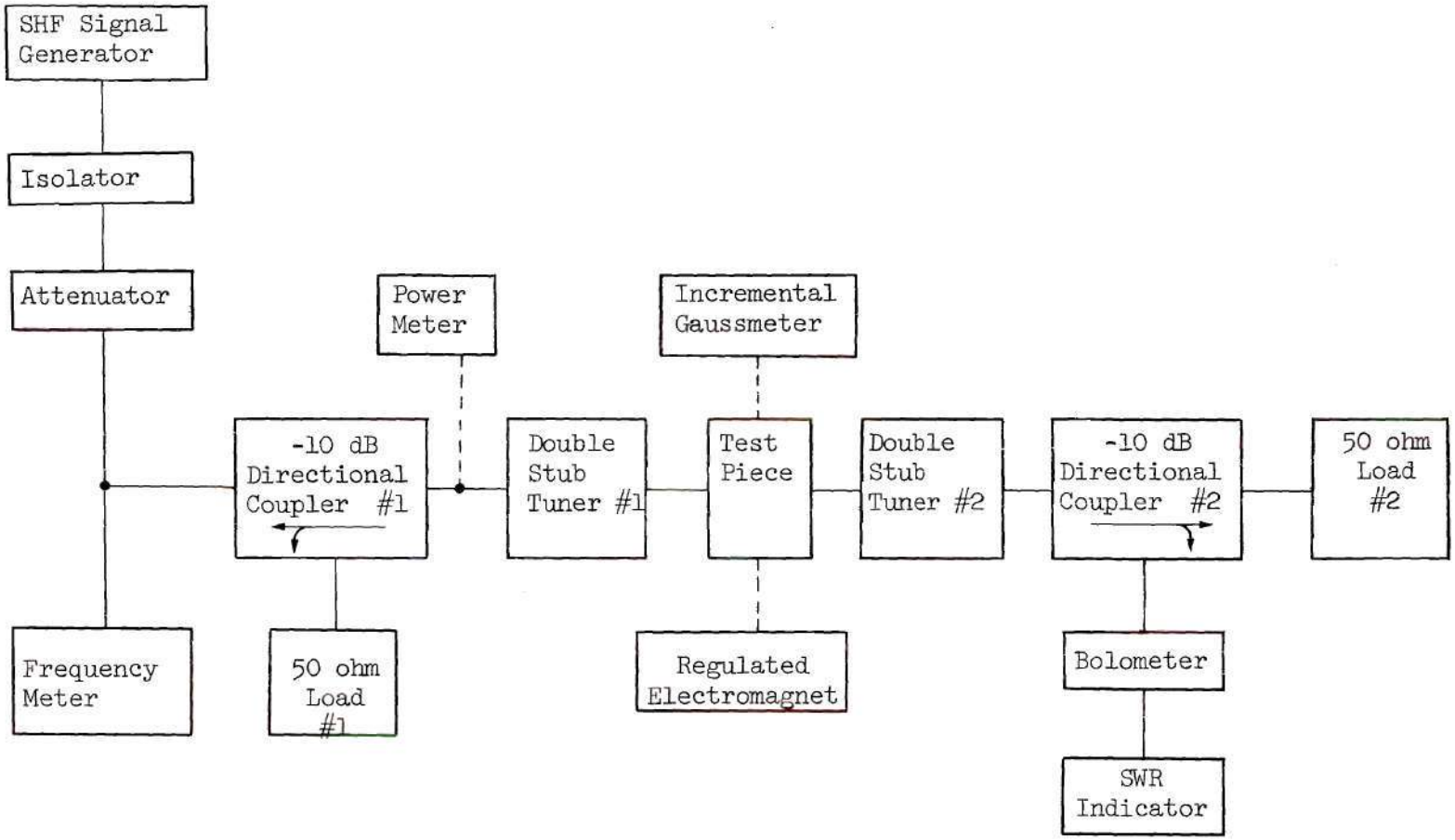

Figure 38. A Block Diagram of the Ferromagnetic Spin Resonance Absorption Experimental Setup

them are pictured in Figure 39.

To obtain a significant amount of resonance absorption with a small sample, a material having a narrow resonance line width[†] must be used. A single crystal YIG sphere was chosen since its line width is much narrower than that of other ferrimagnetic materials. To prevent a dielectric loading effect (perturbation of the field distribution) on the microstrip surface, the high dielectric constant YIG sphere ($\kappa = 16$) had to be small. The YIG sphere probe (the small dot beside the tapered line in Figure 39) had a diameter of 0.0164 inch and a line width of 0.27 oersted.

Experimental Procedures

The resonance absorption experiment was composed of two procedures. The first was to check the VSWR of the test piece and match out any residual discontinuities. A standing wave in the microstrip would lead to incorrect field calculations. The second was to record the magnitudes of the resonance absorptions of the YIG sphere at different positions on the microstrip interface for each of the four orthogonal orientations of the DC biasing field. From these measured absorptions the relative magnetic field components were calculated.

VSWR Determinations and Subsequent Reductions. The VSWR versus frequency of the test piece was measured on a Hewlett-Packard automatic network analyzer. This provided the information needed to pick a frequency where the mismatches of the two connectors were small.

The mismatch due to the connector on the generator side was re-

---

[†]Line width is the width of the resonance absorption curve at half-maximum absorption.

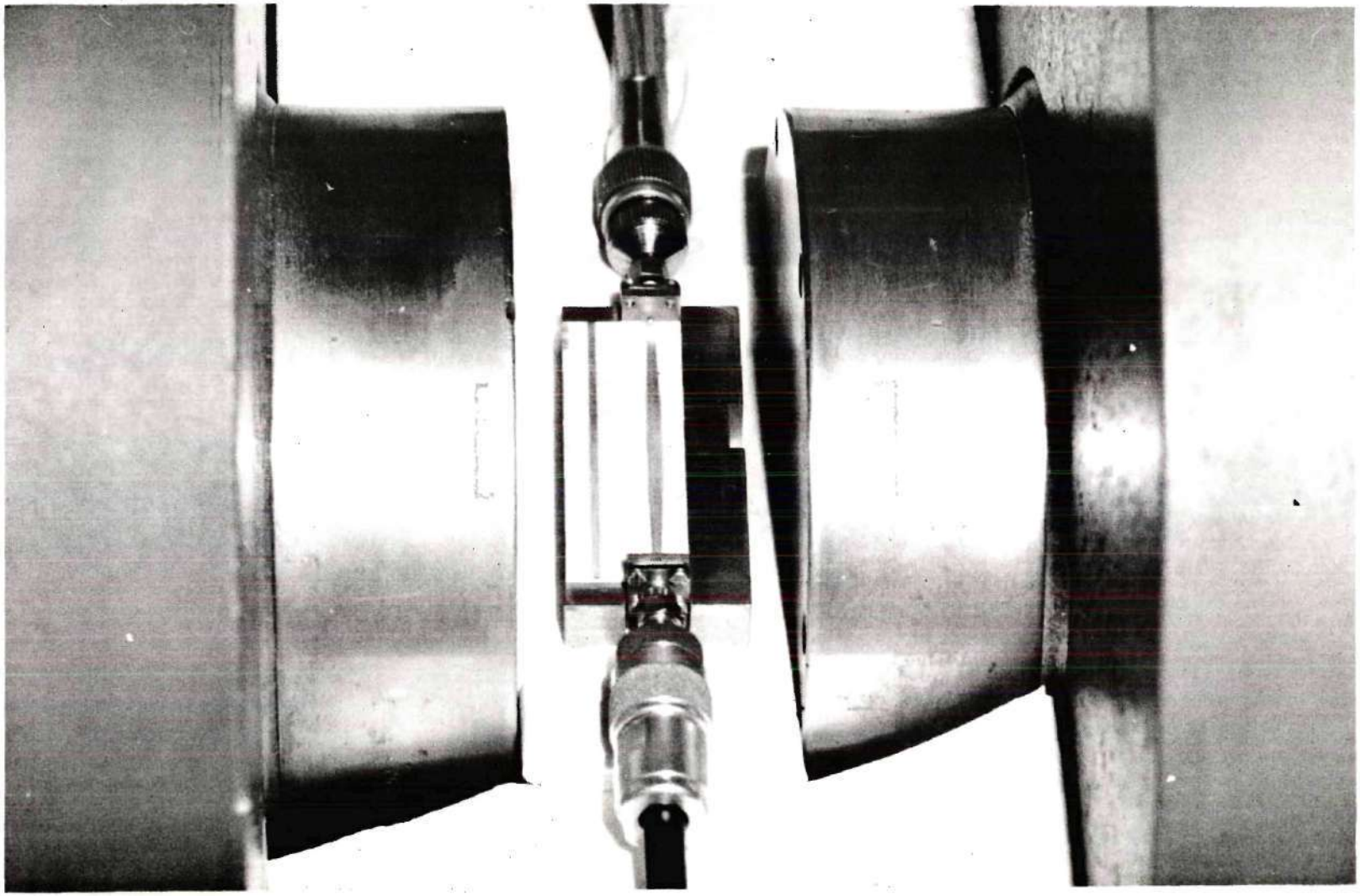

Figure 39. A Photograph of the Microstrip Test Piece Between the Poles of the Electromagnet

duced by:

(1) replacing the 50 ohm load #1 with the bolometer and SWR indicator,

(2) laying a piece of load material, polyiron, on the center strip of the microstrip line, and

(3) tuning double stub tuner #1 until there was minimum reflected power from the connector mismatch.

The mismatch of the connector on the load side was reduced by:

(1) replacing the 50 ohm load #2 with the output of the signal generator and isolator combination,

(2) connecting the bolometer and SWR indicator to the arm of directional coupler #2,

(3) laying the load material on the center strip, and

(4) tuning double stub tuner #2 until there was a minimum of reflected power from the connector.

As long as the frequency of operation was not changed, the microstrip line retained a minimum reflected wave after this tuning procedure.

Ferromagnetic Spin Resonance Absorption Measurements. The spin resonance absorption measurements were made with the setup of Figure 38. A frequency was selected and the generator power was adjusted for a power level of less than a milliwatt. The procedure for measuring the absorption was to:

(1) select a location in the plane of the interface on the line and affix the YIG sphere to the line with a small amount of glue,

(2) connect the test piece to the system and orient it between

the poles of the electromagnet,

(3) set the SWR indicator at zero dB,

(4) vary the magnetic field of the electromagnet and watch for resonance absorptions,

(5) measure the magnitudes of the absorptions in dB with the SWR indicator,

(6) measure the field strength of the DC biasing magnetic field with the gaussmeter,

(7) rotate the test piece by 90° and repeat steps (4) through (7) until the absorptions of the four orthogonal orientations have been measured,

(8) remove the YIG spheres with acetone, and

(9) repeat steps (1) through (9) at different locations in the transverse plane of the microstrip.

Experimental Precautions. Several precautions had to be observed to ensure success of the experimental measurements. The slides of the double stub tuners were taped after their adjustment to keep them from sliding and upsetting the system. Care had to be taken in the pressure fitting of the OSM connectors to the microstrip's center strip as an overpressure could break the substrate. The YIG sphere had to be handled with extreme care to keep it from being lost. In particular, after gluing the sphere to the substrate, it had to be checked to make sure that it was firmly attached before placing the test piece in the electromagnet.

Experimental Error

Four types of experimental error were evident in performing the previously discussed experimental procedures. The following list is not all inclusive but it does represent those types which account for most of the error:

(1) errors inherent in the measuring equipment,

(2) errors arising from reading the instruments,

(3) errors arising from inaccurate physical placement of the test piece and YIG sphere probe, and

(4) errors arising from the YIG sphere loading of the substrate.

Transmission Resonance Experiment

In the transmission resonance experiment, the frequency meter was the critical piece of measurement equipment. It had a calibrated accuracy of 0.2 percent, and the maximum error in reading the absorption blip on the oscilloscope was about 0.5 percent. The resonant frequency was shifted from its true value due to the coupling effects of the loops. This error is reasoned to be less than one percent for loose coupling. The resonant section was three inches long, but the exact location of the short circuits was not known accurately. The electrical length was estimated to be within 1.5 percent of the three inch length. It was believed that the maximum experimental error in this particular experiment amounted to approximately five percent, and is largely systematic error.

Spin Resonance Absorption Experiment

In the ferromagnetic spin resonance absorption experiment the critical piece of measuring equipment was the SWR indicator which had an

inherent maximum error of 0.2 percent. For absorptions between six and ten dB, the meter could be read to within about 0.2 dB. For absorptions up to around one dB the expanded scale could be read to within 0.02 dB. The SHF generator's frequency was accurate to within about 0.5 percent. The position of the YIG sphere for each run was read to within 0.0005" with a Nikon profile projector.

There were other sources of error which could not be accurately estimated. Some error was introduced when the DC biasing magnetic field was not exactly parallel to or perpendicular to the substrate interface. Despite the precautions taken to eliminate standing waves, a small amount of reflected energy still existed on the line and perturbed the measurement of the fields of the dominant propagating mode. In regions of the substrate surface where nonuniform (Walker) modes were excited, a reduction in the peak of the uniform resonance absorption curve resulted in some error in the calculated fields.

The relative size of the YIG probe was a limiting factor in the amount of error obtained. The larger the sphere, in comparison with the microstrip, the larger the perturbation of the field pattern. For the experiment with the .055" alumina substrate with w/b = 2, the relative size of the sphere was small. However, for the other two experiments the relative size of the sphere became larger and the difference between the actual measured fields and the theoretically calculated fields of the unloaded microstrip increased accordingly. In regions away from the center strip, the perturbation caused by the high dielectric constant YIG sphere loading of the substrate increased as the fields were drawn

out into it. The result of this field displacement was that the symmetry of the mode pattern was distorted and away from the center strip the experimentally determined field distribution was not an accurate representation of the real distribution. It is believed that the total maximum error for the experiment ranged from about ten percent in the vicinity of the center strip to twenty percent and higher as the distance from the strip increased.

CHAPTER V

EXPERIMENTAL RESULTS AND COMPARISONS WITH THEORETICAL CALCULATIONS

This chapter presents the results of the experimental procedures discussed in the previous chapter and compares them with the theoretical results discussed in Chapter III. The experimentally determined f-β diagrams were prepared from the measured data of the loosely coupled transmission resonance experiment. The experimental determinations of the RF magnetic field components were calculated from the data taken with the ferromagnetic spin resonance absorption experiment. Comparisons are made between the experimental and theoretical results of this work and with the results reported by other investigators. Together, the theoretical and experimental results provide a more complete understanding of the microstrip mode than had previously been obtained.

Loosely Coupled Transmission Resonance Results

The loosely coupled transmission resonance experiment was set up according to the block diagram of Figure 34 and performed according to the experimental procedure outlined in Chapter IV.

The transmissions, which occur through each of the resonant microstrip lines whenever the line length, ℓ, is an integral number, n, of guide half-wavelengths long, can be indexed as tabulated in Table 6. This table relates the index number, n, to the guide wavelength, λ_g, and

Table 6. The Relationship Between n, λ_g, and β for a Three Inch Substrate

n	λ_g (cm)	β (rad/cm)
1	15.24	.41
2	7.62	.82
3	5.08	1.24
4	3.81	1.65
5	3.05	2.06
6	2.54	2.48
7	2.18	2.89
8	1.91	3.30
9	1.69	3.71
10	1.52	4.12
11	1.38	4.54
12	1.27	4.95
13	1.17	5.36
14	1.09	5.77
15	1.02	6.18
16	0.95	6.60
17	0.90	7.01
18	0.85	7.42
19	0.80	7.83
20	0.76	8.24

the phase constant, β. ($\beta = \frac{2\pi}{\lambda_g} = \frac{n\pi}{\ell}$ as shown in Equation (2) of Chapter IV.)

Experimental Measurements

Loosely coupled transmission measurements were made on each of the six prepared microstrip lines listed in Table 3. Tables 7 through 12 list the measured frequency at which each shorted line was resonant. The determined number of guide half-wavelengths on the line was then taken as that integral value closest to the theoretically calculated number. This was then verified by measuring the number of guide half-wavelengths on the line with the metal probe on a moving carriage. The corresponding phase constant at each resonant frequency was then obtained from Table 6.

Table 7. Frequency, n, and β for the .055" Alumina Substrate with a w/b = 2

f (GHz)	n	β (rad/cm)
2.208	3	1.24
2.931	4	1.65
3.631	5	2.06
4.348	6	2.48
5.040	7	2.89
5.725	8	3.30
6.400	9	3.71
7.080	10	4.12
7.753	11	4.54
9.055	13	5.36
9.710	14	5.77
10.358	15	6.18

Table 8. Frequency, n, and β for the .055" Alumina Substrate with a w/b = 1

f (GHz)	n	β (rad/cm)
2.293	3	1.24
3.050	4	1.65
3.775	5	2.06
4.506	6	2.48
5.224	7	2.89
5.937	8	3.30
6.644	9	3.71
8.738	12	4.95
9.405	13	5.36
10.090	14	5.77

Table 9. Frequency, n, and β for the .025" Alumina Substrate with a w/b = 2

f (GHz)	n	β (rad/cm)
2.236	3	1.24
2.970	4	1.65
3.700	5	2.06
4.420	6	2.48
5.142	7	2.89
5.858	8	3.30
6.568	9	3.71
9.380	13	5.36
10.090	14	5.77

Table 10. Frequency, n, and β for the .025" Alumina Substrate with a w/b = 1

f (GHz)	n	β (rad/cm)
2.318	3	1.24
3.081	4	1.65
3.839	5	2.06
4.594	6	2.48
5.344	7	2.89
6.092	8	3.30
6.834	9	3.71
8.475	11	4.54
9.045	12	4.95
9.718	13	5.36

Table 11. Frequency, n, and β for the .055" D-16 Substrate with a w/b = 2

f (GHz)	n	β (rad/cm)
2.298	4	1.65
2.858	5	2.06
3.402	6	2.48
4.468	8	3.30
4.992	9	3.71
5.520	10	4.12
7.065	13	5.36
7.580	14	5.77
8.585	16	6.60
9.090	17	7.01
9.772	18	7.42

Table 12. Frequency, n, and β for the .055" D-16 Substrate with a w/b = 0.6

f (GHz)	n	β (rad/cm)
2.450	4	1.65
3.048	5	2.06
3.640	6	2.48
4.203	7	2.89
4.775	8	3.30
5.342	9	3.71
5.904	10	4.12
6.465	11	4.54
7.015	12	4.95
7.564	13	5.36
8.640	15	6.18
9.170	16	6.60
9.720	17	7.01

The oscilloscope display of two sets of these transmission resonances was photographed with a Polaroid camera and is shown in Figure 40. The first photograph shows the transmission resonances obtained for a .055" alumina substrate with a w/b = 2. The frequency range of the microwave sweep generator was between approximately four and eight gigahertz. The output power of the generator and the coupling coefficient at resonance was not constant over the swept frequency range. This accounts for the variation in the transmitted RF energy. The second photograph shows the transmission resonances for a .055" D-16 substrate with a w/b = 0.6. The frequency was again swept between about four and eight GHz.

Experimental and Theoretical Comparisons

The experimental results tabulated in Tables 7 through 12 are plotted as frequency versus phase constant curves in Figures 41 through 46. Also plotted in Figures 41 through 45 are the theoretically predicted f-β curves for comparison. The theoretical curves for the w/b = 2 ratios are generally in better agreement with the experimental curves than are the curves for the w/b = 1 ratios. This was expected since the w/b = 1 configurations required unequal spacing between the bottom two rows of nodes in order to achieve the w/b = 1 ratio with 147 nodes whereas the w/b = 2 configurations were modeled with equally spaced nodes. As was pointed out in the section on error analysis in Chapter II, the unequal spacing finite-difference equation had an error of $O(h)$ whereas the equally spaced equation had an error of $O(h^2)$. Consequently the solutions of the finite-difference equations for unequal spacing of the nodes are less accurate than the solutions obtained for an equal spacing of nodes. Figure 41 also contains the f-β curves for the

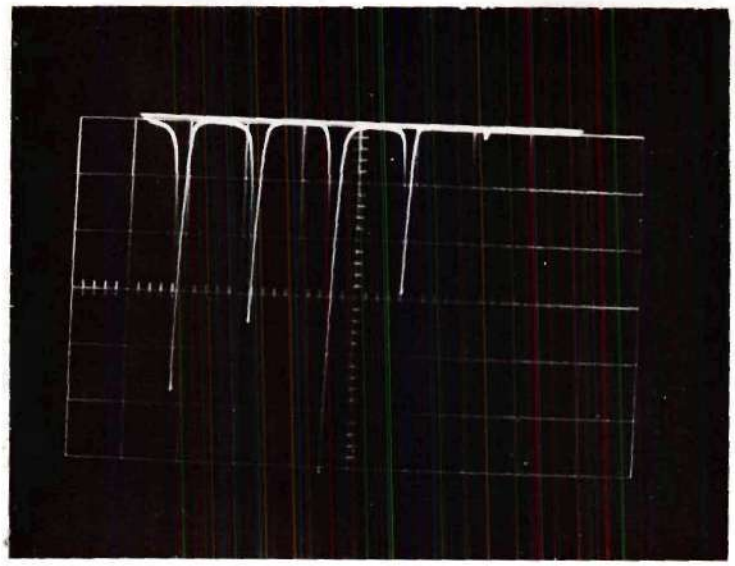

(a) .055" Alumina Substrate with w/b = 2
for a Swept Frequency of 4 to 8 GHz

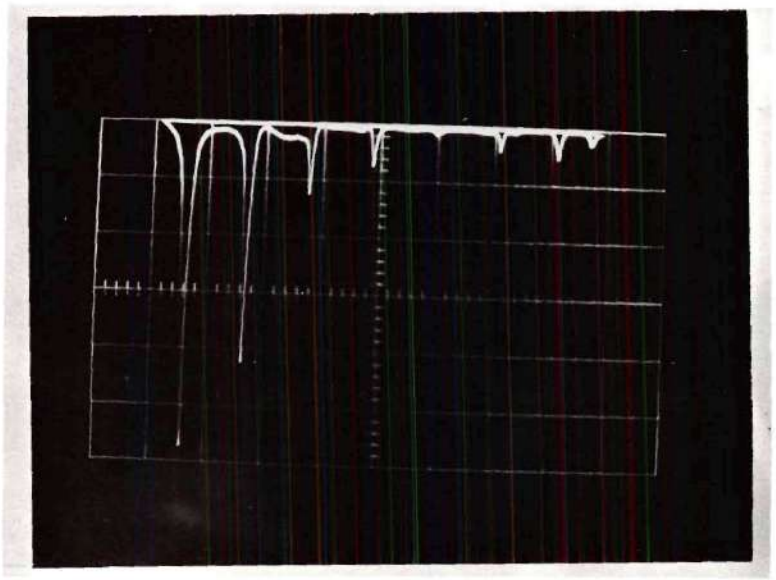

(b) .055" D-16 Substrate with w/b = 0.6
for a Swept Frequency of 4 to 8 GHz

Figure 40. Photographs of the Loosely Coupled Transmission Resonances

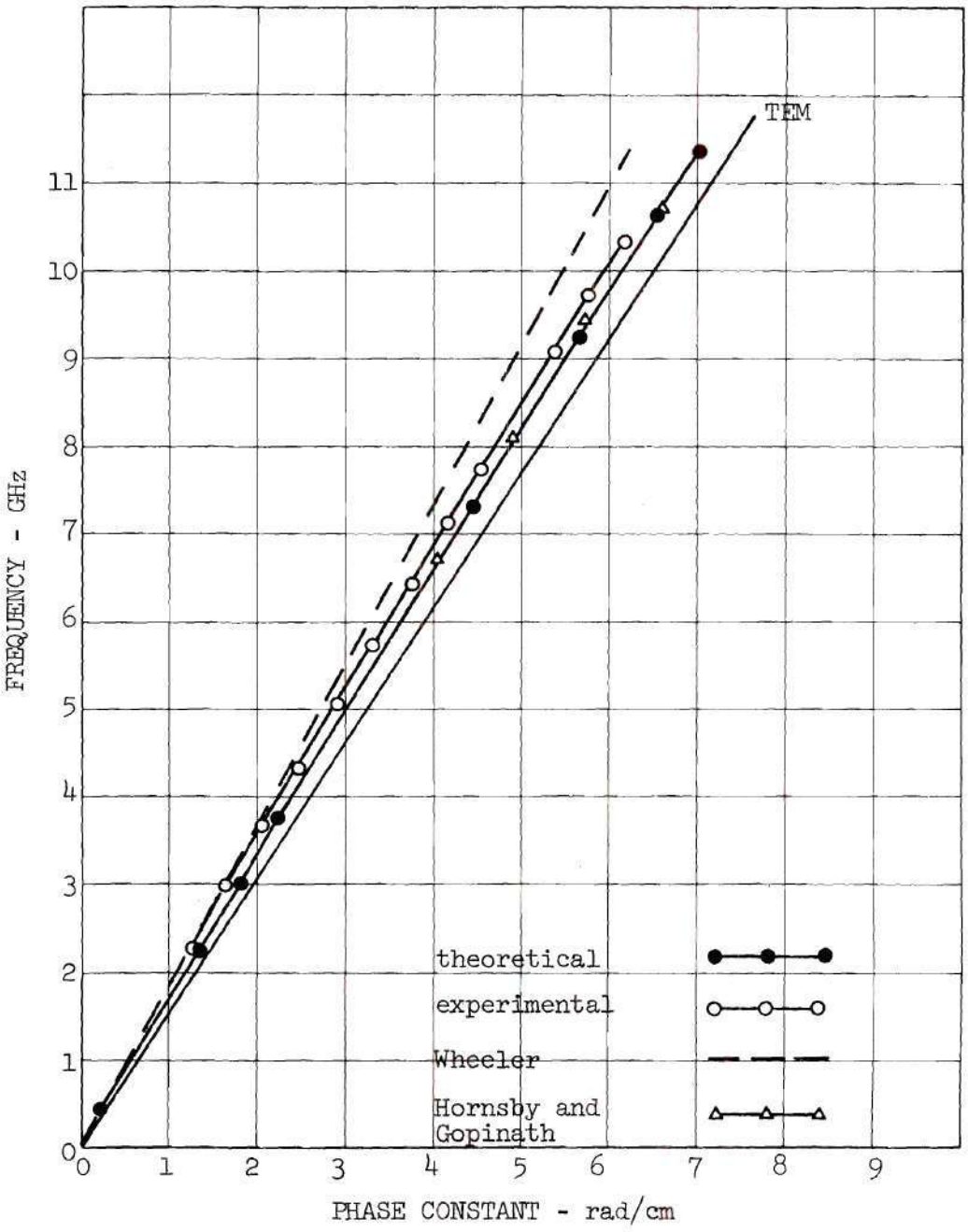

Figure 41. Experimental and Theoretical f-β Diagrams for the .055" Alumina Substrate with w/b = 2

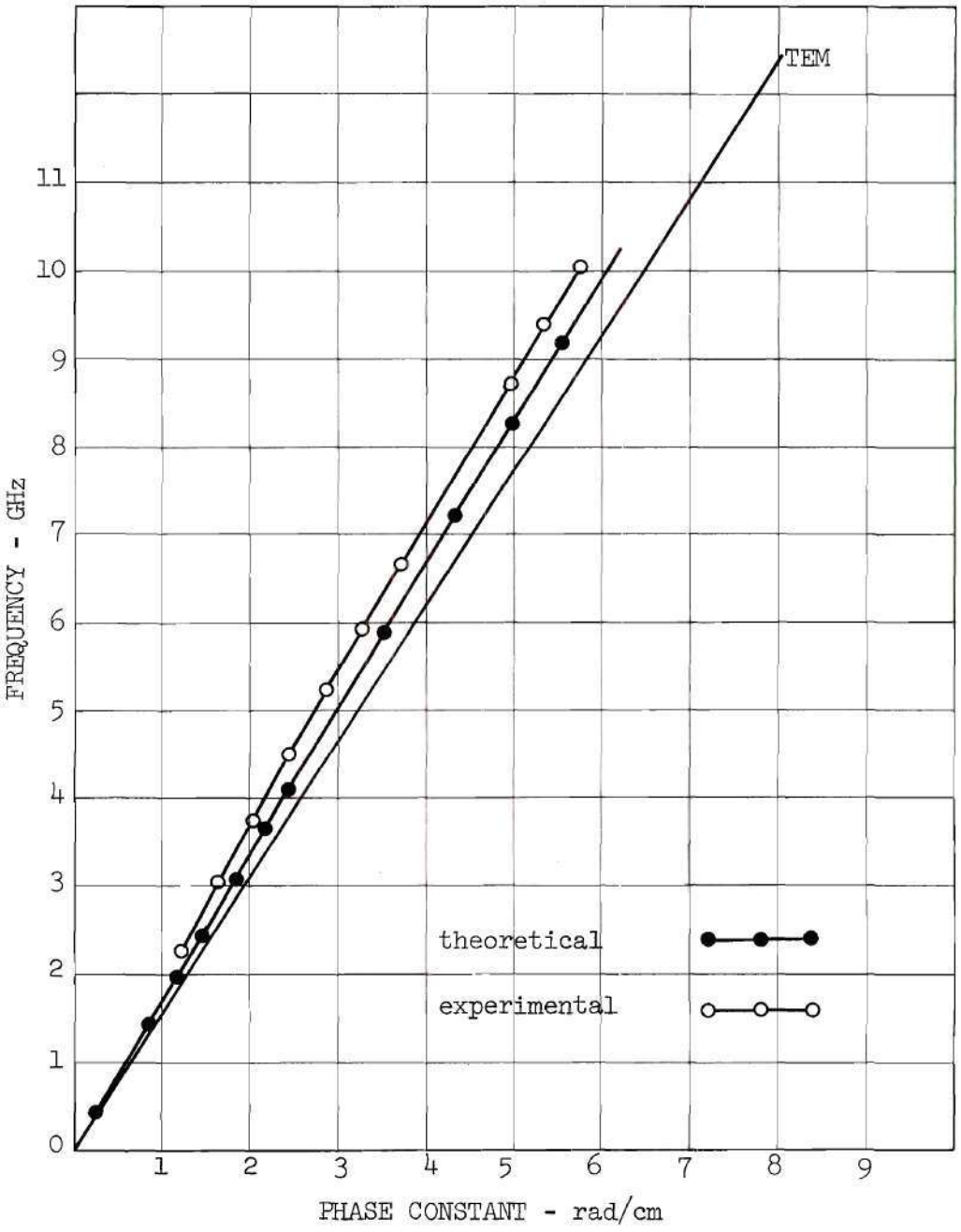

Figure 42. Experimental and Theoretical f-β Diagrams for the .055" Alumina Substrate with w/b = 1

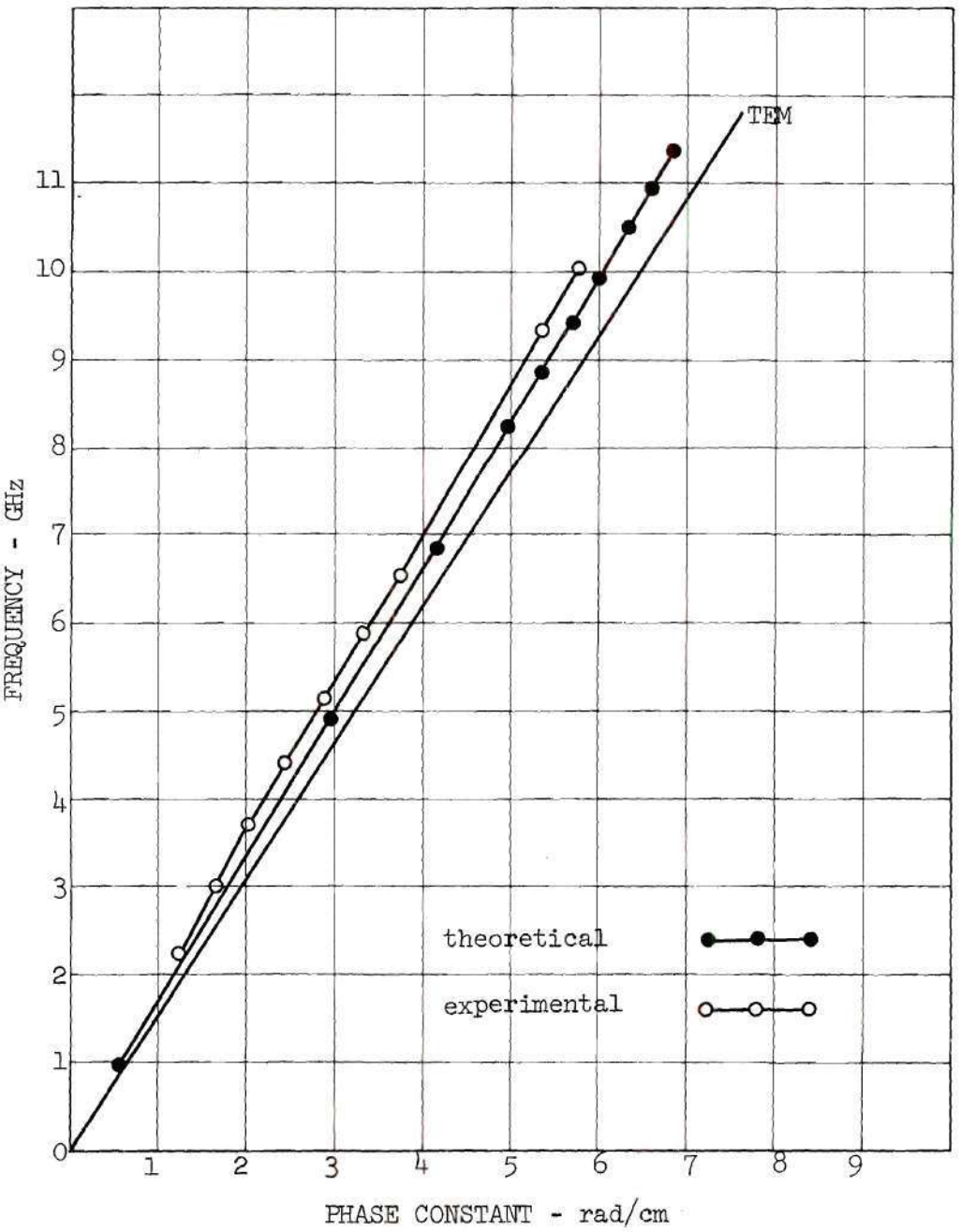

Figure 43. Experimental and Theoretical f-β Diagrams for the .025" Alumina Substrate with w/b = 2

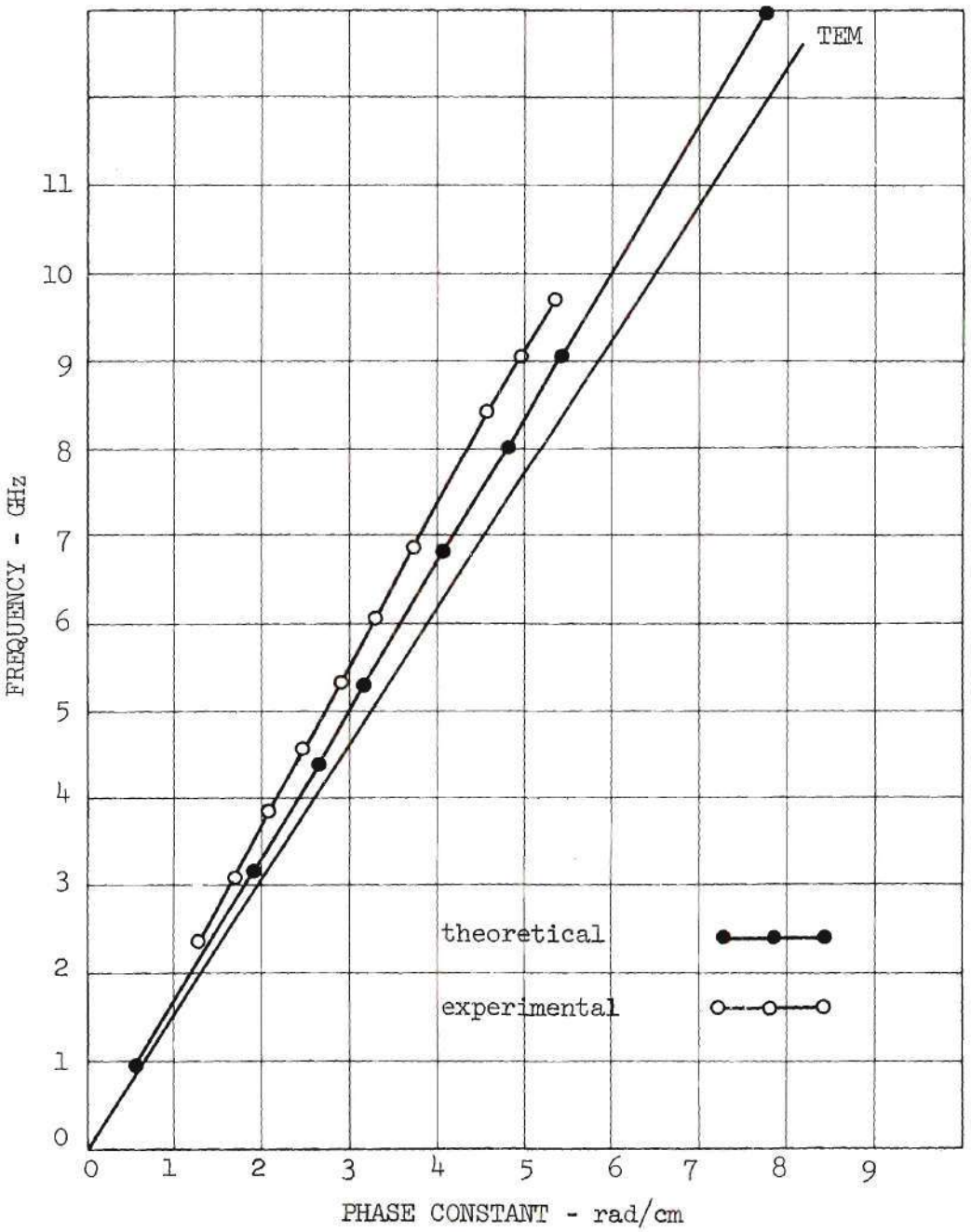

Figure 44. Experimental and Theoretical f-β Diagrams for the .025" Alumina Substrate with w/b = 1

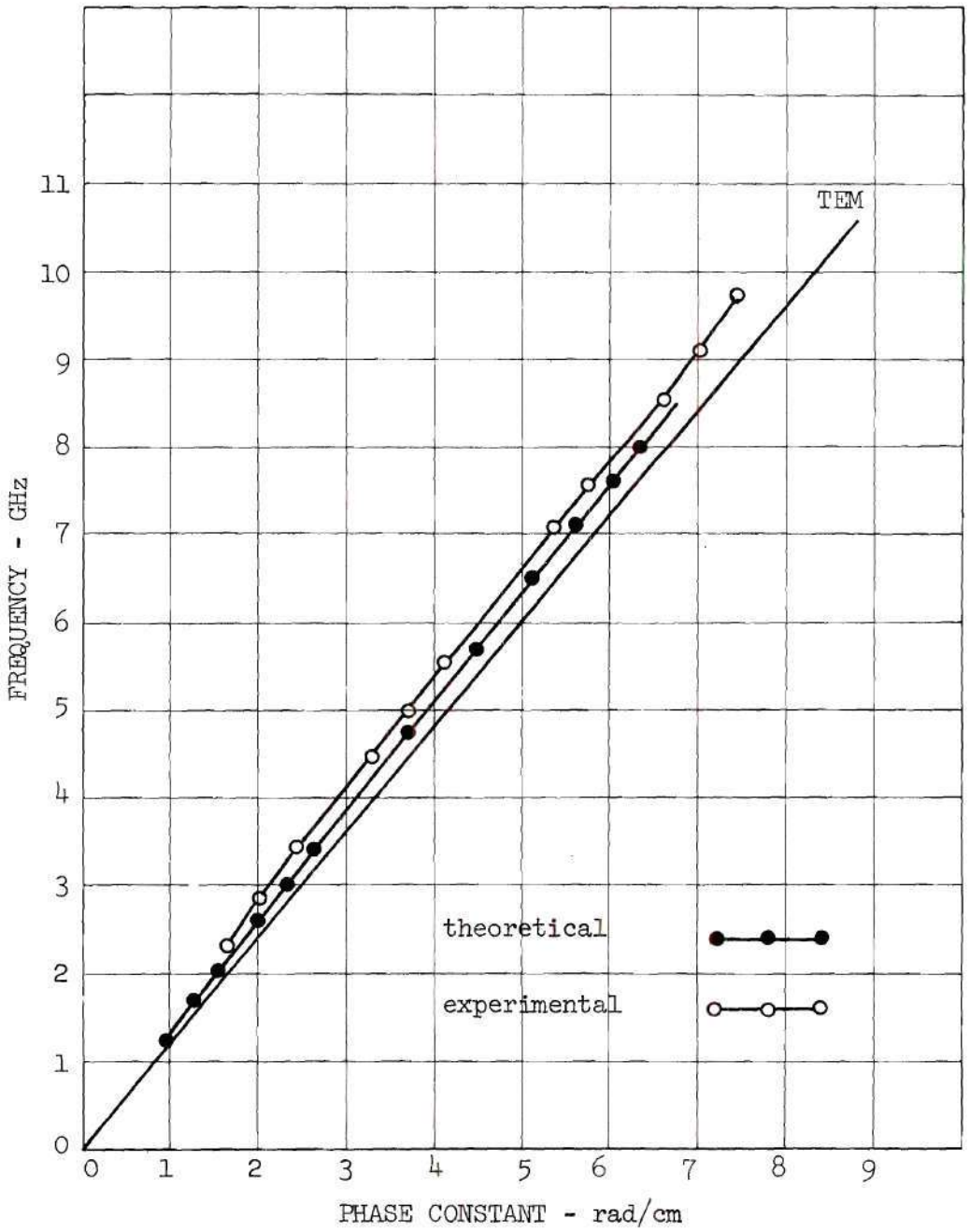

Figure 45. Experimental and Theoretical f-β Diagrams for the .055" D-16 Substrate with w/b = 2

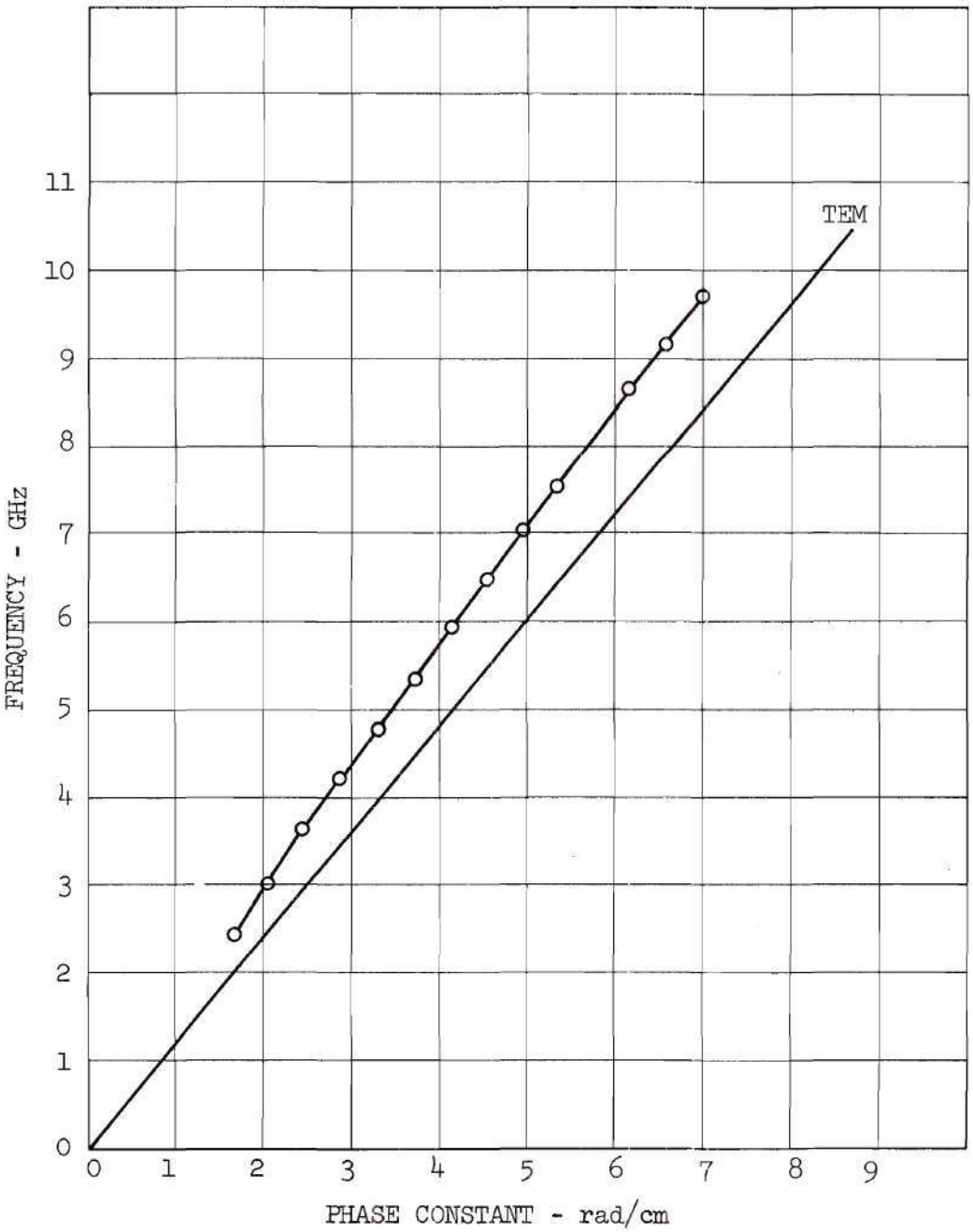

Figure 46. Experimental f-β Diagram for the .055" Alumina Substrate with w/b = 0.6

quasi-TEM mode of Wheeler[13] and the waveguide enclosed microstrip mode of Hornsby and Gopinath,[22] both of which are discussed later in this chapter.

Note that, in the microwave frequency region, all the experimental curves exhibit the normal dispersion which was predicted by the theoretical analysis.

Other Microstrip Modes

In addition to the mode selected as the dominant microstrip mode, other mathematical modes appeared in the set of numerical solutions. If these other mathematical modes had existed physically then, because of their zero cutoff frequency, they should have been excited. Transmission resonances for each of the higher order modes and the lowest order mode then should have appeared in the photographs of Figure 40, but they did not appear. At this time, these other mathematical modes cannot be associated with any known experimentally measured mode. Thus no physical interpretation is presently available.

By comparing Figure 16 with Figure 41, it is seen that the f-β curve for the lowest order mathematical mode is displaced to the right of the second lowest mode (the dominant microstrip mode) by a small amount and is thus further from the experimental f-β curve.

Ferromagnetic Spin Resonance Absorption Results

The ferromagnetic spin resonance absorption experiment was set up according to the block diagram of Figure 38 and performed according to the experimental procedures outlined in Chapter IV. The magnetic field components were calculated from the measured spin resonance absorptions

on three of the microstrip lines: the .055" and .025" alumina lines with w/b = 2 and the .055" D-16 line with w/b = 0.6.

VSWR Measurements

VSWR versus frequency measurements for these three lines which were computed on the Hewlett-Packard network analyzer are plotted in Figure 47.

The variation in VSWR as a function of the frequency was due to the phasing of the reflected waves from the connector mismatches. These results indicated that each line would have to be matched using the two double stub tuners before meaningful resonance absorption measurements could be taken. Had a matching procedure not been used, the large reflected wave on the microstrip line would have added to the forward propagating wave. Subsequently, the fields calculated from the measured spin resonance absorptions would then have been a resultant of the forward and reverse propagating waves. This would have led to an erroneous mode pattern.

Experimental and Theoretical Results for the .055" Alumina Substrate with w/b = 2

The spin resonance absorption measurements were made on the .055" alumina substrate with a center strip width of .110" (having a characteristic impedance of 33 ohms) at a frequency of 10.6 GHz. The measured uniform mode spin resonance absorption peaks are presented in Table 13 as a function of the YIG sphere positions, normalized to half the center strip width W, in the vicinity of the center strip. Also listed are the relative power absorbed and the calculated magnetic field components.

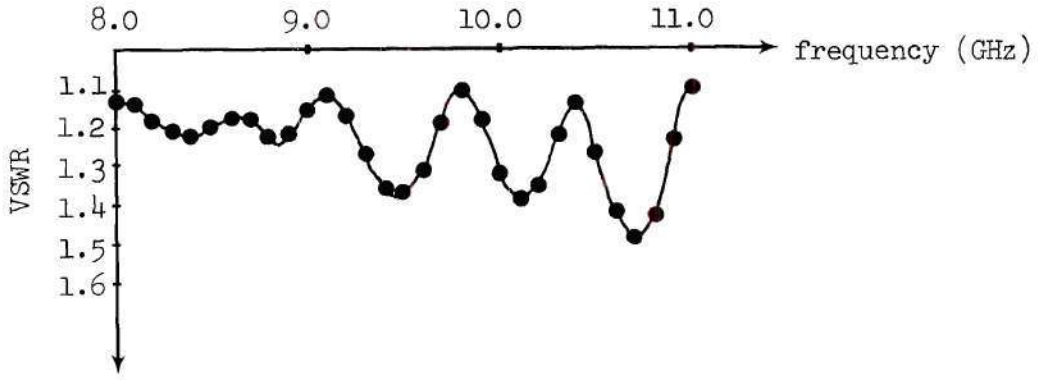

(a) .055" Alumina Substrate with w/b = 2

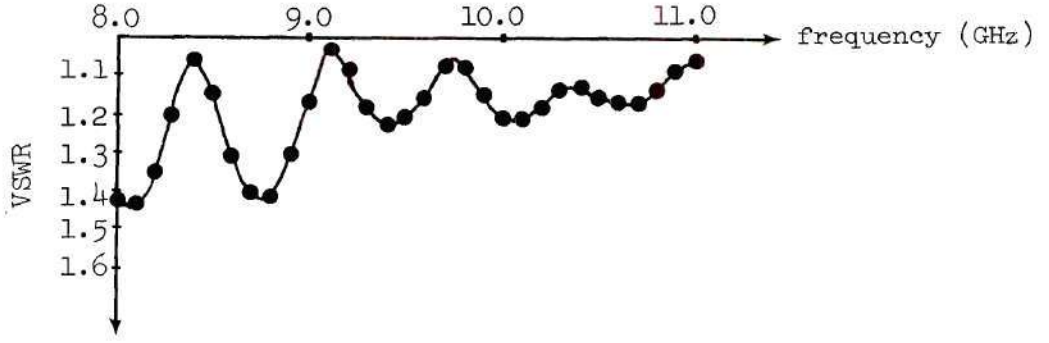

(b) .025" Alumina Substrate with w/b = 2

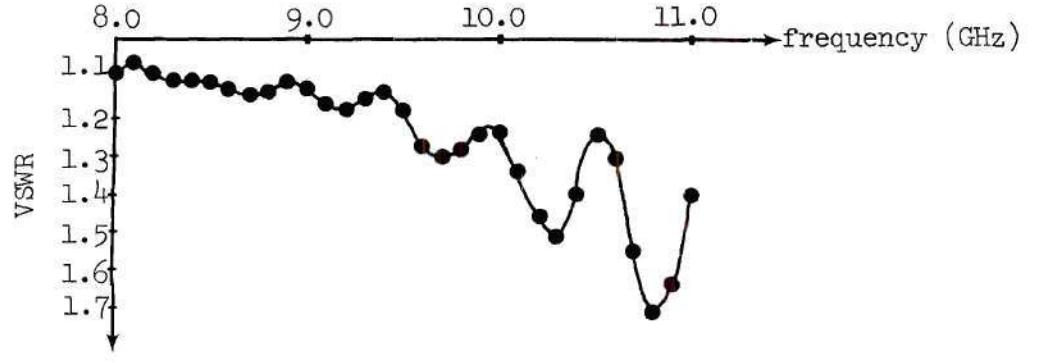

(c) .055" D-16 Substrate with w/b = 0.6

Figure 47. VSWR versus Frequency for Three Microstrip Lines

Table 13. Measured Resonance Absorptions and the Calculated Magnetic Field Components for the .055" Alumina Substrate with w/b = 2

x/W	Orientation of the DC Field	Measured Absorption (dB)	Power Absorbed	Relative Magnetic Field
0.010	-y	0.08	0.017	h_x = 0.261
	+y	0.08	0.017	h^x = 0.0
	-x	0.0	0.0	h^z = 0.0
	+x	0.0	0.0	h^y_z = 0.0
0.254	-y	0.08	0.017	h_x = 0.258
	+y	0.11	0.024	h^x = 0.024
	-x	0.0	0.0	h^z = 0.0
	+x	0.0	0.0	h^y_z = 0.0
0.455	-y	0.0	0.0	h_y = 0.407
	+y	0.24	0.053	h^y = 0.091
	-x	0.0	0.0	h^z = -0.032
	+x	0.01	0.001	h^y_z = 0.032
0.600	-y	0.15	0.033	h_x = 0.468
	+y	0.38	0.083	h^x = 0.108
	-x	0.0	0.0	h^z = -0.161
	+x	0.12	0.026	h^y_z = 0.161
0.828	-y	0.35	0.076	h_x = 0.468
	+y	1.40	0.275	h^x = 0.248
	-x	0.05	0.01	h^z = -0.428
	+x	0.50	0.108	h^y_z = 0.228
1.020	-y	0.04	0.019	h_x = 0.256
	+y	0.73	0.155	h^x = 0.532
	-x	0.46	0.099	h^z = -0.888
	+x	1.73	0.328	h^y_z = 0.258
1.400	-y	1.82	0.342	h_x = -0.585
	+y	0.0	0.0	h^x = 0.585
	-x	0.23	0.050	h^z = -0.957
	+x	3.35	0.538	h^y_z = 0.509
1.945	-y	0.75	0.158	h_x = -0.397
	+y	0.0	0.0	h^x = 0.397
	-x	0.0	0.0	h^z = -0.349
	+x	0.57	0.122	h^y_z = 0.349

A complete listing of the measured resonance absorptions, including both uniform and nonuniform modes is presented in Appendix C.

The magnetic field components which were calculated from the spin resonance absorption data are plotted in Figure 48. Note that two H_z curves are plotted, one for each of the two antiparallel orientations of $\vec{H}_o$. Also shown in the figure is a cross sectional view of the microstrip drawn to approximate scale. The large dot represents the size of the YIG sphere relative to the microstrip line. The triangles on the plot indicate the regions on the substrate where the nonuniform modes perturbed the uniform mode of resonance absorption. At those regions coupling to nonuniform modes resulted in a broadening of the resonance line of the principal mode of resonance absorption and consequently a reduction in the peak of the resonance absorption curve. The fields calculated at these locations are based on the resonances which were judged to be the uniform mode but which were probably reduced in amplitude due to the coupling to nonuniform modes.

The theoretically calculated magnetic field components are presented for comparison in Figures 49 and 50. Since the YIG sphere diameter was approximately equal to the node spacing for the .055" substrate, the plotted fields are averages of the field values at the nodes on the interface and the field values at the nodes just above the interface. Comparison of the experimental and theoretical curves in the vicinity of the center strip shows very good agreement. The longitudinal magnetic field reaches its maximum just past the center strip edge. The x-component of the magnetic field reaches its positive extremum just inside the center

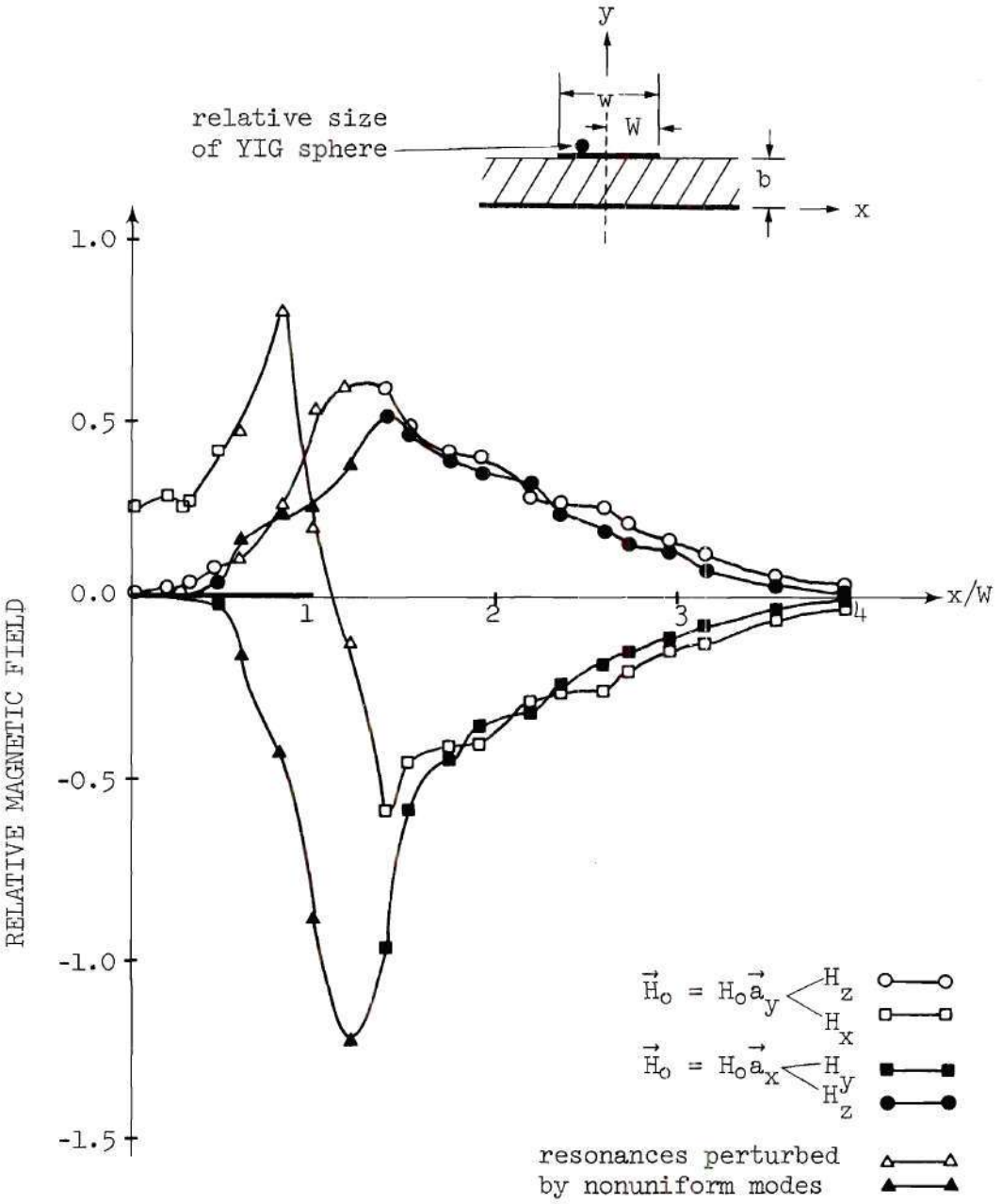

Figure 48. Magnetic Field Components Calculated from the Measured Spin Resonance Absorptions for the .055" Alumina Substrate with w/b = 2 at 10.6 GHz

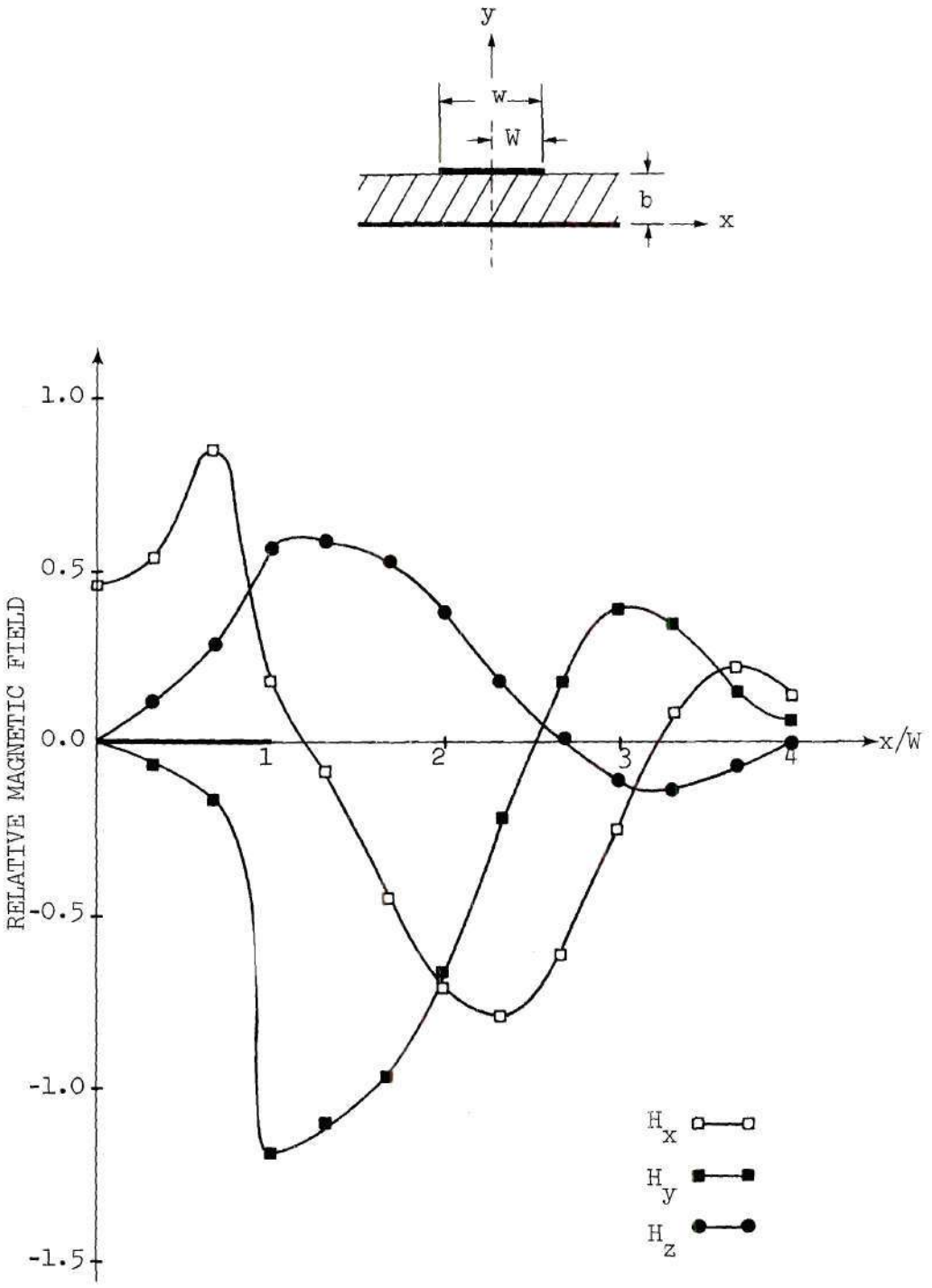

Figure 49. Relative Amplitudes of the Numerically Calculated Magnetic Field Components for the .055" Alumina Substrate with w/b = 2 at 10.62 GHz

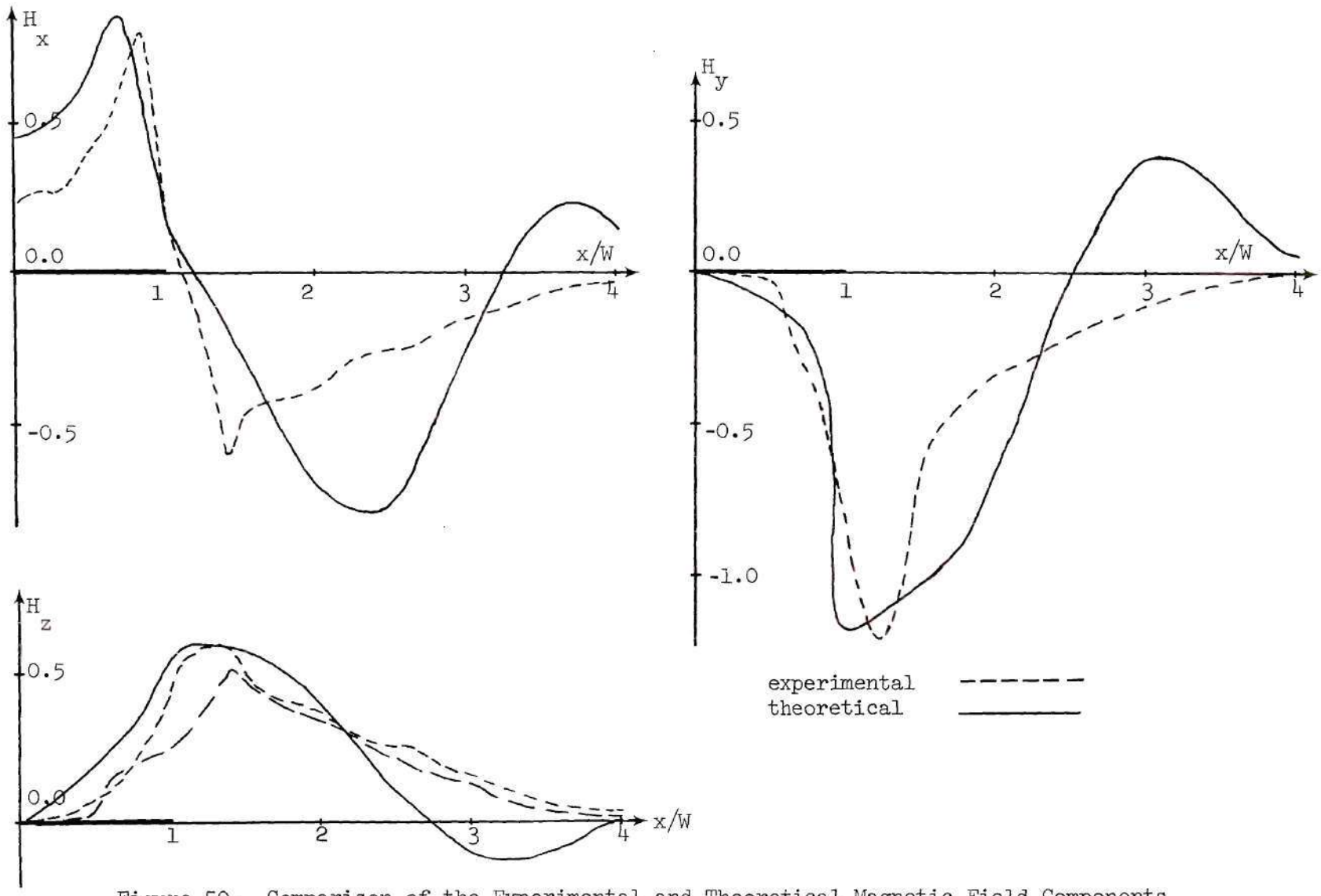

Figure 50. Comparison of the Experimental and Theoretical Magnetic Field Components for the .055" Alumina Substrate with w/b = 2

strip edge, passes through zero just past the edge and then passes through a negative extremum a short distance from the edge. The y-component of the magnetic field drops off from zero in the vicinity of the center strip down to a negative maximum just past the center strip edge. Note that the longitudinal magnetic field and consequently the longitudinal electric field of the microstrip mode along the interface is far from being a negligible quantity.

Further away from the center strip, the accuracy of the measurement decreases rather rapidly for reasons associated with the experimental technique. The power absorbed by the YIG sphere probe was effectively normalized to a maximum value of unity. The RF magnetic field was then calculated from the square root of the power absorbed by the sphere, and two was the maximum value that these calculated fields could attain. Thus for a relatively large range of absorptions measured in dB, from zero to a large value, the resulting calculated fields cover a relatively small range, from zero to a maximum of two.

At regions on the air-dielectric interface in the vicinity of the center strip edge, both the experimental plot, Figure 48, and the theoretical plot, Figure 49, reveal a relatively large component of circularly polarized RF magnetic field in planes normal to both the x- and y-axes. Experimental work by other investigators[†] had indicated that there was a circularly polarized component of the RF magnetic field in microstrip, but its relative location and amplitude were not known.

[†]Private communication with D. R. Taft, Sperry Microwave Electronics Company, Clearwater, Florida.

This research substantiates its existence and provides information vital to the design of microstrip components which make use of this particular field configuration. For example, a nonreciprocal resonance isolator could be easily constructed by surface loading the microstrip line with a piece of ferrimagnetic material properly biased for the frequency of operation.

The fact that there is a substantial component of longitudinal magnetic field has been demonstrated both experimentally and theoretically. It should be pointed out, however, that most of the energy in the microstrip mode is concentrated in the dielectric substrate under the center strip and in this region the longitudinal fields are relatively weak. Consequently, one would expect TEM calculations of guide wavelength, phase constant, etc. to be reasonably close to the actual values. This is shown by comparing the calculations in this research with calculated TEM values.

Experimental and Theoretical Results for the .025" Alumina Substrate with w/b = 2

The resonance absorption measurements were made on a .025" alumina substrate with a center strip width of .050" (having a characteristic impedance of 33 ohms) at a frequency of 10.8 GHz. The measured uniform mode resonance absorptions and calculated data in the vicinity of the center strip are listed in Table 14. A complete listing of uniform and nonuniform resonance absorptions and calculated field components are listed in Appendix C.

Table 14. Measured Resonance Absorptions and the Calculated Magnetic Field Components for the .025" Alumina Substrate with w/b = 2

x/W	Orientation of the DC Field	Measured Absorption (dB)	Power Absorbed	Relative Magnetic Field
0.00	-y	2.15	0.39	$h_x = 1.248$
	+y	2.15	0.39	$h_z = 0.0$
	-x	0.0	0.0	$h_y = 0.0$
	+x	0.0	0.0	
0.300	-y	1.40	0.275	$h_x = 1.165$
	+y	2.30	0.41	$h_z = 0.116$
	-x	0.0	0.0	$h_y = -0.21$
	+x	0.20	0.044	
0.860	-y	0.62	0.132	$h_x = 1.081$
	+y	3.15	0.515	$h_z = 0.355$
	-x	0.80	0.167	$h_y = -1.245$
	+x	5.20	0.698	
1.220	-y	0.42	0.092	$h_x = 0.913$
	+y	2.00	0.368	$h_z = 0.301$
	-x	2.70	0.463	$h_y = -1.670$
	+x	16.80	0.979	
1.640	-y	3.30	0.532	$h_x = -0.785$
	+y	0.02	0.003	$h_z = 0.675$
	-x	1.48	0.288	$h_y = -1.523$
	+x	15.80	0.974	
2.040	-y	2.8	0.475	$h_x = -0.721$
	+y	0.01	0.001	$h_z = 0.658$
	-x	0.48	0.103	$h_y = -1.258$
	+x	9.10	0.877	

The magnetic field components which were calculated from the measured spin resonance absorptions are plotted in Figure 51. Also drawn to relative scale is a cross sectional view of the microstrip and YIG sphere. As before the triangles indicate the excitation of nonuniform absorption modes.

The same .0164" diameter YIG sphere that was used in measuring the fields of the .055" alumina line was used in this set of measurements. The relative size of the YIG sphere when compared with the size of the microstrip had increased for this portion of the experiment. Thus the presence of the high dielectric constant YIG sphere ($K = 16$) perturbed the propagating fields to a much larger degree than that experienced in the previous experiment. This perturbation could have been reduced if a smaller single crystal YIG sphere had been used. However, the .0164" YIG sphere was the smallest that was available for use in this research.

The theoretically calculated magnetic field components are plotted in Figure 52. The field values plotted are those of the first row of nodes just above the interface since these more closely approximate the center of the YIG sphere. In the vicinity of the center strip, the field components of the experimental and theoretical calculations show fairly good agreement. Away from the center strip the accuracy decreases rather quickly for the same reasons previously discussed. Also, the assumption that the high dielectric constant YIG sphere can be treated only as a perturbation becomes less accurate, particularly as the sphere is moved away from the center strip. This is because the sphere does not perturb

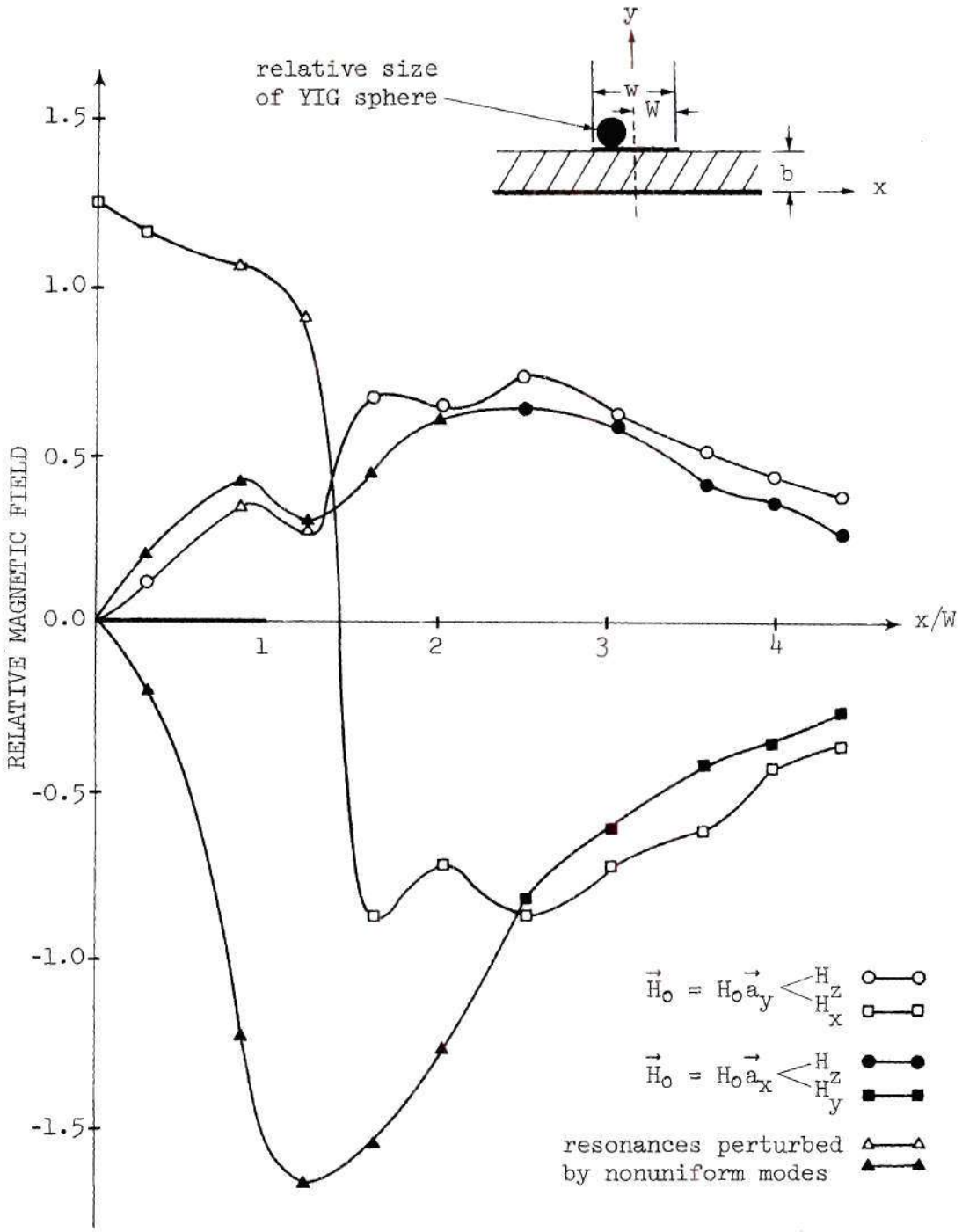

Figure 51. Magnetic Field Components Calculated from the Measured Spin Resonance Absorptions for the .025" Alumina Substrate with w/b = 2 at 10.8 GHz

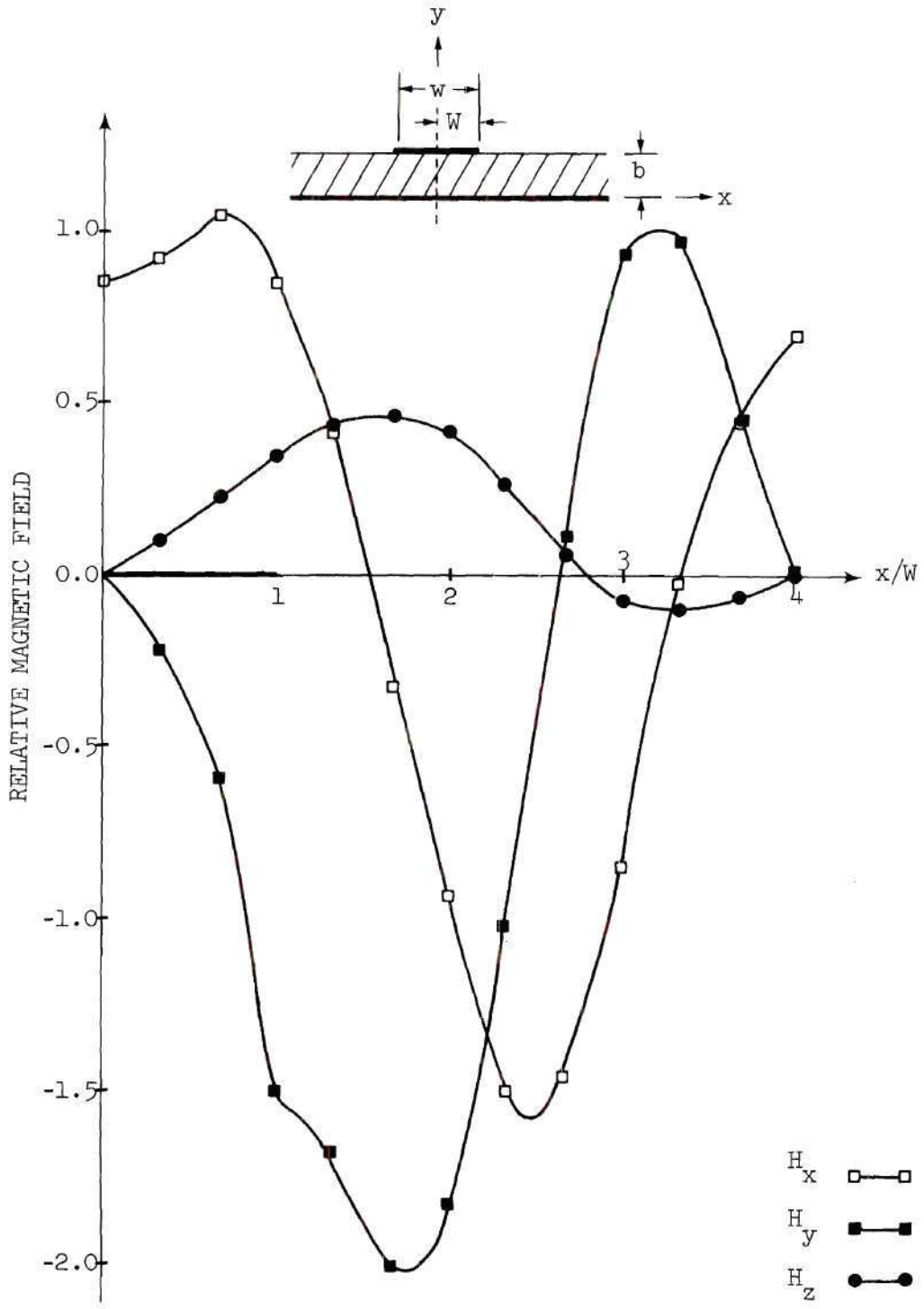

Figure 52. Relative Amplitudes of the Numerically Calculated Magnetic Field Components for the .025" Alumina Substrate with w/b = 2 at 10.94 GHz

the mode pattern appreciably when it is over the center strip. But when the YIG sphere is on the air-dielectric interface away from the center strip, it behaves like a field displacement device and thus perturbs the mode pattern.

Experimental Results for the .055" D-16 Substrate with w/b = 0.6

The final set of measurements were taken on a .055" D-16 substrate with a .033" center strip having a 50 ohm characteristic impedance and at a frequency of 8.1 GHz. A partial listing of the measured uniform mode absorptions and calculated fields is shown in Table 15, and the complete listing is included in Appendix C. Figure 53 shows the calculated fields and the locations where the nonuniform Walker modes perturbed the principal uniform mode of resonance absorption. Note the relatively large size of the sphere as compared with the microstrip center strip width. In the vicinity of the center strip, the fields still show the same relative shape predicted by the earlier measurements and calculations, despite the presence of such a large perturbing probe. There were no theoretical calculations made for this particular set of measurements because the narrow center strip could not be accurately represented by the nodal arrangement.

Relative Accuracy of the Experimental Results

Of the three spin resonance absorption experiments, the .055" alumina substrate with the .110" center strip was the most accurate since the probing sphere was the smallest when compared with the microstrip dimensions. It was interesting to note that, despite the increasingly large perturbation presented by the YIG sphere probe in the sequence of experiments, the resulting determined fields in the vicinity of the

Table 15. Measured Resonance Absorptions and the Calculated Magnetic Field Components for the .055" D-16 Substrate with w/b = 0.6

x/W	Orientation of the DC Field	Measured Absorption (dB)	Power Absorbed	Relative Magnetic Field
0.000	-y	3.20	0.521	$h_x = 1.434$
	+y	3.20	0.521	$h_z = 0.0$
	-x	0.0	0.0	$h_y = 0.0$
	+x	0.0	0.0	$h_z = 0.0$
0.455	-y	3.50	0.553	$h_x = 1.566$
	+y	4.75	0.665	$h_z = 0.08$
	-x	0.49	0.105	$h_y = 0.816$
	+x	1.21	0.242	$h_z = 0.068$
1.240	-y	0.87	0.18	$h_x = 1.319$
	+y	7.00	0.80	$h_z = 0.471$
	-x	3.78	0.543	$h_y = -1.704$
	+x	12.00	0.937	$h_z = 0.232$
2.000	-y	4.10	0.611	$h_x = -0.575$
	+y	0.20	0.043	$h_z = 0.989$
	-x	1.81	0.340	$h_y = -1.572$
	+x	16.70	0.979	$h_z = 0.406$
3.030	-y	5.75	0.734	$h_x = -0.911$
	+y	0.02	0.003	$h_z = 0.801$
	-x	0.86	0.179	$h_y = -1.405$
	+x	14.50	0.965	$h_z = 0.559$

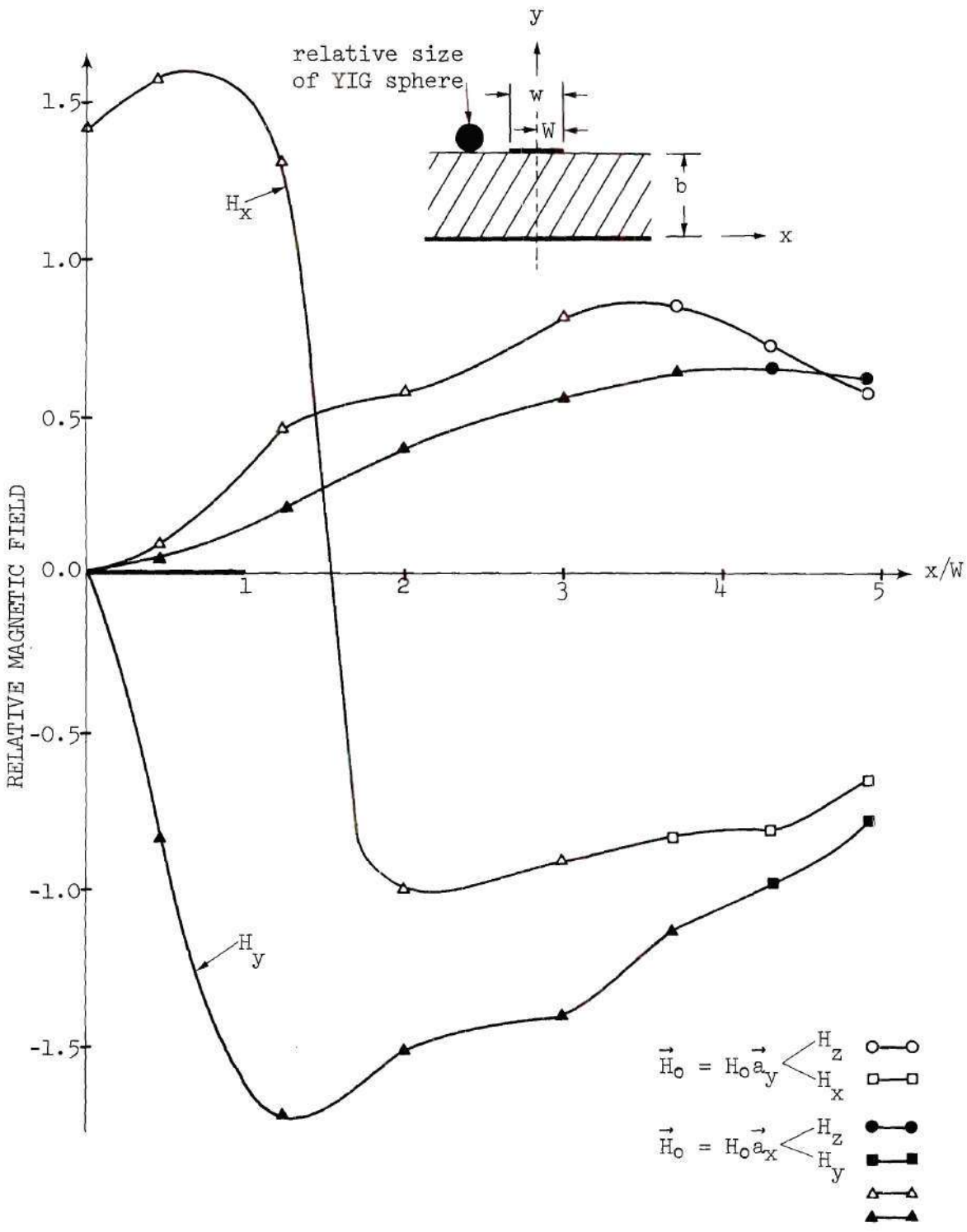

Figure 53. Magnetic Field Components Calculated from the Measured Spin Resonance Absorptions for the .055" D-16 Substrate with w/b = 0.6 at 8.1 GHz

center strip still retained their predicted shape.

A Resonance Absorption

The magnitude of the ferromagnetic spin resonance absorption was measured with an SWR indicator. In order to get a photograph of a resonance absorption, the SHF signal generator was replaced by a microwave sweep generator and the bolometer and SWR indicator were replaced by the crystal detector and oscilloscope. Figure 54 shows the photograph of the detected output with a single uniform mode of resonance absorption

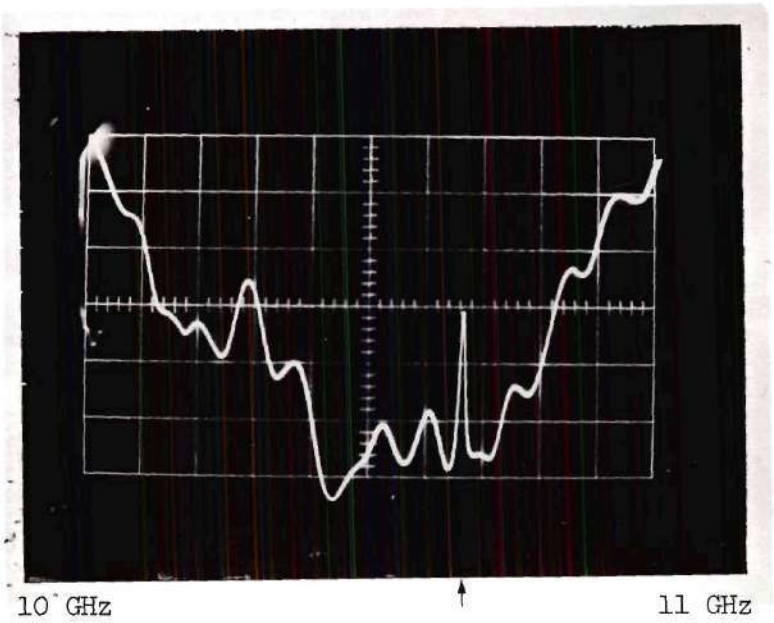

Figure 54. A Uniform Mode Resonance (arrow) on a .055" Alumina Substrate with w/b = 2

on a .055" alumina substrate with w/b = 2. The sweep frequency range on the generator was from 10 to 11 GHz and the DC biasing field was about 3.60 kilogauss. The variations at off resonance were due to the microwave

sweep generator and the mismatches in the system.

Figure 56 shows the principal uniform resonance mode of absorption along with two very small nonuniform modes (Walker modes) of resonance absorption for two different DC biasing fields. The sweep frequency range was between 9.5 and 11.1 GHz for DC biasing fields of about 3.66 kilogauss and 3.70 kilogauss. Note the frequency shift of all the modes.

Comparison with Other Investigator's Calculations

Hornsby and Gopinath[22] modeled the microstrip with an enclosing waveguide and made calculations for a dielectric substrate having $K = 9.0$, $b = .020"$, and $w/b = 2$. In the vicinity of the center strip their calculated fields are similar to those calculated in this work. Their longitudinal magnetic field is displayed in Figure 55.

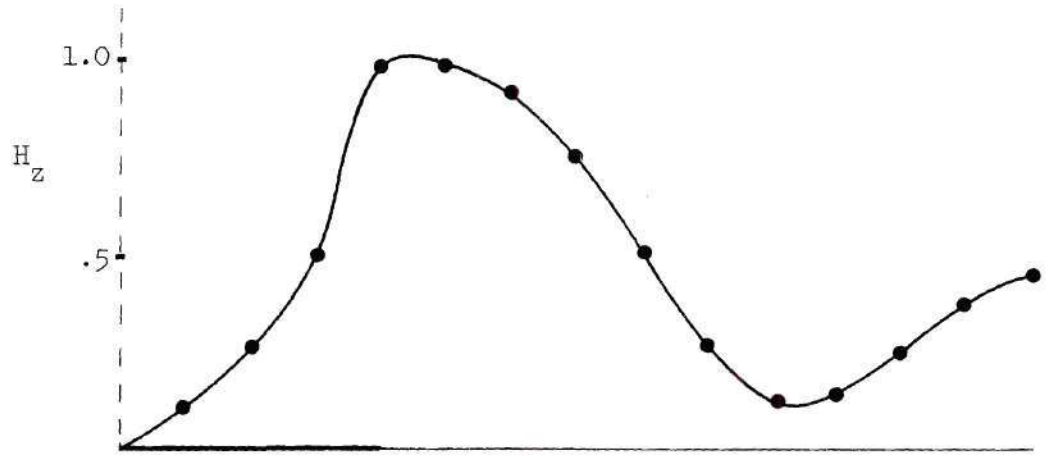

Figure 55. Longitudinal Magnetic Field of a .020" Dielectric Substrate with $K = 9.0$ and $w/b = 2$ of Hornsby and Gopinath

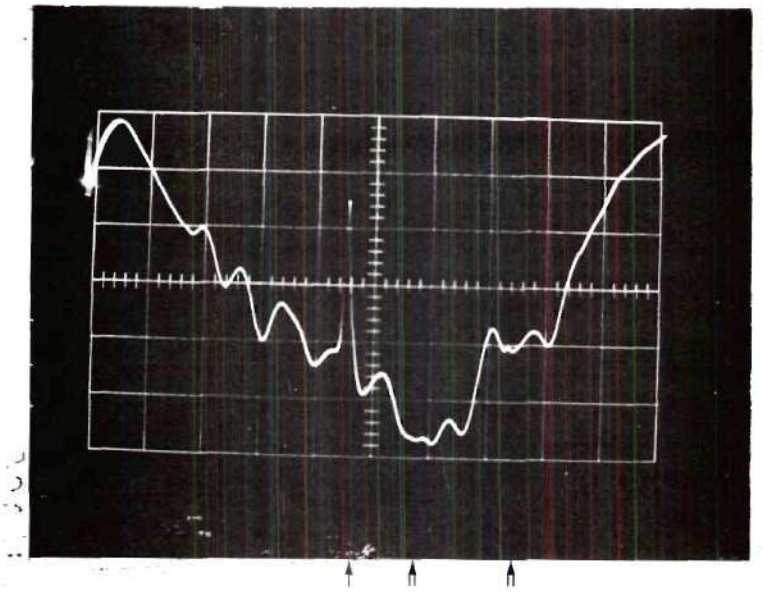

9.5 GHz 11.1 GHz

(a) DC Field of 3.66 kilogauss

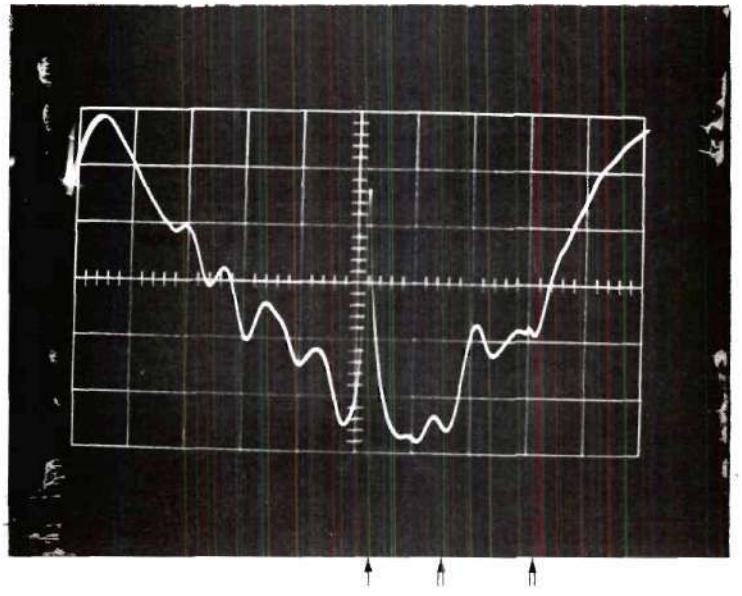

9.5 GHz 11.1 GHz

(b) DC Field of 3.70 kilogauss

Figure 56. A Uniform Mode (arrow) and Two Nonuniform Modes (double arrow) of Resonance Absorption on a .025" Alumina Substrate with w/b = 2 for DC Biasing Fields of 3.66 and 3.70 Kilogauss

Along the air-dielectric interface near the waveguide wall, the magnetic field of their calculation had an erratic behavior which they attributed to the approximate nature of their method.

It is interesting to note that the mode calculated by Hornsby and Gopinath was actually the second lowest mathematical mode. They used a technique which calculated only the eigenvalue of smallest modulus and its corresponding eigenvector. They assumed that the eigenvalues which they calculated belonged to the same mathematical mode. As a check of their work, all the eigenvalues were calculated by the QR transform technique of this work, modified to allow for the perfectly conducting bounding walls. A break in the eigenvalues occurred and a lowest order mathematical mode resulted. However, they did not observe this mathematical mode. Their choices for the parameter T yielded results for the second lowest mode, the mode considered here to be the dominant mode.

The only other experimental investigation for the field configuration was by Shafer.[8] He used a loop coupling technique to measure the average RF magnetic field distribution on an oversized microstrip line having a low dielectric constant substrate. His measured average value of the square of the longitudinal magnetic field along the interface is drawn in Figure 57. This longitudinal magnetic field component is similar to the longitudinal magnetic field component in this work and plotted in Figure 48. It appears that his measured fields experienced the same reversal in sign as did the theoretical calculations here.

Caulton, et al.[14] calculated several sets of curves describing the change in several microstrip parameters as functions of the physical dimensions of the line. In particular, their plot of λ/λ_{TEM} versus w/b

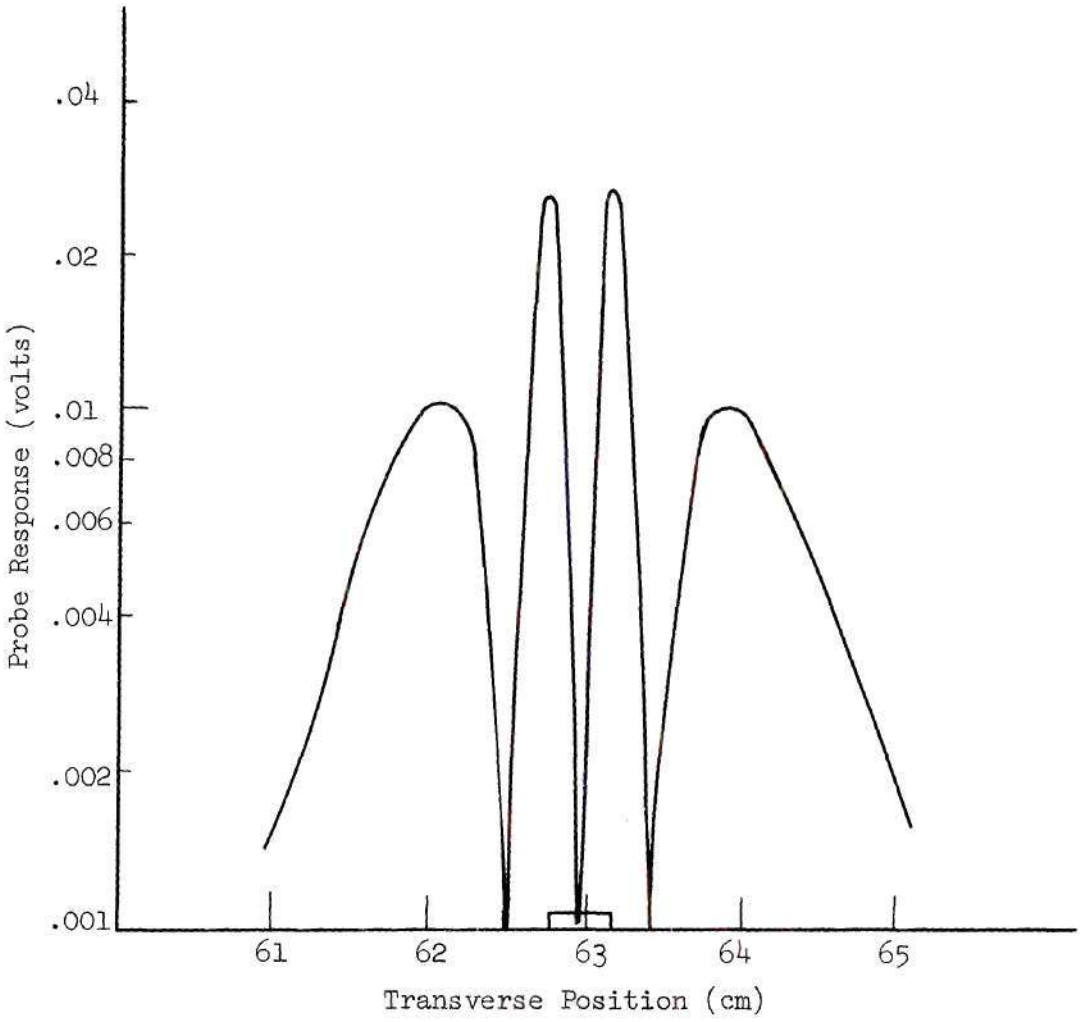

Figure 57. Average Longitudinal Magnetic Field Squared as Measured by Shafer

has been used quite frequently in the microwave industry for determining the guide wavelength for various configurations. That part of their plot for a relative dielectric constant of 9.5 is plotted in Figure 58. It has generally been assumed that the wavelength curve normalized to the wavelength for a TEM wave in a homogeneous dielectric would be accurate over the microwave frequency range. The theoretically and experimentally calculated values plotted in Figure 58 show that the curve prepared by Caulton is accurate only around 2 GHz. The experimental points around S band for the two lines tested fall very close to Caulton's curve, but around X band or higher there is about 15 percent or more error. The theoretical calculations for the $w/b = 1$ configuration had an error of $O(h)$ and are accordingly less accurate than the calculations for the $w/b = 2$ configuration which had an error of $O(h^2)$.

Wheeler's analysis of a quasi-TEM mode leads to a straight line f-β curve as shown for comparison in Figure 41. The curve is characteristic of a TEM mode (zero cutoff frequency), and it is nondispersive. The f-β curve obtained for the waveguide enclosed microstrip of Hornsby and Gopinath fell right along the curve for the zero field walls as is also shown in Figure 41. Thus in Figure 58 the points corresponding to their analysis fell on the points for the zero field wall analysis studied here.

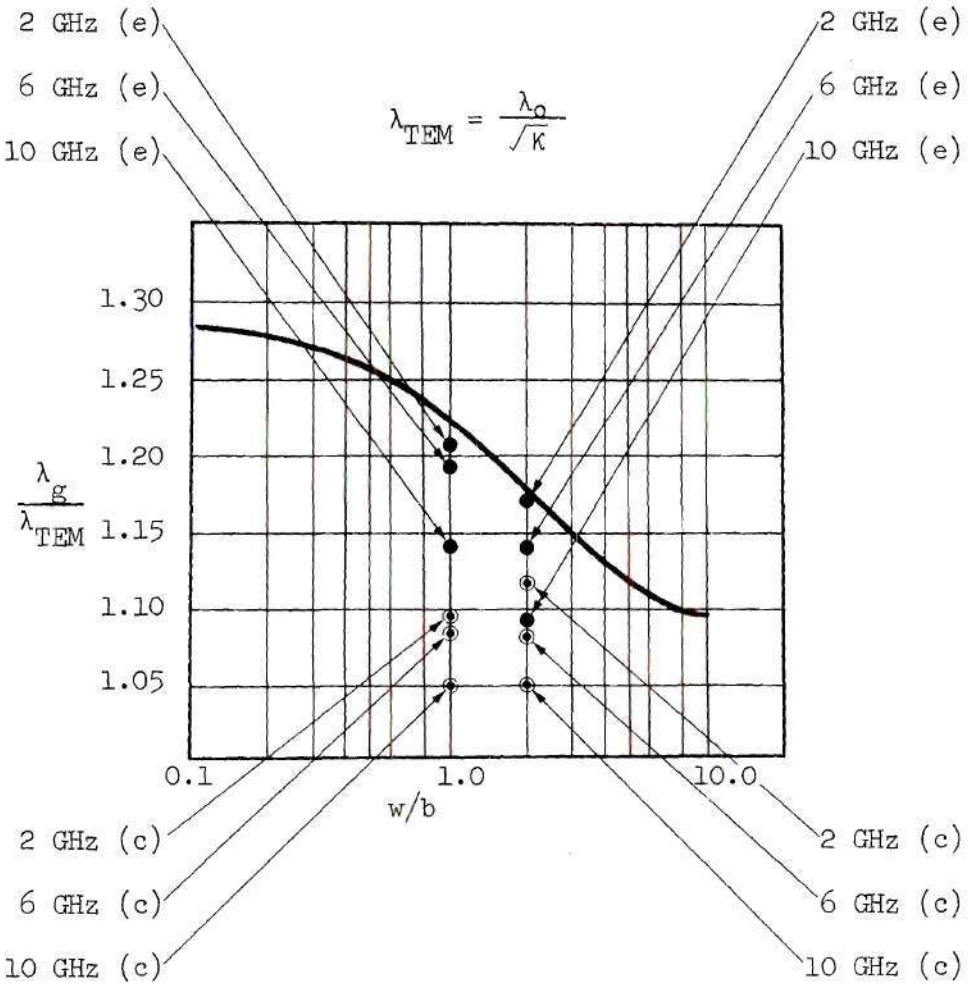

Figure 58. Experimental (e) and Calculated (c) Normalized Wavelength as a Function of w/b for a .025" Alumina Substrate Plotted Against Caulton's Curve for $\kappa = 9.5$

CHAPTER VI

CONCLUSIONS AND RECOMMENDATIONS

Many investigators in the microwave industry have attempted to determine the properties of microstrip and its mode pattern. At the inception of this research, their theoretical analyses for the determination of the field configuration were based on TEM or quasi-TEM assumptions. These assumptions, though not rigorously accurate, had led to usable approximations of the microstrip parameters, such as impedance, guide wavelength, etc. The reason for their success is that most of the energy of the microstrip mode is concentrated under the center strip in the high dielectric constant substrate. In this region the longitudinal fields are weak, and thus an analysis based on purely transverse fields shows reasonably good correlation with the true values. However, the TEM techniques yield absolutely no information about the longitudinal field components. This research, the first to show correlation between the experimental and theoretical calculations for the complete microstrip mode, verified that the dominant propagating mode in microstrip was indeed a hybrid coupled mode and not a TEM mode.

In the theoretical analysis, the microstrip region was quantized by a system of nodes. The Helmholtz wave equations were written as finite-difference equations at each node, cast into a matrix eigensystem, and solved on a digital computer to yield the propagation characteristics

and the longitudinal field configuration of the microstrip mode. The transverse field configuration was then calculated via Maxwell's equations. This particular method allowed for the determination of both the longitudinal and transverse components of the electric and magnetic fields.

The results of the theoretical portion of this research not only verified that nonnegligible longitudinal electric and magnetic fields exist but also yielded the complete field distribution of the dominant mode in microstrip. These results imply that the matrix eigensystem method is a valid technique for solving the scalar Helmholtz equations for hybrid coupled modes of propagation. In particular, the numerical results predicted that the dominant microstrip mode was shaped like an inverted saddle about the center strip. More important however, the computed results showed that the dominant mode possessed substantial amounts of circular polarization of the RF magnetic field. This type of polarization has been suspected but had not previously been shown to exist. An interesting observation was that the almost circular polarizations appeared in each of two orthogonal planes. This information will be useful in the design of microwave hybrid integrated circuit components, e.g. a resonance isolator.

It was found that, as the frequency was lowered and as the guide wavelength became greater than the substrate thickness, the relative amplitude of the longitudinal fields decreased and the fields began to approach the TEM mode. At low microwave frequencies, the frequency-phase constant curve approached the straight line of the TEM mode.

The propagation characteristics were verified by observing the frequencies for which resonant transmissions occurred through a loosely coupled short circuited section of microstrip. The f-β curves determined from this experimental research compared favorably with the theoretical curves obtained via the numerical analysis technique. In particular, both sets of curves showed that, in the microwave frequency band, microstrip is indeed dispersive and that a nondispersive TEM solution is not exact.

To complement and verify the theoretical field calculations, a technique was devised which allowed for the determination of the magnetic field components from measured amounts of ferromagnetic spin resonance absorption in a small single crystal YIG sphere. The experimentally determined magnetic fields compare very well with the numerically calculated fields in the vicinity of the center strip. Not only do they have the same shape, but their relative amplitudes are similar. This substantiated the theoretical predictions of a well defined longitudinal field. The theoretically predicted regions of circular polarization of the RF magnetic field are also found. The magnetic field has the form of the saddle mode.

A change in the microstrip line's impedance (change in the ratio of center strip width to substrate thickness) does not seem to change the general shape of the mode pattern and the general propagation characteristics.

The chief limitation in the research was the upper limit on the size matrix that the computer was capable of handling. A faster computer

with an increased storage capacity would allow for a much larger matrix eigensystem to be solved. Alternatively, a different technique (one more nearly aligned with the indirect method) might be developed for solving larger eigensystems. In either case, greater accuracy for the given microstrip problem and increased latitude in w/b ratios could be obtained. In addition, complex matrices could then be introduced, thus allowing for lossy dielectric substrates (characterized by a complex permittivity) and unmagnetized ferrimagnetic substrates (characterized by a scalar complex permeability). Problems involving inhomogeneous substrates, e.g. a ferrite loaded substrate, could then be investigated.

An interesting extension to the present work would be an investigation utilizing bounding walls which require the normal derivatives of the longitudinal fields to vanish in addition to requiring the longitudinal fields to vanish at the bounding walls.

Slot line and coplanar waveguide, the other two types of microwave hybrid integrated circuit transmission lines which are presently undergoing evaluation by the microwave industry can be analyzed by the same numerical technique used to determine the microstrip mode. Quantized models for these two lines are shown in Figure 59.

Another interesting problem that could be solved by this numerical approach is the even-mode and odd-mode coupled microstrip lines. The only theoretical investigation for this major coupling problem has been a purely TEM analysis. A more accurate description of the fields is needed for the precise design of microstrip filters which utilize coupled lines.

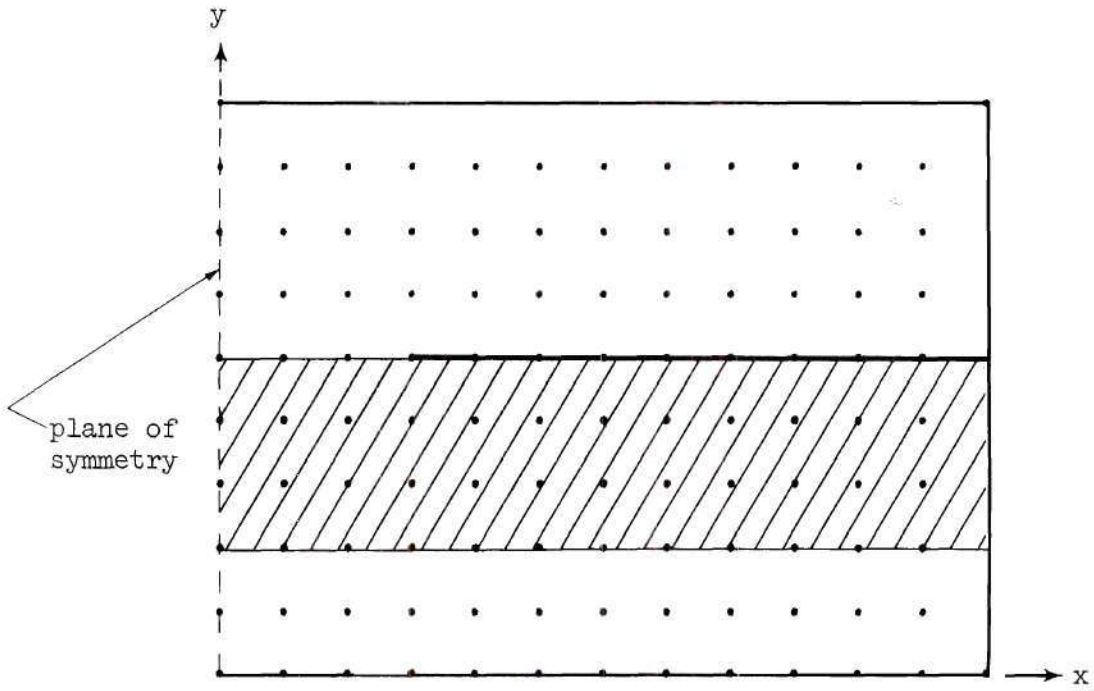

(a) Slot line

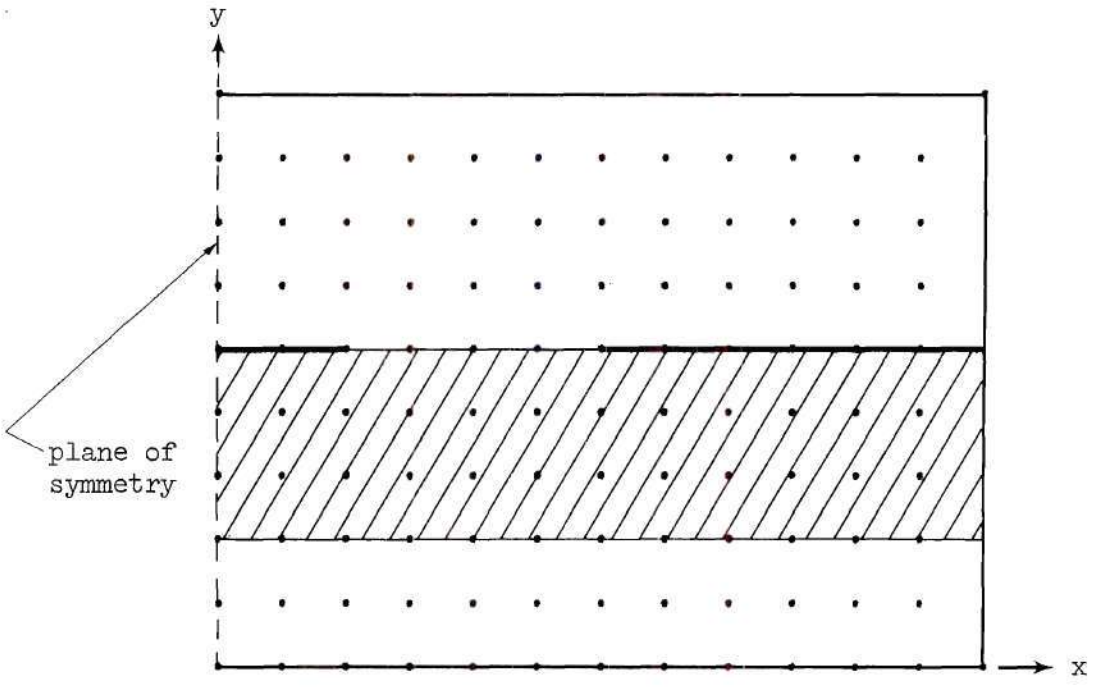

(b) Coplanar waveguide

Figure 59. Models for Slot Line and Coplanar Waveguide

As a result of this research, the propagation characteristics and total field configuration of the microstrip are more clearly understood. In particular, the longitudinal field components have been shown to not only exist and be of substantial amplitude but to be potentially useful. Based on the more accurately determined field configuration, the design of some microstrip components could be improved and their performance optimized. Possibly new components could be developed to perform specific functions.

APPENDICES

APPENDIX A

DERIVATION OF THE AIR-DIELECTRIC INTERFACE EQUATIONS

With reference to Figure 6, at a typical node lying on the air-dielectric interface, the normal component of the magnetic field must be continuous.

$$H_{y_{air}} = H_{y_{dielectric}} \tag{A-1}$$

Equation (7), of Chapter II, gives the general relationship between the normal component of the magnetic field and the longitudinal electric and magnetic field components.

$$H_y = - \frac{1}{k_c^2} \left(j\omega\epsilon \frac{\partial E_z}{\partial x} + j\beta \frac{\partial H_z}{\partial y} \right) \tag{A-2}$$

In the air, k_c^2 and ϵ are replaced by k_a^2 and ϵ_o, respectively. In the dielectric, k_c^2 and ϵ are replaced by k_d^2 and $\kappa\epsilon_o$, respectively. Applying the continuity condition, Equation (A-1) becomes

$$- \frac{j\beta}{k_a^2} \left(\frac{\partial H_z}{\partial y}\right)_A - \frac{j\omega\epsilon_o}{k_a^2} \left(\frac{\partial E_z}{\partial x}\right)_A = - \frac{j\beta}{k_d^2} \left(\frac{\partial H_z}{\partial y}\right)_D - \frac{j\omega\epsilon_o\kappa}{k_d^2} \left(\frac{\partial E_z}{\partial x}\right)_D \tag{A-3}$$

Define the parameter

$$T = \frac{k_a^2}{k_d^2} = \frac{\omega^2\mu_o\epsilon_o - \beta^2}{\omega^2\mu_o\epsilon_o\kappa - \beta^2} \tag{A-4}$$

T is an artificial, nonphysical parameter relating the square of the transverse wave numbers in the air and dielectric. Specifying a value of T is equivalent to specifying the λ_g/λ_o ratio characterizing the solution. Equation (A-3) becomes

$$\beta\left(\frac{\partial H_z}{\partial y}\right)_A + \omega\epsilon_o\left(\frac{\partial E_z}{\partial x}\right)_A = \beta T\left(\frac{\partial H_z}{\partial y}\right)_D + \omega\epsilon_o K T\left(\frac{\partial E_z}{\partial x}\right)_D \qquad \text{(A-5)}$$

after replacing k_a^2/k_d^2 by T and canceling the -j in each term.

The finite-difference equations representing the partial derivative with respect to x is derived in Chapter II and given by Equation (13). An analogous equation can be derived for the y direction. Neglecting the third and fourth order terms, the derivative approximations are given as

$$\left(\frac{\partial H_y}{\partial y}\right)_A = \frac{H_{z_1} h_3}{h_1(h_1+h_3)} - \frac{H_{z_3 A} h_1}{h_3(h_1+h_3)} + \frac{h_1-h_3}{h_1 h_3} H_{z_o} \qquad \text{(A-6)}$$

$$\left(\frac{\partial E_z}{\partial x}\right)_A = \frac{E_{z_4} h_2}{h_4(h_2+h_4)} - \frac{E_{z_2} h_4}{h_2(h_2+h_4)} + \frac{h_4-h_2}{h_2 h_4} E_{z_o}$$

$$\left(\frac{\partial H_z}{\partial y}\right)_D = \frac{H_{z_1 D} h_3}{h_1(h_1+h_3)} - \frac{H_{z_3} h_1}{h_3(h_1+h_3)} + \frac{h_1-h_3}{h_1 h_3} H_{z_o}$$

$$\left(\frac{\partial E_z}{\partial x}\right)_D = \frac{E_{z_4} h_2}{h_4(h_2+h_4)} - \frac{E_{z_2} h_4}{h_2(h_2+h_4)} + \frac{h_4-h_2}{h_2 h_4} E_{z_o}$$

Since these equations apply at nodes which are on the air-dielectric interface, it is necessary to introduce image magnetic fields. $H_{z_{3A}}$ and $H_{z_{1D}}$ are respectively the image fields which would exist if the finite-

difference approximations were applied to a node which was positioned in an all air or all dielectric medium.

Substituting Equations (A-6) into Equation (A-5) yields

$$\beta\left(\frac{H_{z_1} h_3}{h_1(h_1+h_3)} - \frac{H_{z_3 A} h_1}{h_3(h_1+h_3)} + \frac{h_1-h_3}{h_1 h_3} H_{z_o}\right) + \omega\epsilon_o\left(\frac{E_{z_4} h_2}{h_4(h_2+h_4)} - \frac{E_{z_2} h_4}{h_2(h_2+h_4)}\right. \quad \text{(A-7)}$$

$$\left. + \frac{h_4-h_2}{h_2 h_4} E_{z_o}\right) = \beta T\left(\frac{H_{z_1 D} h_3}{h_1(h_1+h_3)} - \frac{H_{z_3} h_1}{h_3(h_1+h_3)} + \frac{h_1-h_3}{h_1 h_3} H_{z_o}\right)$$

$$+ \omega\epsilon_o K T\left(\frac{E_{z_4} h_2}{h_4(h_2+h_4)} - \frac{E_{z_2} h_4}{h_2(h_2+h_4)} + \frac{h_4-h_2}{h_2 h_4} E_{z_o}\right)$$

Since the image fields $H_{z_{3A}}$ and $H_{z_{1D}}$ are the fields that would exist in an all air or all dielectric medium, then $H_{z_{3A}}$ is H_{z_3} in the finite-difference equation for

$$(\nabla_T^2 + k_a^2) H_z = 0 \quad \text{(A-8)}$$

i.e.

$$2\left(\frac{H_{z_1}}{h_1(h_1+h_3)} + \frac{H_{z_3 A}}{h_3(h_1+h_3)} + \frac{H_{z_2}}{h_2(h_2+h_4)} + \frac{H_{z_4}}{h_4(h_2+h_4)}\right. \quad \text{(A-9)}$$

$$\left. - H_{z_o}\left(\frac{1}{h_1 h_3} + \frac{1}{h_2 h_4}\right)\right) = -k_a^2 H_{z_o}$$

And $H_{z_{1D}}$ is H_{z_1} in the finite-difference equation for

$$(\nabla_T^2 + k_d^2) H_z = 0 \quad \text{(A-10)}$$

i.e.

$$2\left(\frac{H_{z_1 D}}{h_1(h_1+h_3)} + \frac{H_{z_3}}{h_3(h_1+h_3)} + \frac{H_{z_2}}{h_2(h_2+h_4)} + \frac{H_{z_4}}{h_4(h_2+h_4)}\right. \tag{A-11}$$

$$\left. - H_{z_o}\left(\frac{1}{h_1 h_3} + \frac{1}{h_2 h_4}\right)\right) = -k_d^2 H_{z_o}$$

Rearranging Equations (A-9) and (A-11) gives the image fields in terms of the field values of the center node's nearest neighbors.

$$-\frac{H_{z_3 A}}{h_3(h_1+h_3)} = \frac{H_{z_1}}{h_1(h_1+h_3)} + \frac{H_{z_2}}{h_2(h_2+h_4)} + \frac{H_{z_4}}{h_4(h_2+h_4)} \tag{A-12}$$

$$- H_{z_o}\left(\frac{1}{h_1 h_3} + \frac{1}{h_2 h_4}\right) + \frac{k_a^2}{2} H_{z_o}$$

$$\frac{H_{z_1 D}}{h_1(h_1+h_3)} = \frac{-H_{z_3}}{h_3(h_1+h_3)} - \frac{H_{z_2}}{h_2(h_2+h_4)} - \frac{H_{z_4}}{h_4(h_2+h_4)}$$

$$+ H_{z_o}\left(\frac{1}{h_1 h_3} + \frac{1}{h_2 h_4}\right) - \frac{k_d^2}{2} H_{z_o}$$

Elimination of the image fields from Equation (A-7) after division by β yields

(A-13)

$$\frac{H_{z_1} h_3}{h_1(h_1+h_3)} + \frac{H_{z_1} h_1}{h_1(h_1+h_3)} + \frac{H_{z_2} h_1}{h_2(h_2+h_4)} + \frac{H_{z_4} h_1}{h_4(h_2+h_4)} - H_{z_o} h_1\left(\frac{1}{h_1 h_3} + \frac{1}{h_2 h_4}\right)$$

$$+ h_1 \frac{k_a^2}{2} H_{z_o} + \frac{h_1 - h_3}{h_1 h_3} H_{z_o} + \frac{\omega \varepsilon_o}{\beta}(1-KT)\left(\frac{E_{z_4} h_2}{h_4(h_2+h_4)} - \frac{E_{z_2} h_4}{h_2(h_2+h_4)}\right.$$

(continued)

$$+ \frac{h_4 - h_2}{h_2 h_4} E_{z_o}\Big) = - \frac{H_{z_3} Th_3}{h_3(h_1+h_3)} - \frac{H_{z_2} Th_3}{h_2(h_2+h_4)} - \frac{H_{z_4} Th_3}{h_4(h_2+h_4)}$$

$$+ H_{z_o} Th_3 \left(\frac{1}{h_1 h_3} + \frac{1}{h_2 h_4}\right) - Th_3 \frac{k_d^2}{2} H_{z_o} - \frac{H_{z_3} Th_1}{h_3(h_1+h_3)} + T \frac{h_1 - h_3}{h_1 h_3} H_{z_o}$$

Rearranging and collecting like terms yields

$$H_{z_1} \left(\frac{2}{h_1(h_1+h_3)}\right) + H_{z_2} \left(\frac{2(h_1+Th_3)}{(h_1+h_3)h_2(h_2+h_4)}\right) + H_{z_3} \left(\frac{2T}{h_3(h_1+h_3)}\right) \qquad \text{(A-14)}$$

$$+ H_{z_4} \left(\frac{2(h_1+Th_3)}{(h_1+h_3)h_4(h_2+h_4)}\right) + H_{z_o} \left(\frac{-2(h_1+Th_3)}{(h_1+h_3)} \left(\frac{1}{h_1 h_3} + \frac{1}{h_2 h_4}\right)\right.$$

$$\left. + 2 \frac{h_1 - h_3}{h_1 h_3 (h_1+h_3)} (1-T)\right) + \frac{2\omega\epsilon_o}{\beta} \frac{(1-KT)}{(h_1+h_3)} \left(\frac{E_{z_4} h_2}{h_4(h_2+h_4)} - \frac{E_{z_2} h_4}{h_2(h_2+h_4)}\right.$$

$$\left. + \frac{h_4 - h_2}{h_2 h_4} E_{z_o}\right) = -k_a^2 H_{z_o}$$

This equation gives the center node magnetic field in terms of the nearest neighbor magnetic fields and nearest neighbor electric fields. In other words, the electric field is coupled to the magnetic field along the air-dielectric interface. Note, however, that in the coupling term, the unknown phase velocity ω/β is present. To circumvent this difficulty, define a normalized electric field

$$\bar{E}_{z_i} = \frac{\chi\omega\epsilon_o}{\beta} E_{z_i} \qquad \text{(A-15)}$$

where the phase velocity is now absorbed and need be determined only after the finite-difference equations have been solved. A scale factor χ is also included in order to aid in the solution of the equations. The final result is

$$H_{z_1}\left(\frac{2}{h_1(h_1+h_3)}\right) + H_{z_2}\left(\frac{2(h_1+Th_3)}{h_2(h_1+h_3)(h_2+h_4)}\right) + H_{z_3}\left(\frac{2T}{h_3(h_1+h_3)}\right) \qquad \text{(A-16)}$$

$$+ H_{z_4}\left(\frac{2(h_1+Th_3)}{h_4(h_1+h_3)(h_2+h_4)}\right) + H_{z_0}\left(\frac{-2(h_1+Th_3)}{(h_1+h_3)}\left(\frac{1}{h_1h_3}+\frac{1}{h_2h_4}\right)\right.$$

$$\left. + 2\,\frac{h_1-h_3}{h_1h_3}\,\frac{(1-T)}{(h_1+h_3)}\right) + 2\,\frac{(1-\chi T)}{(h_1+h_3)}\left(\frac{\bar{E}_{z_4}h_2}{h_4(h_2+h_4)} - \frac{\bar{E}_{z_2}h_4}{h_2(h_2+h_4)}\right.$$

$$\left. + \frac{h_4-h_2}{h_2h_4}\,E_{z_0}\right) = -\,k_a^2\,H_{z_0}$$

Now, an equation relating the center node electric field to the nearest neighbor electric fields and nearest neighbor magnetic fields is needed. In order to derive this equation, use the boundary condition requiring the tangential components of the magnetic field to be continuous across the air-dielectric interface.

$$H_{x_{air}} = H_{x_{dielectric}} \qquad \text{(A-17)}$$

Equation (7), of Chapter II, gives the general equation

$$H_x = -\,\frac{j\beta}{k_c^2}\left(\frac{\partial H_z}{\partial x}\right) + \frac{j\omega\epsilon}{k_c^2}\left(\frac{\partial E_z}{\partial y}\right) \qquad \text{(A-18)}$$

as derived from Maxwell's equations. As in the derivation of Equation (A-3), in the air k_c^2 and ϵ are replaced by k_a^2 and ϵ_o, respectively. In the dielectric k_c^2 and ϵ are replaced by k_d^2 and $\kappa\epsilon_o$, respectively. Substituting into Equation (A-17) and employing Equation (A-4) yields

$$- \beta\left(\frac{\partial H_z}{\partial x}\right)_A + \omega\epsilon_o\left(\frac{\partial E_z}{\partial y}\right)_A = - \beta T\left(\frac{\partial H_z}{\partial x}\right)_D + \omega\epsilon_o\kappa T\left(\frac{\partial E_z}{\partial y}\right)_D \qquad \text{(A-19)}$$

For the derivatives normal to the interface, it is necessary to introduce image electric fields $E_{z_{3A}}$ and $E_{z_{1D}}$. The finite-difference equations representing the partial derivatives are then

$$\left(\frac{\partial H_z}{\partial x}\right)_A = \frac{H_{z_4} h_2}{h_4(h_2+h_4)} - \frac{H_{z_2} h_4}{h_2(h_2+h_4)} + \frac{h_4-h_2}{h_2 h_4} H_{z_o} \qquad \text{(A-20)}$$

$$\left(\frac{\partial E_z}{\partial y}\right)_A = \frac{E_{z_1} h_3}{h_1(h_1+h_3)} - \frac{E_{z_{3A}} h_1}{h_3(h_1+h_3)} + \frac{h_1-h_3}{h_1 h_3} E_{z_o}$$

$$\left(\frac{\partial H_z}{\partial x}\right)_D = \frac{H_{z_4} h_2}{h_4(h_2+h_4)} - \frac{H_{z_2} h_4}{h_2(h_2+h_4)} + \frac{h_4-h_2}{h_2 h_4} H_{z_o}$$

$$\left(\frac{\partial E_z}{\partial y}\right)_D = \frac{E_{z_{1D}} h_3}{h_1(h_1+h_3)} - \frac{E_{z_3} h_1}{h_3(h_1+h_3)} + \frac{h_1-h_3}{h_1 h_3} E_{z_o}$$

Substituting into equation (A-19) yields

$$- \beta\left(\frac{H_{z_4} h_2}{h_4(h_2+h_4)} - \frac{H_{z_2} h_4}{h_2(h_2+h_4)} + \frac{h_4-h_2}{h_2 h_4} H_{z_o}\right) + \omega\epsilon_o\left(\frac{E_{z_1} h_3}{h_1(h_1+h_3)}\right. \qquad \text{(A-21)}$$

$$\left. - \frac{E_{z_{3A}} h_1}{h_3(h_1+h_3)} + \frac{h_1-h_3}{h_1 h_3} E_{z_o}\right) = - \beta T\left(\frac{H_{z_4} h_2}{h_4(h_2+h_4)} - \frac{H_{z_2} h_4}{h_2(h_2+h_4)}\right.$$

(continued)

$$+ \frac{h_4 - h_2}{h_2 h_4} H_{z_o}\Big) + \omega\epsilon_o\kappa T\Big(\frac{E_{z_1 D} h_3}{h_1(h_1+h_3)} - \frac{E_{z_3} h_1}{h_3(h_1+h_3)} + \frac{h_1 - h_3}{h_1 h_3} E_{z_o}\Big)$$

As before, the image electric fields are eliminated by use of the finite-difference equation approximation for the transverse Helmholtz equations

$$(\nabla_T^2 + k_a^2)\, E_z = 0 \qquad \text{(A-22)}$$

$$(\nabla_T^2 + k_d^2)\, E_z = 0$$

Solving the difference equations,

$$2\Big(\frac{E_{z_1}}{h_1(h_1+h_3)} + \frac{E_{z_3 A}}{h_3(h_1+h_3)} + \frac{E_{z_2}}{h_2(h_2+h_4)} + \frac{E_{z_4}}{h_4(h_2+h_4)} \qquad \text{(A-23)}$$

$$- E_{z_o}\Big(\frac{1}{h_1 h_3} + \frac{1}{h_2 h_4}\Big)\Big) = - k_a^2 E_{z_o}$$

$$2\Big(\frac{E_{z_1 D}}{h_1(h_1+h_3)} + \frac{E_{z_3}}{h_3(h_1+h_3)} + \frac{E_{z_2}}{h_2(h_2+h_4)} + \frac{E_{z_4}}{h_4(h_2+h_4)}$$

$$- E_{z_o}\Big(\frac{1}{h_1 h_3} + \frac{1}{h_2 h_4}\Big)\Big) = - k_d^2 E_{z_o}$$

for the image electric fields yields

$$\frac{-E_{z_3 A}}{h_3(h_1+h_3)} = \frac{E_{z_1}}{h_1(h_1+h_3)} + \frac{E_{z_2}}{h_2(h_2+h_4)} + \frac{E_{z_4}}{h_4(h_2+h_4)} \qquad \text{(A-24)}$$

$$- E_{z_o}\Big(\frac{1}{h_1 h_3} + \frac{1}{h_2 h_4}\Big) + \frac{k_a^2}{2} E_{z_o}$$

and

$$\frac{E_{z_1} D}{h_1(h_1+h_3)} = -\frac{E_{z_3}}{h_3(h_1+h_3)} - \frac{E_{z_2}}{h_2(h_2+h_4)} - \frac{E_{z_4}}{h_4(h_2+h_4)}$$

$$+ E_{z_0}\left(\frac{1}{h_1 h_3} + \frac{1}{h_2 h_4}\right) + \frac{k_d^2}{2} E_{z_0}$$

Substituting into the boundary condition equation, Equation (A-19) yields

$$-\left(\frac{H_{z_4} h_2}{h_4(h_2+h_4)} - \frac{H_{z_2} h_4}{h_2(h_2+h_4)} + \frac{h_4-h_2}{h_2 h_4} H_{z_0}\right)(1-T) + \frac{\omega\epsilon_0}{\beta}\left(\frac{E_{z_1} h_3}{h_1(h_1+h_3)}\right. \qquad \text{(A-25)}$$

$$+ \frac{E_{z_1} h_1}{h_1(h_1+h_3)} + \frac{E_{z_2}}{h_2(h_2+h_4)} + \frac{E_{z_4} h_1}{h_4(h_2+h_4)} - E_{z_0} h_1\left(\frac{1}{h_1 h_3} + \frac{1}{h_2 h_4}\right) + \frac{h_1 k_a^2}{2} E_{z_0}$$

$$\left. + \frac{h_1-h_3}{h_1 h_3} E_{z_0}\right) = \frac{\omega\epsilon_0 KT}{\beta}\left(\frac{-E_{z_3} h_3}{h_3(h_1+h_3)} - \frac{E_{z_2} h_3}{h_2(h_2+h_4)} - \frac{E_{z_4} h_3}{h_4(h_2+h_4)}\right.$$

$$\left. + E_{z_0} h_3\left(\frac{1}{h_1 h_3} + \frac{1}{h_2 h_4}\right) - \frac{h_3 k_d^2}{2} E_{z_0} - \frac{E_{z_3} h_1}{h_3(h_1+h_3)} + \frac{h_1-h_3}{h_1 h_3} E_{z_0}\right)$$

Rearranging, collecting like terms, and employing the normalized electric field of Equation (A-15) yields

$$-\left(\frac{H_{z_4} h_2}{h_4(h_2+h_4)} - \frac{H_{z_2} h_4}{h_2(h_2+h_4)} + \frac{h_4-h_2}{h_2 h_4} H_{z_0}\right)\frac{2(1-T)}{h_1+Kh_3} + \bar{E}_{z_1}\left(\frac{2}{h_1(h_1+Kh_3)}\right) \qquad \text{(A-26)}$$

$$+ \bar{E}_{z_2}\left(\frac{2(h_1+KTh_3)}{(h_1+Kh_3)h_2(h_2+h_4)}\right) + \bar{E}_{z_3}\left(\frac{2KT}{h_3(h_1+Kh_3)}\right) + \bar{E}_{z_4}\left(\frac{2(h_1+KTh_3)}{(h_1+Kh_3)h_4(h_2+h_4)}\right)$$

$$- \bar{E}_{z_0}\left(\frac{-2(h_1+KTh_3)}{(h_1+Kh_3)}\left(\frac{1}{h_1 h_3} + \frac{1}{h_2 h_4}\right) + 2\frac{(h_1-h_3)}{h_1 h_3}\frac{(1-KT)}{(h_1+Kh_3)}\right) = -k_a^2 \bar{E}_{z_0}$$

This equation expresses the required coupling between the electric field at the center node and the adjacent field values along the interface.

APPENDIX B

QR TRANSFORM

The QR transform has proved to be a powerful method for calculating the eigenvalues λ of a general matrix A.

$$(A - \lambda I)\ \Phi = 0 \tag{B-1}$$

The method, developed and tested by Francis, works well on real or complex and symmetric or nonsymmetric matrices. It makes use of similarity transformations which tend to be numerically stable. The basis of the transform is to decompose the matrix A into the product of a unitary matrix and an upper triangular matrix R,

$$A^{(k)} = Q^{(k)}R^{(k)} \tag{B-2}$$

where the superscript k implies the k^{th} iteration or application of the decomposition. Calculations in the QR transform are made simpler if the matrix A is initially reduced to upper Hessenberg form by Householder's method. The matrix form is given by Equation (72) in Chapter II. As $k \rightarrow \infty$, the matrix $A^{(k)}$ tends to an upper triangular matrix, the diagonal elements of which are the eigenvalues of A.

Beginning with the Hessenberg matrix, an iteration is performed by premultiplying $A^{(k)}$ by $Q^{(k)*}$ to get

$$Q^{(k)*}A^{(k)} = Q^{(k)*}Q^{(k)}R^{(k)} = R^{(k)} \tag{B-3}$$

The n-1 subdiagonal elements of the matrix $A_{i+1,i}$, i = 1, 2, 3, $\cdots$n-1, are eliminated in turn by a series of elementary unitary matrices.

$$\begin{aligned} Q_1^{(1)*}A^{(1)} &= A_2^{(1)} \\ Q_2^{(1)*}A_2^{(1)} &= A_3^{(1)} \\ &\vdots \\ Q_{n-1}^{(1)*}A_{n-1}^{(1)} &= R^{(1)} \end{aligned} \tag{B-4}$$

or

$$Q^{(1)*}A^{(1)} = Q_1^{(1)*}Q_2^{(1)*}Q_3^{(1)*} \cdots\cdots Q_{n-1}^{(1)*}A^{(1)} = Q^{(1)*}A^{(1)} = R^{(1)} \tag{B-5}$$

Next, the upper triangular matrix $R^{(k)}$ is post multiplied by $Q^{(k)}$ to get $A^{(k+1)}$.

$$\begin{aligned} R^{(1)}Q_1^{(1)} &= R_2^{(1)} \\ R_2^{(1)}Q_2^{(1)} &= R_2^{(1)} \\ &\vdots \\ R_{n-1}^{(1)}Q_{n-1}^{(1)} &= A^{(2)} \end{aligned} \tag{B-6}$$

or

$$R_1^{(1)}\, Q_1^{(1)}Q_2^{(1)}Q_3^{(1)} \cdots\cdots Q_{n-1}^{(1)} = R^{(1)}Q^{(1)} = A^{(2)} \tag{B-7}$$

After one iteration $A^{(2)}$ is derived from $A^{(1)}$. After k iterations, the QR transform can be written as a similarity transform

$$A^{(k+1)} = Q^{(k)*}Q^{(k-1)*} \cdots\cdots Q^{(1)*}A^{(1)}Q^{(1)}Q^{(2)} \cdots\cdots Q^{(k)} \tag{B-8}$$

In many cases, convergence to the eigenvalues is slow. This weakness in the transform is overcome by using a modified form of the algorithm defined by

$$A^{(k)} - k_s^{(k)} I = Q^{(k)} R^{(k)} \tag{B-9}$$

where

$$Q^{(k)*}(A^{(k)} - k_s^{(k)} I) = R^{(k)} \tag{B-10}$$

is formed, and then

$$R^{(k)} Q^{(k)} + k_s^{(k)} I = A^{(k+1)} \tag{B-11}$$

is formed to complete the iteration. If the origin of the eigenvalues is shifted close to λ_n, the eigenvalue of smallest modulus, by the shift $k_s^{(k)}$ before an iteration and shifted back again afterwards, then the subdiagonal elements in the last row will be greatly reduced in that iteration, thus speeding convergence. The value of $k_s^{(k)}$ is determined as follows. Prior to an iteration, say the k^{th}, find the eigenvalues of the last principal 2 x 2 submatrix. If the eigenvalues are real, choose that one that differs least from the last diagonal element $a_{n,n}^{(k)}$ and call it $\lambda^{(k)}$. Initially $\lambda^{(0)}$ is zero. Perform the test

$$\alpha = \left| \frac{\lambda^{(k)} - \lambda^{(k-1)}}{\lambda^{(k)}} \right| \tag{B-12}$$

where $\lambda^{(k-1)}$ was calculated on the $(k-1)^{th}$ iteration. If $\alpha < \frac{1}{2}$, set $k_s^{(k)} = \lambda^{(k)}$, otherwise set $k_s^{(k)} = 0$. If the eigenvalues of the submatrix

are found to be complex, then the matrix will have to take on a complex form if it is real, since shifting by real quantities cannot move the origin of the eigenvalues arbitrarily close to either of the complex conjugate roots.

After each iteration, the subdiagonal elements $a_{n,n-1}$ and $a_{n-1,n-2}$ are tested. If $a_{n,n-1}$ is zero, then $a_{n,n}$ is taken as the eigenvalue and the matrix is deflated by removing the last row and column. If $a_{n-1,n-2}$ is zero, then the last 2 x 2 submatrix is solved to find its two eigenvalues and the matrix is deflated by two rows and two columns.

Another form of the QR transform was developed by Francis in which two iterations are combined into one real operation. If two successive iterations with shifts $k_s^{(k)}$ and $k_s^{(k+1)}$ are performed on a real matrix $A^{(k)}$, the final matrix $A^{(k+2)}$ is real. Since a real nonsymmetric matrix can have complex conjugate eigenvalues, they can be calculated by the double QR transform without having to leave the real field. The transform is defined by

$$A^{(k)} - k_s^{(k)}{}_I = Q^{(k)}R^{(k)} \qquad R^{(k)}Q^{(k)} + k_s^{(k)}{}_I = A^{(k+1)} \tag{B-13}$$

$$A^{(k+1)}k_s^{(k+1)}{}_I = Q^{(k+1)}R^{(k+1)} \qquad R^{(k+1)}Q^{(k+1)} + k_s^{(k+1)}{}_I = A^{(k+2)}$$

or as a similarity transform

$$A^{(k+2)} = Q^{(k+1)*}Q^{(k)*}A^{(k)}Q^{(k)}Q^{(k+1)} \tag{B-14}$$

where

$$(Q^{(k+1)}Q^{(k)})(R^{(k)}R^{(k+1)}) = (A^{(k)} - k_s^{(k)}I)(A^{(k)} - k_s^{(k+1)}) = G \quad \text{(B-15)}$$

The matrices $Q^{(k)}$, $Q^{(k+1)}$, $R^{(k)}$, and $R^{(k+1)}$ can be complex, but

$$W = Q^{(k+1)}Q^{(k)} \quad \text{(B-16)}$$

and

$$D = R^{(k)}R^{(k+1)} \quad \text{(B-17)}$$

will both be real since they correspond to factorization of the real matrix $(A^{(k)} - k_s^{(k)}I)\ (A^{(k)} - k_s^{(k+1)}I)$. The method effectively determines W and $A^{(k+2)}$ from $A^{(k)}$ without computing the possibly complex matrices $Q^{(k)}$, $Q^{(k+1)}$, $R^{(k)}$, and $R^{(k+1)}$. Francis shows that, in order to perform a double iteration, an initial transformation is performed on $A^{(k)}$,

$$P^{(0)}A^{(k)}P^{(0)} \quad \text{(B-18)}$$

changing it to a matrix which is no longer in upper Hessenberg form. Then this matrix is reduced to upper Hessenberg form by Householder's method, and the result is $A^{(k+2)}$.

After a double iteration has been performed, the last subdiagonal elements are tested. Eigenvalues and deflation of the matrix result exactly as in a single QR iteration. The double iteration procedure is continued until the coefficient matrix has been reduced to either a 2 X 2 matrix in which the eigenvalues are calculated directly or a 1 X 1 matrix which is the last eigenvalue.

Proofs and details of the procedures outlined above are contained in Francis's original work.

APPENDIX C

COMPLETE EXPERIMENTAL MEASUREMENTS AND CALCULATIONS

The following three tables contain the location of the measuring YIG sphere probe, the orientation of the DC biasing magnetic field, the measured amounts of the ferromagnetic spin resonance absorption, the measured DC biasing magnetic field in kilogauss, the calculated amount of uniform mode power absorbed by the YIG sphere and the calculated relative RF magnetic field components

Table 16. Measured Uniform and Nonuniform Resonance Absorptions and the Calculated Magnetic Field Components for the .055" Alumina Substrate with w/b = 2

x/W	Orientation of the DC Field	Measured Absorption (dB)	DC Biasing Magnetic Field	Power Absorbed	Relative Magnetic Field
0.010	-y	0.08	3.55	0.017	$h_x = 0.261$
	+y	0.08	3.59	0.017	$h_z = 0.0$
	-x	0.0		0.0	$h_y = 0.0$
	+x	0.0		0.0	
0.200	-y	0.08	3.66	0.017	$h_x = 0.298$
	+y	0.13	3.68	0.028	$h_z = 0.037$
	-x	0.0		0.0	$h_y = 0.0$
	+x	0.0		0.0	
0.254	-y	0.08	3.60	0.017	$h_x = 0.258$
	+y	0.11	3.68	0.024	$h_z = 0.024$
	-x	0.0		0.0	$h_y = 0.0$
	+x	0.0		0.0	
0.309	-y	0.06	3.64	0.013	$h_x = 0.273$
	+y	0.12	3.65	0.026	$h_z = 0.049$
	-x	0.0		0.0	$h_y = 0.0$
	+x	0.0		0.0	

Table 16. (continued)

0.455	-y	0.09	3.57	0.019	h_x = 0.407
	+y	0.24	3.58	0.053	h_z = 0.091
	-x	0.0		0.0	h_y = -0.032
	+x	0.01	3.60	0.001	h_z = 0.032
0.600	-y	0.15	3.58	0.033	h_x = 0.468
	+y	0.38	3.58	0.083	h_z = 0.108
	-x	0.0		0.0	h_y = -0.161
	+x	0.05	3.61		
		0.12	3.64	0.026	h_z = 0.161
0.828	-y	0.01	3.59		
		0.35	3.64	0.076	h_x = 0.800
	+y	0.05	3.59		
		1.40	3.68	0.275	h_z = 0.248
		0.01	3.72		
	-x	0.05	3.61	0.01	h_z = 0.228
		0.01	3.88		
	+x	0.10	3.60		
		0.50	3.61	0.108	h_y = -0.428
		0.02	3.89		
1.020	-y	0.01	3.58		
		0.08	3.59		
		0.06	3.66		
		0.04	3.70	0.019	h_z = 0.532
		0.01	3.84		
	+y	0.05	3.59		
		0.08	3.60		
		0.11	3.69		
		0.11	3.70		
		0.73	3.71	0.155	h_x = 0.256
	-x	0.03	3.57		
		0.11	3.64		
		0.23	3.69		
		0.46	3.69	0.099	h_y = -0.888
		0.02	3.75		
		0.02	3.79		
		0.01	3.81		
	+x	0.015	3.53		
		0.15	3.58		
		0.05	3.63		
		1.15	3.69		
		1.73	3.70	0.328	h_z = 0.258
		0.01	3.71		
		0.03	3.76		
		0.05	3.78		
		0.11	3.90		

Table 16. (continued)

1.180	-y	0.01	3.52		
		0.02	3.59		
		0.59	3.64	0.126	$h_x = -0.129$
		0.02	3.88		
	+y	0.01	3.59		
		0.23	3.63	0.051	$h_z = 0.581$
	-x	0.01	3.61		
		0.90	3.66	0.186	$h_y = -1.224$
		0.015	3.89		
	+x	0.05	3.54		
		4.30	3.65	0.628	$h_z = 0.362$
1.400	-y	1.82	3.69	0.342	$h_x = -0.585$
	+y	0.0		0.0	$h^x = 0.585$
	-x	0.23	3.71	0.050	$h^z = -0.957$
	+x	3.35	3.70	0.538	$h^y_z = 0.509$
1.520	-y	1.05	3.61	0.215	$h_x = -0.464$
	+y	0.0		0.0	$h^x = 0.464$
	-x	0.02	3.66	0.003	$h^z = -0.577$
	+x	1.39	3.65	0.273	$h^y_z = 0.467$
1.745	-y	0.8	3.67	0.168	$h_x = -0.409$
	+y	0.0		0.0	$h^x = 0.409$
	-x	0.01	3.62	0.001	$h^z = -0.444$
	+x	0.81	3.64	0.170	$h^y_z = 0.380$
1.945	-y	0.75	3.64	0.170	$h_x = -0.397$
	+y	0.0		0.0	$h^x = 0.397$
	-x	0.0		0.0	$h^z = -0.349$
	+x	0.57	3.61	0.122	$h^y_z = 0.349$
2.200	-y	0.35	3.65	0.076	$h_x = -0.276$
	+y	0.0		0.0	$h^x = 0.276$
	-x	0.0		0.0	$h^z = -0.302$
	+x	0.42	3.70	0.091	$h^y_z = 0.302$
2.360	-y	0.32	3.63	0.07	$h_x = -0.265$
	+y	0.0		0.0	$h^x = 0.265$
	-x	0.0		0.0	$h^z = -0.247$
	+x	0.28	3.70	0.061	$h^y_z = 0.247$
2.600	-y	0.31	3.61	0.068	$h_x = -0.261$
	+y	0.0		0.0	$h^x = 0.261$
	-x	0.0		0.0	$h^z = -0.180$
	+x	0.15	3.65	0.033	$h^y_z = 0.180$

Table 16. (concluded)

2.730	-y	0.21	3.72	0.045	h_x = -0.212
	+y	0.0		0.0	h_z = 0.212
	-x	0.0		0.0	h_y = -0.141
	+x	0.09	3.65	0.02	h_z = 0.141
2.960	-y	0.13	3.71	0.028	h_x = -0.167
	+y	0.0		0.0	h_z = 0.167
	-x	0.0		0.0	h_y = -0.127
	+x	0.075	3.68	0.016	h_z = 0.127
3.160	-y	0.075	3.60	0.016	h_x = -0.127
	+y	0.0		0.0	h_z = 0.127
	-x	0.0		0.0	h_y = -0.077
	+x	0.03	3.65	0.006	h_z = 0.077
3.550	-y	0.02	3.61	0.003	h_x = -0.055
	+y	0.0		0.0	h_z = 0.055
	-x	0.0		0.0	h_y = -0.032
	+x	0.01	3.69	0.001	h_z = 0.032
3.910	-y	0.01	3.65	0.001	h_x = -0.032
	+y	0.0		0.0	h_z = 0.032
	-x	0.0		0.0	h_y = 0.0
	+x	0.0		0.0	h_z = 0.0

Table 17. Measured Uniform and Nonuniform Resonance Absorptions and the Calculated Magnetic Field Components for the .025" Alumina Substrate with w/b = 2

x/W	Orientation of the DC Field	Measured Absorption (dB)	DC Biasing Magnetic Field	Power Absorbed	Relative Magnetic Field
0.0	-y	2.15	3.75	0.39	h_x = 1.248
		0.10	3.80		
	+y	0.20	3.69		
		2.15	3.75	0.39	h_z = 0.0
		0.02	3.81		
	-x	0.0		0.0	h_y = 0.0
		0.21	3.66		
	+x	0.0		0.0	h_z = 0.0

Table 17. (continued)

0.300	-y	1.40	3.66	0.275	h_x = 1.165
	+y	2.30	3.65	0.41	h_z = 0.116
	-x	0.0		0.0	h_y = -0.21
	+x	0.20	3.68	0.044	h_z = 0.21
		0.06	3.91		
0.86	-y	0.10	3.63		
		0.62	3.72	0.132	h_x = 1.081
	+y	0.19	3.66		
		3.15	3.73	0.515	h_z = 0.355
		0.05	3.84		
	-x	0.01	3.60		
		0.26	3.70		
		0.80	3.71	0.167	h_y = -1.245
		0.10	3.72		
		0.01	3.74		
		0.01	3.79		
		0.07	3.81		
		0.10	3.87		
	+x	0.50	3.69		
		5.20	3.70	0.698	h_z = 0.427
		0.27	3.72		
		0.11	3.81		
		0.09	3.85		
1.220	-y	0.42	3.70	0.092	h_x = 0.913
		0.06	3.75		
		0.02	3.82		
		0.06	3.88		
	+y	0.24	3.62		
		0.01	3.67		
		0.60	3.70		
		2.00	3.71	0.368	h_z = 0.301
	-x	0.15	3.61		
		0.60	3.70		
		2.70	3.75	0.463	h_y = -1.670
		0.04	3.87		
	+x	0.88	3.60		
		0.20	3.65		
		16.80	3.72	0.979	h_z = 0.308
		0.01	3.83		
1.64	-y	3.30	3.75	0.532	h_x = -0.785
	+y	0.02	3.75	0.003	h_z = 0.675
	-x	0.02	3.71		
		1.48	3.78	0.288	h_y = -1.523
	+x	0.13	3.64		
		15.80	3.78	0.974	h_z = 0.449

Table 17. (concluded)

2.040	-y	2.8	3.75	0.475	h_x = -0.721
	+y	0.01	3.77	0.001	h^x = 0.658
	-x	0.48	3.82	0.103	h^z_y = -1.258
	+x	0.05	3.70		
		9.10	3.82	0.877	h_z = 0.616
2.520	-y	3.95	3.79	0.597	h_x = -0.805
	+y	0.01	3.79	0.001	h^x = 0.741
	-x	0.05	3.75	0.01	h^z = -0.830
	+x	3.30	3.76	0.532	h^y_z = 0.630
3.080	-y	2.65	3.80	0.456	h_x = -0.731
	+y	0.02	3.80	0.003	h^x = 0.621
	-x	0.0		0.0	h^z = -0.607
	+x	2.00	3.75	0.368	h^y_z = 0.607
3.600	-y	1.71	3.81	0.325	h_x = -0.625
	+y	0.02	3.81	0.003	h^x = 0.515
	-x	0.0		0.0	h^z = -0.421
	+x	0.85	3.75	0.177	h^y_z = 0.421
4.000	-y	0.97	3.78	0.200	h_x = -0.447
	+y	0.0		0.0	h^x = 0.447
	-x	0.0		0.0	h^z = -0.358
	+x	0.6	3.80	0.128	h^y_z = 0.358
4.400	-y	0.65	3.75	0.138	h_x = -0.372
	+y	0.0		0.0	h^x = 0.372
	-x	0.0		0.0	h^z = -0.255
	+x	0.30	3.79	0.065	h^y_z = 0.255
5.200	-y	0.29	3.74	0.064	h_x = -0.253
	+y	0.0		0.0	h^x = 0.253
	-x	0.0		0.0	h^z = -0.221
	+x	0.22	3.75	0.049	h^y_z = 0.221

Table 18. Measured Uniform and Nonuniform Resonance Absorptions and the Calculated Magnetic Field Components for the .055" D-16 Substrate with w/b = 0.6

x/W	Orientation of the DC Field	Measured Absorption (dB)	DC Biasing Magnetic Field	Power Absorbed	Relative Magnetic Field
0.0	-y	0.72	2.71		
		3.20	2.73	0.521	h_x = 1.434

Table 18. (continued)

		2.80	2.73		
	+y	0.72	2.71		
		3.20	2.73	0.521	h_z = 0.0
		2.20	2.73		
	-x	0.0		0.0	h_y = 0.0
	+x	0.0		0.0	h_z = 0.0
		0.1	2.77		
0.455	-y	0.41	2.74		
		3.50	2.78	0.553	h_x = 1.566
	+y	0.58	2.71		
		4.75	2.75	0.665	h_z = 0.080
		0.10	2.77		
		0.10	2.80		
	-x	0.49	2.71	0.105	h_y = 0.816
		1.40	2.75		
	+x	1.21	2.71	0.242	h_z = 0.068
		0.41	2.72		
1.24	-y	1.31	2.71		
		0.04	2.72		
		0.82	2.81		
		0.87	2.84	0.18	h_z = 0.471
		0.13	2.93		
		0.08	2.99		
	+y	0.92	2.72		
		1.30	2.81		
		7.00	2.84	0.800	h_x = 1.319
		0.01	2.89		
	-x	0.675	2.80		
		0.11	2.80		
		0.60	2.83		
		1.275	2.88		
		3.78	2.88	0.543	h_y = -1.704
		3.40	2.88		
		0.01	2.91		
		0.01	2.95		
		0.01	3.21		
		0.28	3.23		
	+x	0.10	2.70		
		1.63	2.79		
		1.20	2.80		
		0.59	2.85		
		10.35	2.88		
		12.00	2.88	0.937	h_z = 0.232
		0.12	3.10		
		0.36	3.22		

Table 18. (concluded)

2.00	-y	0.02	2.75		
		4.10	2.80	0.611	h_x = -0.575
		0.26	3.00		
	+y	0.01	2.75		
		0.20	2.79	0.043	h_z = 0.989
		0.08	3.00		
	-x	1.81	2.78	0.340	h_y = -1.572
		0.10	3.00		
	+x	0.10	2.63		
		16.70	2.78	0.979	h_z = 0.406
		0.12	2.98		
3.03	-y	5.75	2.86	0.734	h_x = -0.911
		0.13	3.05		
	+y	0.02	3.09	0.003	h_z = 0.801
	-x	0.86	2.80	0.179	h_y = -1.405
		0.025	3.05		
	+x	0.03	2.70		
		14.50	2.80	0.965	h_z = 0.559
		0.08	3.02		
3.730	-y	5.50	2.87	0.718	h_x = -0.848
	+y	0.0		0.0	h_x = 0.848
	-x	0.28	2.80	0.061	h_z = -1.134
	+x	6.7	2.79	0.786	h_z = 0.640
4.330	-y	4.05	2.78	0.606	h_x = -0.838
	+y	0.02	2.80	0.003	h_x = 0.728
	-x	0.12	2.80	0.026	h_z = -0.985
	+x	4.95	2.81	0.680	h_z = 0.663
4.940	-y	2.10	2.79	0.382	h_x = -0.650
	+y	0.01	2.79	0.001	h_x = 0.586
	-x	0.02	2.80	0.003	h_z = -0.726
	+x	2.60	2.80	0.450	h_z = 0.616
5.550	-y	1.80	2.79	0.339	h_x = -0.582
	+y	0.0		0.0	h_x = 0.582
	-x	0.0		0.0	h_z = -0.604
	+x	1.98	2.79	0.365	h_z = 0.604
6.150	-y	2.00	2.83	0.368	h_x = -0.661
	+y	0.02	2.84	0.003	h_x = 0.551
	-x	0.0		0.0	h_z = -0.543
	+x	1.53	2.83	0.295	h_z = 0.543
7.49	-y	0.80	2.80	0.167	h_x = -0.441
	+y	0.01	2.80	0.001	h_x = 0.377
	-x	0.0		0.0	h_z = -0.354
	+x	0.595	2.80	0.125	h_z = 0.354

BIBLIOGRAPHY

1. Summary of Microwave Integrated Circuit Investigations, Sperry Microwave Electronics Division, Clearwater, Florida, November 1968.

2. Kilpatrick, T. H., "Micromin for Microwaves," Microwaves, pp 21-34, October, 1967.

3. Leeds, M. B., "Microwave IC's Come of Age," Electronics, pp 107-112, October 30, 1967.

4. Cohn, S. B., "Slot Line - An Alternate Transmission Medium for Integrated Circuits," 1968 International Microwave Symposium, Detroit, Michigan, May 1968.

5. Robinson, G. H. and Allen, J. L., "Application of Slot Line to Miniature Ferrite Devices," IEEE G-MTT 1969 International Microwave Symposium, Dallas, Texas, May 1969.

6. Wen, C. P., "Coplanar Waveguide, A Surface Strip Transmission Line Suitable for Nonreciprocal Gyromagnetic Device Applications," IEEE G-MTT 1969 International Microwave Symposium, Dallas, Texas, May 1969.

7. Aridti, M., "Experimental Determination of the Properties of Microstrip Components," Electrical Communication, pp 283-293, December 1953.

8. Shafer, C. G., "Dominant Mode of the Microstrip Transmission Line," Technical Report No. 257, Cruft Laboratory, Harvard University, Contract Nonr-1886(26), November 1957.

9. Wu, T. T., "Theory of Microstrip," Journal of Applied Physics, Vol. 28, Number 3, pp 299-302, March 1957.

10. Ramo, Whinnery, and Van Duzer, Fields and Waves in Communication Electronics, Wiley, New York, p. 394, 1965.

11. Assadourian, F. and Rimai, E., "Simplified Theory of Microstrip Transmission Systems," Proceedings of the I.R.E., pp 1651-1657, December, 1952.

12. Wheeler, H. A., "Transmission-Line Properties of Parallel Wide Strips by a Conformal-Mapping Approximation," IEEE Transactions on Microwave Theory and Techniques, pp 280-289, May 1964.

13. Wheeler, H. A., "Transmission-Line Properties of Parallel Strips Separated by a Dielectric Sheet," IEEE Transactions on Microwave Theory and Techniques, pp 172-185, March 1965.

14. Caulton, M., Hughes, J. J., and Sobol, H., "Measurement on the Properties of Microstrip Transmission Lines for Microwave Integrated Circuits," RCA Review, pp 377-391, September 1966.

15. Green, H. E., "The Numerical Solution of Some Important Transmission Line Problems," IEEE Transactions of Microwave Theory and Techniques, Vol. 13, pp 676-692, September 1965.

16. Schneider, M. V., "Computation of Impedance and Attenuation of TEM-lines by Finite Difference Methods," IEEE Transactions on Microwave Theory and Techniques, pp 793-800, November 1965.

17. Steinhelfer, H. E., "An Accurate Calculation of Uniform Microstrip Transmission Lines," IEEE Transactions of Microwave Theory and Techniques, pp 439-444, July 1968.

18. Bryant, T. G. and Weiss, J. A., "Parameters of Microstrip Transmission Lines and of Coupled Pairs of Microstrip Lines," IEEE Transactions on Microwave Theory and Techniques, Vol. 16, December 1968.

19. Johnson, C. C., Field and Wave Electrodynamics, McGraw-Hill, New York, p. 107, 1965.

20. Denlinger, E. J., "A Dynamic TE-TM Mode Solution for Microstrip," IEEE G-MTT 1969 International Microwave Symposium, Dallas, Texas, May 1969.

21. Zysman, G. I. and Varon, D., "Wave Propagation in Microstrip Transmission Lines," IEEE G-MTT 1969 International Microwave Symposium, Dallas, Texas, May 1969.

22. Hornsby, J. S. and Gopinath, A., "Numerical Analysis of a Dielectric-Loaded Waveguide with a Microstrip Line - Finite-Difference Methods," IEEE Transactions on Microwave Theory and Techniques, pp 684-690, September, 1969.

23. Paris, D. T. and Hurd, F. K., Basic Electromagnetic Theory, McGraw-Hill, New York, p. 306, 1969.

24. Collins, J. H. and Daly, P., "Calculations for Guided Electromagnetic Waves Using Finite-difference Methods," Journal Electronics Control, Vol. 14, pp 361-378, 1963.

25. Wilkinson, J. H., The Algebraic Eigenvalue Problem, Clarendon, Oxford, p. 521, 1965.

26. Forsythe, G. E. and Wasow, W. R., Finite-Difference Methods for Partial Differential Equations, Wiley, New York, p. 354, 1960.

27. Fox, L., Numerical Solution of Ordinary and Partial Differential Equations, Pergamon, Oxford, p. 75, 1962.

28. Forsythe, G. E. and Wasow, W. R., op. cit., p. 236.

29. Davies, J. B. and Muilwyk, C. A., "Numerical Solution of Uniform Hollow Waveguides with Boundaries of Arbitrary Shape," Proceedings of the IEE (London), Vol. 113, pp 277-284, 1966.

30. Francis, J. G. F., "The QR Transformation, A Unitary Analogue to the LR Transformation - Part 1 and Part 2," Computer Journal, Vol. 4, pp 265-271 and pp 332-345, October, 1961.

31. Ralston, A. and Wilf, H. S., Mathematical Methods for Digital Computers, Vol. II, Second Edition, Wiley, New York, pp. 116-130, 1967.

32. Walsh, J., Numerical Analysis: An Introduction, Thompson, Washington, p. 42, 1967.

33. Wilkinson, J. H., op. cit., pp 321-325.

34. Sinnott, D. H., Cambrell, G. K., Carson, C. T., and Green, H. E., "The Finite Difference Solution of Microwave Circuit Problems," IEEE Transactions on Microwave Theory and Techniques, Vol. 17, pp 464-478, August, 1969.

35. Green, H. E., op. cit., p. 680.

36. Walsh, J., op. cit., p. 112.

37. Ibid., p. 112.

38. Francis, J. G. F., op. cit., p. 339.

39. Smart, J. S., "The Néel Theory of Ferrimagnetism," American Journal of Physics, pp 356-370, September, 1955.

40. Lax, B. and Button, K. J., Microwave Ferrites and Ferrimagnetics, McGraw-Hill, New York, pp. 125ff, 1962.

41. Wang, S., Solid State Electronics, McGraw-Hill, New York, pp. 593-594, 1966.

42. Lax, B. and Button, K. J., op. cit., pp 180-189.

43. Paris, D. T. and Hurd, F. K., op. cit., pp 312-315.

VITA

Russell Perry Wharton was born on September 11, 1941, in Memphis, Tennessee, the son of William Wheeler and Wilma Elizabeth Wharton. He was married to Carroll Gray Prince of Atlanta, Georgia in June, 1963, and has one daughter.

He attended public schools in Memphis, Tennessee and graduated from Central High School in June, 1959. In June, 1963, he received a B.E.E. degree from the Georgia Institute of Technology.

From July, 1963, to September, 1964, he was employed by the General Dynamics Corporation, Pomona, California as an electronic engineer.

In September, 1964, Mr. Wharton entered the Electrical Engineering graduate school at the Georgia Institute of Technology. He received the M.S.E.E. degree in June, 1966. He taught electromagnetic field theory at the Georgia Institute of Technology from 1964 to 1970. He was a consultant with Sperry Microwave Electronics Company, Clearwater, Florida from 1968 to 1970.

From 1966 to 1968 he held a National Science Foundation Trainee Fellowship.